ABSTRACT

BOONMA, APICHART. Geometric Modeling and Analysis of Microneedle Interaction with Soft Tissue for Biomedical Applications. (Under the direction of Dr. Yuan-Shin Lee and Dr. Roger J. Narayan.)

This paper presents three different analytical modeling and evaluation tools that can be used in the design and assessment of microneedle designs for biomedical applications. Microneedles have become widely known in medical field for years. Microneedles were first introduced to enhance transdermal drug delivery by creating passage ways through the Stratum Corneum. It was believed that the small length of microneedles could prevent them from reaching deeper tissues where nervous systems are located. Therefore, medical practices through microneedles are almost painless. Other benefits of microneedles include reducing patient discomfort and preventing infection. Lately, advantages of microneedles have been extended to other medical applications, for example, blood glucose monitoring, biofluid sampling, and local cells treatment.

Microneedles have been manufactured with different geometries, but not all of them are able to penetrate the skin at reasonable force without breaking. This issue becomes more critical when the length of microneedles increases, especially in biosampling, brain probing and stimulation, and other applications where deep tissue access is required. This research proposed a novel method to analyze the insertion force and to evaluate different microneedle geometries. When a microneedle is inserted into skin, it creates deformation. To analyze the microneedle insertion force, monotonous and heterogeneous tetrahedral models of soft tissue were developed.

Typical microneedle designs must satisfy two requirements; 1) it must not break while inserted into skin, and 2) it should be most effective in performing the designed

function. In transdermal microneedle, the first and second requirement may be represented by buckling and skin permeability. However, the assessments of these aspects are usually conducted separately and result in excessive process, cost, and time. This research proposed a new measurement tool, called Microneedle Performance Index (MPI) that combines the two requirements into a single parameter. MPI can be used to analyze and compare sharpness and stability of different microneedle geometries. The geometry that provides better stability value and MPI can be selected and used for medical applications.

In many applications ranging from transdermal drug delivery to brain probing and stimulation, microneedles are typically required to stay applied on soft tissue for a certain period of time in order to deliver the treatment and minimize damage to surrounding area. Flexible microneedle patches are more likely to remain implanted at a precise location compared to rigid patch. This research proposed an energy based surface fitting technique that can be used to demonstrate the characteristics of flexible microneedle patch when it is being fitted onto a free form surface. By varying the physical properties of the patches via the maximum allowable strain energy, their effects on the microneedle performance can be predicted and analyzed.

In summary, by developing the analytical modeling, surface fitting technique, simulation system and the measurement tool, this research offers some engineering tools that help in the design, analysis, and evaluation of microneedles in attempt to find and choose the best microneedle design. The presented techniques can be used in the design and manufacturing of microneedles for biomedical applications.

Geometric Modeling and Analysis of Microneedle Interaction with Soft Tissue for Biomedical Applications

by
Apichart Boonma

A dissertation submitted to the Graduate Faculty of
North Carolina State University
in partial fulfillment of the
requirements for the Degree of
Doctor of Philosophy

Industrial Engineering

Raleigh, North Carolina

2012

APPROVED BY:

_____	_____
Yuan-Shin Lee Chair of Advisory Committee	Roger J. Narayan Co-Chair of Advisory Committee
_____	_____
Robert E. Young	Ezat T. Sanii

DEDICATION

I dedicate this dissertation work to my grandfather, Boonchan and my parents, Prasit and Thongsri for their encouragement and support. My sister, Nonthanit has taken care of everybody during my study years and is very helpful in many ways. My nieces, Eve and Care have worked hard on their schoolwork and are very special.

I also dedicate this dissertation to my beautiful wife, Sutanya and my lovely daughter, Aya for everything they have done for me during these wonderful years. I would never have made it to this stage without them.

BIOGRAPHY

Apichart Boonma was born in Khon Kaen, Thailand. He is a Ph.D. student in the Edward P. Fitts Department of Industrial and System Engineering at North Carolina State University, U.S.A. He received his B.S. (1999) degree in Industrial Engineering from Khon Kaen University, Thailand and his M.S. (2006) degree in Industrial Engineering from North Carolina State University, U.S.A. His research interests include Reverse Engineering (RE), Computer Aided Design and Manufacturing (CAD/CAM), computational geometry for design and manufacturing, human-haptic interface, regenerative medicine, design and analysis of medical devices, physically-based simulation for medical applications including surgical assistance, surgical planning, and physician training. He received the 2012 CAD Best Paper Award from the International CAD Conference and Exhibition in Canada in July 2012. Upon the completion of his Ph.D. degree, he has accepted a faculty position at the Department of Industrial Engineering at Khon Kaen University, Thailand.

ACKNOWLEDGMENTS

I would like to express my deep appreciation and gratitude to my advisor, Dr. Yuan-Shin Lee, for his support, patience, suggestion, and encouragement during my academic and research work at North Carolina State University. Without his valuable guidance and continuous support, I would never have finished my study. I would like to express my gratitude to Dr. Roger J. Narayan for his support, suggestion, and providing access to his lab equipment. I would like to thank Dr. Ezat T. Sanii and Dr. Robert E. Young for their support and serving in my Ph.D. committee. I would also like to thank Dr. Steven D. Jackson for his serving as my graduate representative.

I sincerely thank my research group members: Dr. Yongfu Ren, Dr. Weihang Zhu, Dr. Susana Lai-Yuen, Abhinand Pamali, Ron Aman, Dr. Deyao Ren, Dr. Yingjie Li, Plamen Velinski, Dr. Eui Seok Kim, Dr. Manida Swangnetr, Dr. Plawut Wongwiwat, Xiaofeng Qin, Wenqi Ma, Hantang Qin, and Cai Yi for their discussions, suggestions, friendship, and inspiration. I would also like to thank the visiting professor to our research group, Dr. Jongyun Jung, Dr. Hayong Shin, Dr. Sungin Bae, Dr. Chunquan Li, and Dr. Jialiang Zhang for their valuable suggestions and discussions. In addition, I would like to thank Ryan Boehm for his suggestions and support in training and setting up lab equipment.

Finally, I could not thank enough to my granddad who passed away before my graduation for his continuous encouragement and inspiration. I would like to express my deep gratitude to my dear mom, dad, my lovely wife and daughter for their unconditional love, support, and always being there for me throughout both happy and difficult times.

TABLE OF CONTENTS

LIST OF TABLES

LIST OF FIGURES

CHAPTER 1

INTRODUCTION

1.1. Motivation

Since it was first invented in 1853, the hypodermic Needle has been one of the most widely used medical devices, with an estimated 16 billion injections administered worldwide [Gill 2007]. Typical hypodermic needle is used with a syringe to either deliver drugs to or extract bio-fluid from the body. At present, needles are not only utilized in such tasks, they are also being applied in other applications including biopsies (removing part of tissue for study), brachytherapy (placing source of radiation into the body), regional anesthesia (cause local insensitive), minimum invasive surgery, neurosurgery, and etc. [Abolhassani 2007]. Moreover, needles can be used as a catheter (draining fluid out of body cavity) and ablation probe (removal of harmful substance from the body).

Despite the fact that utilizing needles in such areas are quite common and widely accepted, it is severely limited by numerous side effects e.g. hemorrhage, infection, or toxic dose level due to concentrated dose in the initial state of drug release. It was reported that unsafe injection may infect more than 80,000 people a year with HIV, and more than 10 million with hepatitis viruses. Collectively, these infections may cause over 1.3 million premature deaths a year in subsequent birth cohorts. Such infections may also cost the world more than US$ 535 million annually in direct medical expenditures [Miller 1999]. Furthermore, traditional needles may also cause pain and patience discomfort that could persuade patients reluctant to receive the essential treatments, especially for those who

suffers from needle-phobia. Hence, there is a need for a device that is able to overcome those obstacles while offers similar or better diagnostic and medication approaches.

Microneedles were first introduced as a good prospect to enhance transdermal drug delivery due to their capability of improving drug permeability through the skin and control release of drugs. Their miniscule dimension creates small local stresses, decreases the risk of tissue deformation, infection, and patient discomfort. Microneedles also reduce amount of time for the tissues and patient to recover. Since they only penetrate through the Stratum Corneum where no nerve networks are located, they can be applied to human skin painlessly [Mikszta 2002, Smart 2000]. The history of traditional transdermal drug delivery systems was described in detail in the work of [Prausnitz 2008]. The advantages of microneedles over conventional needles were rapidly realized and the microneedles have been proposed for other applications such as blood glucose monitoring, biosampling, and local cells treatment.

Although it has been reported that microneedles are sufficiently strong for transdermal drug delivery, further studies such as analytical modeling, mechanics and clinical trials are still required to guarantee that the device is safe and effective. These works must be conducted before the device can be used by the general public, or extended to other applications (e.g. biosampling, local cancer treatment, brain probing and stimulation, and etc) where they are operated at a level much deeper beneath the skin [Davis 2004]. For those applications, microneedles must be long enough to reach the target depth. Since typical microneedles lose strength tremendously when the length increases, it is extremely important to improve their robustness by any possible means through various analytical techniques and experiments. Preceding studies showed different strategies to strengthen or improve the

performance of microneedles. For example, high strength materials such as silicon, titanium and metal have been investigated as raw materials for microneedles [Teo 2006]. Different geometries such as cylinder, cone, and rectangular shape were analyzed by theoretical methods and finite element analysis [Aggarwal 2004]. Supporting device such as guiding mechanism was proposed in order to prevent buckling when microneedles are inserted into skin [Khumpuang 2003]. Piercing performance of the device can be also improved by increasing the speed of insertion [Verbaan 2008]. These topics have been studied intensively in the past and have continued up until now.

Among all the techniques, enhancing strength through geometric design is perhaps the most inexpensive and could be very effective approach. The significance of geometry was observed from a nature-made microneedle the mosquito's proboscis. It was believed that the jagged shape of the proboscis facilitates inserting into soft tissue by generating stress concentration near the tip [Aoyagi 2008]. Also, as microneedles are usually formed in an array-liked format (e.g. multiple needles on a substrate), performance analysis of the device should be performed by considering both microneedle geometry and the way it is structured on a substrate. To the best of our knowledge, such extensive geometric-analysis tool that takes micro-scale relationship between tissue and rigid body (i.e. microneedles) into account has not been developed. Modeling the soft-rigid relationship would be greatly beneficial to extend our understandings in the area of soft tissue modeling and mechanics of microneedles in micro-scale. Finally, the knowledge that we have gained could be used in developing an efficient technique to derive the best possible microneedle design that proper fits the requirement of each targeted applications.

1.2. Research objective

In this dissertation, our objective is to investigate and develop computational and modeling techniques that can be used to effectively represent, demonstrate, and predict the interaction between microneedles and soft tissue. The approaches are then used in design and analysis of different microneedle geometries and array parameters. Several fundamental knowledge, theories, and computation techniques such as 3D object reconstruction, physical based object representation, fracture mechanics, insertion mechanics, finite element method, distributed load, 3D surface fitting, and geodesic distance are applied and utilized in order to developing the new methodologies. The following topics are addressed in our study.

1. Modeling of microneedles and micro-scale soft tissue. A volumetric model is proposed to generate a heterogeneous soft tissue and a monotonous microneedle. The models were represented by a collection of four-node tetrahedrons. The parameters that reflect tissue stiffness such as Young's modulus and Poisson ratio are assigned explicitly to each element and can be used to characterize different material properties of tissues.
2. Simulation of soft tissue deformation and modeling of interaction between soft tissue and microneedle. A continuum mechanics based methodology such as Finite Element (FE) modeling is utilized to simulate soft tissue deformation during the process of microneedle insertion. External force applied at the contact site is computed using Hooke's law. Reactive force on the microneedle is characterized by the fracture mechanics.

3. Reactive force analysis of microneedle piercing into soft tissue. Cutting algorithm and tissue relaxation technique are proposed to generate realistic puncture of microneedle into soft tissue. Fracture mechanics is implemented to predict reactive force return to microneedle.
4. Validation of the developed technique using a test station where the applied force generated from microneedle penetration into the tissue sample can be measured.
5. Analysis and evaluation of microneedle designs using a developed measurement tool called Microneedle Performance Index based on microneedle geometry, structural analysis, and skin permeability.
6. Modeling and analytical analysis of flexible microneedle patch based on 3D surface fitting, geodesic distance, and insertion mechanics.

1.3. Organization of the dissertation

The remainder of this dissertation is structured as follows:

Chapter 2 briefly reviews previous researches in the related fields, including introduction of microneedle and its applications, human skin anatomy, mechanics of microneedle, finite element technique, failure modes in microneedle, and skin permeability.

Chapter 3 introduces the monotonous microneedle and heterogeneous soft tissue modeling using four-node tetrahedrons and nonlinear finite element method. The techniques are used in representing and demonstration of the interaction between soft tissue and rigid body in micro-scale. This chapter also presents a two stage insertion force modeling technique. The method divides microneedle insertion process into pre-puncture and post-

puncture stages, and employs the concept of finite element analysis, fracture mechanics and distributed load to predict the insertion force and evaluate different microneedle designs based on the geometric design parameters.

Chapter 4 presents a new numerical approach that can be used in analysis and evaluation of different microneedle designs for biomedical applications. The developed method combines the two design requirements including structural stability and skin permeability into a single parameter called Microneedle Performance Index. MPI evaluates microneedle designs based on 3D geometry, predicted insertion depth, and buckling force, and quantify the resulting skin permeability associated with the designs.

Chapter 5 proposes a modeling technique and 3D surface fitting for flexible microneedle patch. The developed method fits a set of mass nodes representing a flexible microneedle patch onto a free form surface based on the geodesic distance and energy minimization. Analysis and evaluation of the fitted patch is provided through the Microneedle Performance Index.

Chapter 6 presents illustrative examples and results of the proposed modeling and computation techniques. In depth discussions are also provided.

Chapter 7 presents the conclusions and future research works that would broaden the understandings and knowledge in the area of microneedle technology.

CHAPTER 2

LITERATURE REVIEW

In this chapter, we review the previous researches that are related to microneedle technologies, skin anatomy, soft tissue modeling, piercing mechanics, finite element method, skin permeability, and 3D surface fitting techniques. Some of these topics may be further investigated and presented in the following chapters. The recent researches on microneedles and their applications will be discussed first. We then present the previous studies related to the research and development of microneedle and soft tissue interaction model. Lastly, we end this chapter with the review of design optimization and the future trends of the device.

2.1 Introduction

A microneedle is, just as the name describes, basically a needle fabricated in “micro” scale (about a million times smaller than conventional or “meso” scale). Typical dimensions of microneedles are approximately 300 – 1500 microns long and 100 – 300 microns wide [Teo 2006]. Thanks to their small size, microneedles can be inserted into human skin with less chance of hitting a nerve or pain receptor. Thus, least-pain or painless injection can be achieved. Previous studies confirmed that microneedles were applied to human painlessly [Mikszta 2002, Smart 2000] and that penetration up to 1.5 mm could still be painless [Khumpuang 2007]. This benefit demonstrates significant improvement not only in patient compliance to the drug delivery via needling, but it also shows great potential especially in minimal invasive medical treatment, biosampling, local drug delivery, controlled-release,

vaccination, soft tissue reconstruction, brain probing and stimulation, and etc. In each of these applications, microneedles may not only deliver drugs, but they may also be used in different functions such as destroying unwanted skin patch, or transferring signal to stimulate some soft tissues. The followings are some of the medical areas that microneedles may be applied.

2.2 Applications of microneedles

Potential applications of microneedles span from the medical data collection for diagnosis such as biosampling and brain probing, to various types of drug delivery including transdermal drug delivery, local cell treatment, controlled release administration, or even the repair and improvement of the skin such as in collagen induction for cosmetic purpose. Brief introduction to these microneedle applications are provided in this section.

2.2.1 Transdermal drug delivery

Transdermal drug delivery has been known for a while as a treatment procedure where a drug is applied directly on the skin surface. The drug then permeates through several layers of the skin and gets absorbed and circulated throughout the body. Drugs that are usually used in this type of administration are typically in a form of gel, ointment, or dermal patch where drugs and adhesive substances are applied on one side of the device. Although transdermal drug delivery is widely accepted and used all over the world, it does have some limitations. First, despite a reasonable amount of drug is applied on the skin, only a small amount will be successfully absorbed by the body. This is due to the physical structure and

mechanical property of our skin. Skin is a great barrier that is able to prevent the internal organs from almost all kind of chemicals and substances (including drugs) from the outside. Another reason is that the applied drugs usually degrade or become less effective by the time they successfully permeate through the skin.

Another limitation of traditional transdermal drug delivery is that only drugs that retain small molecular size are suitable for this type of medications. Again this is due to the strong structure of the skin that does not allow any large molecule to pass through. However, these limitations can be now overcome by the use of microneedle. Since microneedles physically penetrate through the skin, they create holes where large molecular compounds can gain access to the inside of the body. This opens a new opportunity for many drugs that have never been managed by transdermal drug delivery before. Moreover, drugs can be easily directed to target sites beneath the skin with minimum loss or degradation. Microneedle also offers a capability of controlled release of small amount of drug over a long period of time and thus maintains the drugs and blood concentration within safe dosage. This advantage can never be accomplished by the use of traditional hypodermic needles.

2.2.2 Vaccination

Vaccination is the process of delivering an antigenic material into the body in order to create immunity to a disease. Sometimes a combination of antigenic materials (“one shot does it all”) is preferable to a single material such as in a case where cost and time are limited. Many countries require all of their people to receive vaccination especially babies

and kids. Routine immunization programs account for approximately 750 million injections per year [Miller 1999].

Vaccines can be delivered via various modes including oral, injection, intramuscular, intradermal, transdermal, and intranasal. Oral drug delivery usually requires the patient to follow instructions of how and when to take the pills in order for the drug to be most effective. Vaccines transported this way may lose parts of the dosage due to the digestion system. Vaccine administered by transdermal method usually loses its effectiveness due to degradation and missing dosage. Intranasal drug delivery is limited to only a number of drugs that can be transformed into aerosol drug compounds. Other disadvantages of this type of drug delivery are the limited maximum dose per spray and rapid clearance from the nasal cavity.

Among those administrations, vaccination by injection seems to be the only one that guarantees the delivery of complete dosage. It does, however, have a major drawback due to uneasiness feeling of pains, needle-phobia, infection, allergy, and other side effects. This reluctant feeling and hesitation could add up and eventually draw the patients to avoid taking vaccination. Since microneedle can deliver several vaccines at the same time while maintaining the controlled release administration and painless injection with minimum risk of infection, it is a promising device for delivering different types of vaccines.

2.2.3 Biosampling

Biosampling is a process where a biomaterial such as body's fluid, blood plasma, or even soft tissue is extracted from the body. The sample is then used in diagnosis for a sign of

illness to determine health conditions of the person. Some good examples of biosampling include blood test to determine blood group or a certain decease (e.g. AIDS, Leukemia, etc.) blood glucose monitoring, biopsy for tissue and cell diagnostics (to search for tumor and cancer cell), and many others.

Among all biosampling applications, blood glucose monitoring and insulin delivery appears to catch a lot of focus lately. Both medical procedures are required in diabetes treatments. It is reported that there were at least 171 million people worldwide found suffering from diabetes in 2000. This number was anticipated to increase to almost a double in 2030 [Wild 2004]. In 2005, in the United States alone, approximately 20.8 million people were found having diabetes. About 6.2 million people were undiagnosed and 41 million would be in the stage of pre-diabetic [ADA 2005]. Patients who suffer from diabetes usually need to monitor blood glucose level about 3 - 4 times a day. Microneedles could be used to sample blood glucose level and release insulin whenever it is required with minimum pain and infections.

The use of needle in biopsies began in the past few decades. Biopsy is a diagnosis operation where a sampling of fluid, cells or tissues is removed from the body for examination. Examples of biopsied sites are such as bone marrow, heart, lung, liver, prostate, nervous system, and etc. The procedure can be performed using various cutting tools e.g. knives and needles. The introduction of needle biopsy offers numerous advantages. The rate of post biopsy infection and hemorrhage with urinary clot retention declined to 0.81% and less than 1% respectively [Bostwick 1997]. Needle biopsy is also less likely to cause cancer tracking, seeding, and implantation through the capsule

A common issue in biosampling is the fact that the biomaterials to be tested must be withdrawn from the body. Pain, infections, and patient discomfort are probably the major problems that may cause hesitation or refusal to take the test. Since microneedles can overcome these problems, they may become a potential solution in biosampling application.

2.2.4 Cancer treatment

Chemotherapy is the most common cancer treatment where chemical agents are used to kill cancer cells. The killing compounds work by damaging and prohibiting the cancer cell from reproducing itself. Chemotherapy is considered as a combined modality procedure where several drugs are used simultaneously. Despite the ability to suppress and eliminate cancer cells, chemotherapy is just like a double-edged sword. Since most of the chemical agents are injected intravenously, they are delivered through blood stream and transported to every part of the body. This allows the agents to spread and destroy normal and healthy cells as well.

Moreover, chemotherapy does have several side effects, such as pain, vomiting, diarrhea, hair loss, memory loss, weight loss, hemorrhage, cardio-toxicity, hepato-toxicity, nephro-toxicity, and etc. Therefore, prior to the execution of the procedure, precise control and planning on the dosage must be determined. Microneedles could be one of potential candidates to improve chemotherapy through their capability to deliver chemical agents to the local target areas. This minimizes the amount of healthy cells to be destroyed by the agents. Besides, microneedles leave only tiny wounds that are easily recovered. Controlled

release of drugs, provided by microneedles, are also important for long term and consistent chemotherapy.

2.2.5 Soft tissue reconstruction

In aesthetic treatment, microneedling or microneedle therapy is the process where microneedles are used in facial and body cosmetic enhancement. Microneedles can be used to manipulate skin color, cure or create different pattern on the skin [Yuzhakov 2003]. Also, it can be used to create openings in the skin such that nutrients or beneficial substances are absorbed more effectively.

Aesthetic treatments may be classified into two categories; 1) skin repair, and 2) skin coloring. Skin repair includes both returning the skin to its previous condition and enhancing the skin. Treatments that fall within this category are damaged skin treatment (e.g. burnt skin), scar treatment, botox injection, wrinkle reduction, and tattoo removal [Rapaport 2011]. Taking scars as an example, they are traditionally cured by laser or needles. The basic concept is to break the scar tissues apart such that the reproductive collagens are able to grow into the space and eventually lift the depressive skin. Potential use of microneedle in scar treatment was realized recently. Use of microneedle array in shallow acne scar treatment was reported in asia [Kim 2009, Thiboutot 2009].

Skin coloring includes implanting cosmetic compound, coloring substance, erasing previous coloring, and smoothing skin color [Yuzhakov 2003]. Cosmetic implant is a process where cosmetic compounds are delivered to the target site. Typically the mixture may last from 3 – 6 months depending upon the depth of insertion and molecular size of the mixture.

With the use of microneedle, artificial color (e.g. lib-stick) may be injected to the depth of epidermis where it will remain for a certain amount of time (typically last around 1 – 3 months) before the color begins to fade away. High resolution coloring or pattern is also achievable with microneedles.

2.2.6 Brain probing and stimulation

Microprobes or electrodes have been used in diagnosing and treatment of certain diseases like Parkinson's. They can be used in activating paralyzed limbs or controlling other devices such as prostheses, robots, and etc. These applications involve neural signal recording, neuronal tissue study, and neuronal function restoration [Motta 2005]. In such tasks, microprobes are inserted into the brain while maintaining minimum damage to the surrounding cells. Once they arrive at the predetermined depth, the electrodes can measure the patterned neural signal emanated from neurons and send it to a computer for recording or processing. The devices can also work in the opposite way. That is, they can release electrical signal to re-energize a part of the brain that has been damaged or transmit the signal directly to the functional motor parts in the body (e.g. muscles) – while bypassing the obstruction part (e.g. damaged spinal cord).

In general, brain probing applications are composed of cortical and deep brain probing. In cortical probing, the length of cortical electrodes needs to be about 1 – 1.2 mm while in the deep brain probing the parameter must be at least 10 mm (10 times longer) to reach subthalamic nucleus (in rats) [Motta 2005]. The width of the arrays is usually ranging between 1.5 – 4.2 mm [Rousche 1998, Maynard 1997]. Moreover, as the microprobes need

to be inserted into the brain, the proper insertion depth of these microprobes was approximately 1 mm.

Microneedle patch may be applicable in the area of brain stimulation as it can be used similar to electrodes. Its major advantage over traditional electrodes is that they can record neural signal at several sites simultaneously. Early studies used single electrode to record the neural signal and study the function and organization of the cortex. However, single electrode tends to obtain information only from the location it is inserted into. To collect larger amount of data, simultaneous monitoring of multiple neuron groups is required. This can be achieved with multiple electrodes.

We have described some potential applications of microneedles. For a microneedle to be applied in such areas, the major obstacle may be how to make successful puncture into skin and arrive at the working depth. As human skin demonstrates very complicated characteristics, it is important to learn and understand its structure and physical properties. A review of skin anatomy will be provided here to help the readers to have a basic knowledge on the structure and organization of the human skin.

2.3 Anatomy of human skin

In mesoscale, human skin can be viewed with bare eyes as a collection of features such as hairs, wrinkles, and pores. In micro scale, however, it is barely visible by naked eyes and usually must be observed by a fine optical instrument. The skin composes of several layers. It can be categorized into two major components including Epidermis and Dermis.

Figure 2.1 shows the anatomy of human skin including tissue layers and other components e.g. blood vessels, hairs, and etc.

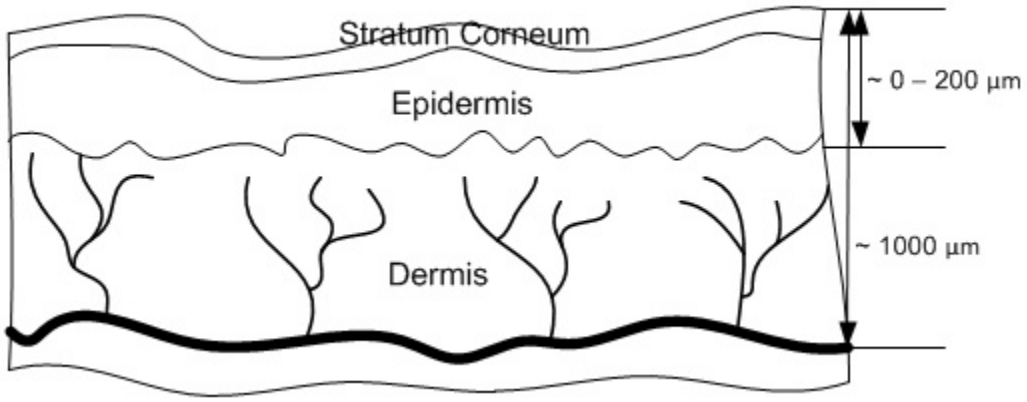

Figure 2.1. Anatomy of human skin.

Epidermis is approximately 75 – 150 µm thick [Odland 1991], containing no blood vessels and fed through diffusion from blood capillaries in Hypodermis region. Epidermis consists of Merkel cells, Keratinocytes, Melanocytes, and Langerhan cells. Through mitosis, these cells continuously generate themselves outward. Cells gradually change its properties and shape while they are moving up (toward outermost skin layer), and finally die when they are too far from nourishing sources (blood capillaries). This process is called keratinization. Epidermis can be divided into four to five layers including Stratum Corneum, Stratum Lucidum, Stratum Granulosum, Stratum Spinosum, and Stratum Germinativum (or Stratum Basale).

Among all Epidermis layers, the outermost skin layer is called Stratum Corneum. It composed of dead cells that move upward from Stratum Granulosum (a layer in Epidermis

region the lies deeper beneath Stratum Corneum). Stratum Corneum is approximately 10 – 40 μm thick, enriched with keratin, and acts as a barrier to all kind of chemicals and other substances from outside the body.

Dermis is approximately 1 – 2 mm thick, located between epidermis and hypodermis. It is connected tightly to epidermis by epidermal-dermal junction. Dermis contains blood vessels, lymphatic vessels, sweat glands, hair follicles, sebaceous (oil) glands, Spocrine glands, mechanoreceptors or nerve endings that provide sense of touch and heat. Blood vessels in dermis layer feed oxygen and nutrients to cells in both dermis and epidermis region.

Based on the human skin structure, the reason that microneedle insertion can be painless may be realized. Since microneedles are rather short (e.g. transdermal microneedles are typically shorter than 500 μm), they will never reach the pain receptors which are located near the bottom of Dermis layer. Even if they do, the size of microneedles may not be large enough to trigger the pain receptor. The sensation of pain is therefore related to the size of microneedles. Several studies have been researched on different geometries and dimensions, aiming to find the most suitable design for microneedles. The followings are some reviews of those studies.

2.4 Overview of microneedles

2.4.1 Types of microneedles

Base on their appearances, microneedles can be classified into two major categories including in-plane and out-of-plane microneedles. In-plane microneedles usually have only

one row of microneedles and are more suitable to small skin area [Stoeber 2005]. Out of plane microneedles typically consist of several needles. Their appearances look similar to a combination of several in-plane microneedles that create a 2D area full of needles. Out-of-plane microneedles are more suitable for larger skin area than in-plane microneedles.

However, If microneedles are to be classified by delivery methods, they could be divided into three categories including solid, hollow, and dissolvable microneedles. Solid microneedles do not have a channel inside their bodies. Drugs are typically coated on the external surface and will diffuse into soft tissues after puncture. Hollow microneedles are basically small scale of regular microneedles. They have small a channel (or more) in the body. The channel acts as a pathway for drugs to pass through. Lastly, dissolvable microneedles are made from drugs directly. That is, drugs are formed into solid matter and in the shape of microneedle. They will gradually dissolve and diffuse into human body shortly after puncture.

2.4.2 Fabrication materials of microneedles

Microneedles can be made out of various materials such as silicon [Wilke 2007], metals [Kim 2007], titanium [Parker 2007], and polymers [Park 2007]. Silicon microneedles are typically made by deep reactive ion etching method. The fabrication process starts by creating a mask on a silicon wafer and patterning it into the shape of microneedles using photolithography. The wafer is then etched by plasma. This process is capable of producing high aspect ratio microneedles.

Polymers are preferable compared to other materials due to their inexpensive production cost and biocompatibility. Some examples of polymers are Polylactic Acid (PLA), Polyglycolic Acid (PGA), and their co-polymers (Polylactide Co-Glycolide Acid: PLGA). Despite their safety use as medical tools, cost effective, and biocompatibility, some polymers might not be suitable to be used as raw material for microneedles due to low physical properties (e.g. PLGA). However, a recent research reported new type of polymers, namely eShell 200 [Gittard 2009]. The polymer is very strong as its Young's modulus is about 2400 GPa.

Metals are one of materials that we can use to produce microneedles. They are selected because of the advantages of mechanical strength, easy to fabrication, rather inexpensive, and safe records as they have been used in several medical application. Although aforementioned materials show promising results in microneedle fabrication, none of them are perfect. For example, silicon could fracture easily and its biocompatibility has never been verified by clinical practices. Polymers are biocompatible and safer but they are rather weak compared to other materials. Some metals have been reported toxic and although some of them have never shown a record of being harmful to the body, it is still at risk using it before conducting a thorough clinical test. A good review on different types of microneedles can be found in [Teo 2006].

2.4.3 Microneedle geometry

Microneedles can be fabricated into various shapes and dimensions. There have been several tip geometries reported. The body or shaft of microneedles, however, is formed into

simple shapes e.g. cone, cylinder, bevel or pyramid. Other geometries such as extremely-sharp and side-open microneedles, were designed to reduce insertion force and improve permeability of drugs into the body.

2.4.4 Microneedle fabrication techniques

There are a number of micro-fabrication methods that are capable of producing microneedles. Park et al used SU-8 epoxy photoresist or polyurethane master structures to create a pattern of microneedles [Park 2005]. Then, the mask was formed by a metal layer and the sample was etched by deep reactive ion etching method. The final product was used to create a mold for polymeric microneedles. Advantages of micromolding are low cost, durability and transparency. Also, the SU-8 photoresist has unique properties such as low optical absorption in UV range, good adhesive properties and inexpensiveness.

Micromachining can be used to produce microneedles as well. Laser micromachining uses material ablation to create 3D features in a single step. The concept was applied from semiconductor industry in 1980s and has been continually improved since then. Other methods capable of producing microneedles are wet and dry etchings. Wet and dry etchings are important process in producing microneedles since they can be used to sharpen the tip of microneedles. The bad news, though, is that they are neither low cost nor suitable for mass production. It only allows the use of wet and dry etching for small lot production.

Since microneedles can be made out of various materials and into different geometries and dimensions, how do we know whether they will be able to make successful

puncture into skin without damage? The answer to this question may be answered by the knowledge of solid mechanics and structural failures.

2.5 Failure modes in microneedles

When a microneedle is trusted against an object (e.g. soft tissue), it behaves like a beam or column under external forces. Therefore, behavior of beam and column could be used as a model for microneedle study. Naturally, a slender part as microneedle buckles when it is loaded with small loads in axial direction. Such condition usually causes buckling failure in the structure and the importance of this phenomenon was reported [Aggarwal 2004].

Basic analysis of beam and column was presented and applied in microneedle analysis in previous studies [Timoshenko 1961, Zahn 1995, Aggarwal 2004]. Assuming that a microneedle is uniform throughout the whole body and there is no lateral load acting upon the microneedle, when the microneedle is being inserted, behaviors of microneedle can be explained by the case of an ideal beam under axial load. If the effects of shearing deformation and shortening of the beam axis are neglected, by summing all forces as shown in Figure 2.2, we obtain:

$$-V + qdx + (V + dV) = 0 \tag{2.1}$$

Rearrange Equation (2.1) and therefore:

$$q = -\frac{dV}{dx} \tag{2.2}$$

Taking moment around point *n*, Equation (2.2) can then be written as:

$$M + qdx\frac{dx}{2} + (V + dV)dx - (M + dM) + P\frac{dy}{dx}dx = 0 \tag{2.3}$$

Thus:

$$M + \frac{q}{2}(dx)^2 + (V + dV)dx - M - dM + Pdy = 0 \tag{2.4}$$

Assuming that the angle between horizontal line and axis of the beam is small, the second order term is neglected and Equation (2.4) can be rearranged as:

$$V = \frac{dM}{dx} - P\frac{dy}{dx} \tag{2.5}$$

Considering a case where there is no shearing force, nor beam shortening, the differential equation for the curvature of the axis of the beam is:

$$EI\frac{d^2y}{dx^2} = -M \tag{2.6}$$

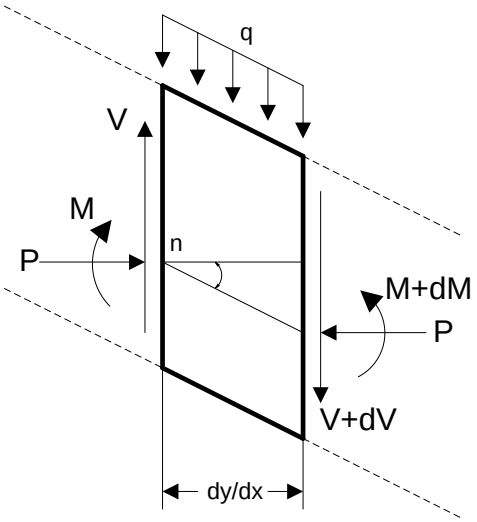

Figure 2.2. Axial force, shearing force, and bending moment of a small section in a beam under axial compressive force P. The figure was reproduced from [Timoshenko 1961].

And from Figure 2.3(a), at any cross section of the beam, bending moment is:

$$M = -P(\delta - y) \tag{2.7}$$

Substituting Equation (2.7) into (2.6), we obtain:

$$EI\frac{d^2y}{dx^2} = P(\delta - y) \tag{2.8}$$

$$\frac{d^2y}{dx^2} = \frac{P\delta}{EI} - \frac{Py}{EI} \tag{2.9}$$

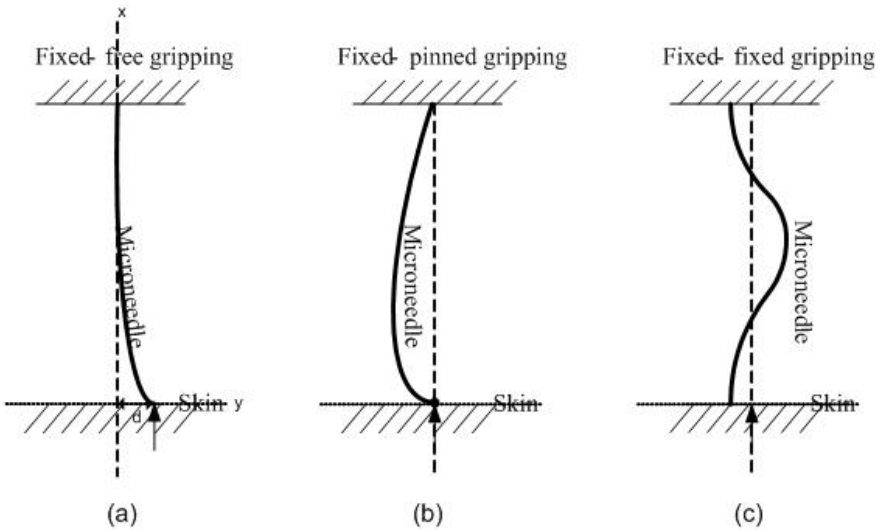

Figure 2.3. The three end condition in beam and column theory, reproduced from (Timoshenko & Gere, 1961). (a) One end fixed, another end free. (b) One end fixed, another end pinned. (c) Both ends fixed.

Let $k^2 = \frac{P}{EI}$, Equation (2.9) becomes:

$$\frac{d^2y}{dx^2} + k^2y = k^2\delta \tag{2.10}$$

The above equation has a general solution in the following form:

$$y = Acos(kx) + Bsin(kx) + \delta \tag{2.11}$$

Now, let's look at the most simple case where one end of the beam is fixed, and another is free. The boundary conditions at the "built in" end of the beam are as shown by the following.

$$y = 0, \text{ at } x = 0 \tag{2.12}$$

$$\frac{dy}{dx} = 0, \text{ at } x = 0 \tag{2.13}$$

Substitute Equation (2.12) into Equation (2.11) and the equation can be rewritten as:

$$0 = Acos(0) + Bsin(0) + \delta \tag{2.14}$$

Thus:

$$A = -\delta \tag{2.15}$$

We need to find another relationship in order to solve the equation. This can be obtained by differentiating Equation (2.11), i.e.:

$$0 = -kAsin(0) + kBcos(0) \tag{2.16}$$

Thus;

$$B = 0 \tag{2.17}$$

Substitute Equation (2.15) and (2.17) into (2.11), and we obtain:

$$y = -\delta \cos(kx) + 0 + \delta \tag{2.18}$$

Thus:

$$y = \delta(1 - \cos(kx)) \tag{2.19}$$

At another end where the beam is free, the condition is:

$$y = \delta, \text{ at } x = l \tag{2.20}$$

Equation (2.19) is satisfied if the term $\delta\cos(kx) = 0$. In other words, the boundary conditions are either:

$$\delta = 0 \tag{2.21}$$

Or:

$$\cos(kx) = 0 \tag{2.22}$$

If $\delta = 0$, it means there is no buckling, and deflection will be zero. On the other hand, if $\cos(kx) = 0$, this means there is buckling in the beam and $kl = (2n - 1)\frac{\pi}{2},\ n = 1, 2, 3, \ldots$

Since the smallest critical load can be found when the value kl is at smallest, which is where $n = 1$, the smallest critical load can then be derived as:

$$kl = (2n - 1)\frac{\pi}{2} = [2(1) - 1]\frac{\pi}{2} = \frac{\pi}{2} \tag{2.23}$$

Substituting $k^2 = \frac{P}{EI}$ into Equation (2.23), we obtain:

$$l\sqrt{\frac{P}{EI}} = \frac{\pi}{2} \tag{2.24}$$

And;

$$\frac{l^2 P}{EI} = \frac{\pi^2}{4} \tag{2.25}$$

Rearranging the term, the critical load for the case of *one end fixed, another end free* can be formulated as:

$$P_{cr} = \frac{\pi^2 EI}{4l^2} \tag{2.26}$$

This equation is similar to Euler formula which is in the form:

$$P_{cr} = \frac{\pi^2 EA}{(\frac{L_e}{r})^2} \tag{2.27}$$

Where A is the cross sectional area of the column. Substitute $r^2 = I/A$ into Equation (2.27) and we obtain:

$$P_{cr} = \frac{\pi^2 EI}{(L_e)^2} \tag{2.28}$$

Where L_e is the effective length which combines the actual length with end-fixity factor; $L_e = KL$, K = constant value and L = actual length of the beam. In the case of one end fixed and another end free, K = 2.0 (theory value) or 2.1 (practical value), thus $L_e = 2L$ [Mott 2008]. Substituting it into Equation (2.28) and we can get;

$$P_{cr} = \frac{\pi^2 EI}{4L^2} = \frac{0.25\pi^2 EI}{L^2} \tag{2.29}$$

This equation is similar to Equation (2.26). It is noted that L in Equation (2.29) is equal to l in Equation (2.26). If the bar has *both ends fixed*, as shown in Figure 12(c), there are reactive moments preventing the ends of the beam from rotating during buckling. Inflection points are located where the line of action of P intersects the defection curve since bending moments are zero at these points. The beam can be divided into four equal regions,

each of which is in the same condition as the beam with one end fixed and one end free. The critical load for the case of both ends fixed can be obtained by substituting *l/4* for *l* in Equation (2.26), gives:

$$P_{cr} = \frac{4\pi^2 EI}{l^2} \tag{2.30}$$

This is similar to the case of substituting $L_e = L/2$ into Equation (2.28). It should be noted that in the case of both ends fixed, $K = 0.5$ (theory value) or 0.65 (practical value). If the bar has *one end fixed, another end pinned* as shown in Figure 2.12(b), $L_e = 0.7L$. Theory value of K is 0.7 and practical value of K is 0.8. Substitute this L_e into Equation (2.28), and we obtain:

$$P_{cr} = \frac{2.04\pi^2 EI}{L^2} = \frac{2.04\pi^2 EI}{l^2} \tag{2.31}$$

It was mentioned that the use of Equation (2.26), (2.30) and (2.31) are limited due to the maximum compressive stresses [Timoshenko 1961]. It requires another computation to determine that they can be used to compute the critical load. This can be done by calculating the minimum (l / r) from

$$\sigma_{cr} = \frac{P_{cr}}{A} = \frac{\pi^2 E}{(\frac{l}{r})^2} \tag{2.32}$$

where σ_{cr} is the given critical value of the compressive stress, E is Young's modulus, and *r* represents the radius of gyration, $r = \sqrt{I/A}$ where *I* is area moment of inertia and *A* is cross sectional area. If the needle geometry in question shows larger *l* / *r* value (compared to the minimum *l* / *r* computed in Equation (2.32)), we can use Equation (2.26), (2.30) and (2.31). Otherwise, the compressive stress reaches the proportional limit before buckling and the equations are inapplicable.

Another method to check if the Euler equations can be used in this analysis is to calculate slenderness ratio (*SR*) and check if the value exceed the transition slenderness ratio, or column constant (C_c) [Mott 2008]:

$$SR = \frac{KL}{r} = \frac{L_e}{r} \tag{2.33}$$

where *K* is the end-fixity factor, *L* is the actual length of the microneedle between points of support or lateral restraint, L_e is the effective length, and *r* is the smallest radius of gyration of the cross section of the microneedle described previously.

$$C_c = \sqrt{\frac{2\pi^2 E}{s_y}} \tag{2.34}$$

where E is modulus of elasticity and s_y is yield strength of the material. If the actual effective slenderness ratio L_e/r is greater than C_c, the microneedle is considered "long" and can be analyzed using the Euler formula (Equation (2.26), (2.30) and (2.31)). Otherwise, the column is considered "short" and should be analyzed by J. B. Johnson formula as shown by the following.

$$P_{cr} = As_y \left[1 - \frac{s_y(\frac{L_e}{r})^2}{4\pi^2 E}\right] \tag{2.35}$$

Now, consider the case of *uniform varying cross section* beam, e.g. conic beam. Under axial load with one end fixed, another end free fixity, the critical load can be computed by

$$P_{cr} = \frac{mEI_2}{l^2} \tag{2.36}$$

Where P_{cr} is the critical load, E is Young's modulus, I_2 is the moment of inertia at the lower end of the column (in our case, it's the bottom of microneedle), m is the integer number depending on ratio of I_1 and I_2, and can be found [Timoshenko 1961].

Buckling is the primary mode of failure often found in microneedles. The determination whether a microneedle will buckle or not is mainly dependent on two parameters including geometry and dimension of microneedle, and physical properties of the soft tissue. We have shown in this section that if a microneedle is subjected to an axial force

larger than the critical buckling load, it may suffer from buckling. Now, to determine the magnitude of such force, one may either collect the data from microneedle insertion experiment, or develop a physical-based method to predict the force applied to microneedle during the insertion.

Physical-based methods have been widely used in predicting the behaviors of soft materials including skin and other soft tissues. A brief introduction on these methods is presented in the next section.

2.6 Soft tissue modeling method

2.6.1 History of soft tissue study

Property of soft tissues is one of the most important elements in needle insertion as its interaction with the needle could change the course of the needle or damage it due to buckling or bending. Studies of soft tissue properties can be performed through indentation by applicators [Hayes 1972, Zhang 1997], cutting by knives or scissor [Greenish 2002], penetration by needles [Kobayashi 2005], applying tension [Miller 2002], applying compression [Sakuma 2003, Miller 2000, Bergstorm 2001], or non-invasive methods such as aspiration experiment [Nava 2004], and elastography (the measurement of soft tissue elasticity by imaging technique such as ultrasound or MRI) [Greenleaf 2003]. These studies have been conducted on porcine brain [Miller 2002], articular cartilage [Sokoloff 1966, Mow 1989], skin with subcutaneous tissues [Bader 1983, Reynolds 1992, Mak 1994, Vannah 1996], bovine liver [Liu 2000], porcine liver [Hu 2004, Kobayashi 2005, Sakuma 2003], human liver [Nava 2004, Carter 2001], human kidney [Nava 2004], abdominal skin [Tay

2002], and etc. The parameter that most studies used to describe the properties of soft tissues is the elasticity.

Elasticity of soft tissue can be demonstrated through parameters such as stress-strain relationship, Young's modulus or elastic modulus. Although these parameters are generally derived from experimental data [Zhang 1997, Liu 2000], some studies extract them via mathematical approach. Hayes et al developed a mathematic equation for calculating the Young's modulus of cartilage from indentation force, Poisson ratio, indentation depth, radius of the indenter, and thickness of the tested tissue [Hayes 1972]. Sakamoto later presented another mathematical method for computing the Young's modulus [Sakamoto 1996]. Local effective elastic modulus of bovine liver was derived from experimental data [Hu 2004]. Moreover, studies of other characteristics of soft tissues have been implemented such as dynamic viscoelastic and creep [Kobayashi 2005].

Factors affecting the properties of soft tissue are such as age, race, gene or diseases. It was reported earlier that the elasticity of human skin decreases over age especially after the age of 30. The thickness of skin is also influenced by aforementioned parameters and therefore has a direct effect on the skin properties [Al-Qallaf 2008, Lee 2002]. As cancerous and cirrhotic tissues appear to be stiffer than healthy tissues [Wang 1992], some diseases may also contribute to the variety of skin properties. These difficulties are the major problems that hinder the development a precise predictive model of needle and soft tissue interaction.

2.6.2 Soft tissue modeling

Since soft tissue expresses inhomogeneous, anisotropic, viscous and pseudo-elastic, nonlinear stress-strain behavior, it is very difficult to formulate them into simple mathematic function. It is therefore quite common to demonstrate the properties of soft tissue by complex mathematic or simulation model. In medical applications, soft tissue models are used in many ways such as training a surgeon, testing new equipment, planning a complex surgery, and etc. The primary reason for its growing use is probably due to limited resources for training and testing with the actual soft tissue. Several issues prohibit the use of human tissue for training, e.g. potential injury, fatality, setup cost, and ethical issue. Similarly, the use of animal tissue is expensive and controversial due to high setup cost, limited number of training allowed for each animal, different tissue properties comparing to human tissue, difficult to measure trainee performance, and etc.

Soft tissue modeling approaches can be classified into two categories; geometric-based and physical based modeling. Geometric-based modeling such as free-form deformation illustrates the deformation of an object using geometric techniques. Free-form deformation mostly conforms to user's manipulation rather than physical properties of the object. The method tends to allow the object being manipulated to have discontinuities and openings. Thus, this modeling method is not suitable for soft tissue modeling. Physical based modeling combines engineering, physics, and geometric modeling in order to create realistic-looking behavior. Physical based modeling includes chain-mail, mass-spring (MSM), finite element method (FEM), boundary element method (BEM), discontinuous free form deformation (DFFD), and mass tensor model (MTM).

Chain-mail technique models an object as a series of linked elements (chain-liked elements) [Gibson 1997, Gibson 1999, Wang 2004]. Movement of each element is constrained such that it is stretched or compressed between adjacent nodes. Although this technique is computational efficient, the deformation of chain-liked object cannot realistically approximate the deformation of soft tissue.

Mass spring model (MSM) represents an object by a set of mass points [Bielser 2000, Mohr 2003, Mollemans 2003]. Each point is connected to one another by springs as shown in Figure 2.4. Stiffness of each spring can be specified individually through a parameter called spring constant. MSM is fast (in term of computation time) since it is simple and easy to implement. This advantage makes the method become suitable for real-time computation. However, it requires large number of nodes in order to create realistic deformation. Moreover, it is difficult to convert soft tissue properties into spring constant, and setup each spring to obtain realistic deformation of the whole object. Also, in case of large degree deformation, MSM does not behave like soft tissue.

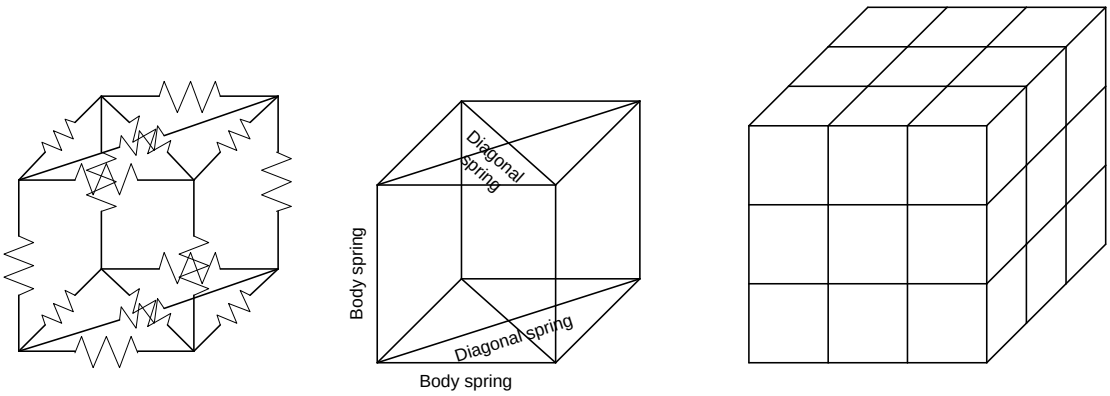

Figure 2.4. Example of mass spring model.

FEM and BEM are used to approximate continuous problem by discretizing the input model into elements [Tang 2003, Dimaio 2003]. Each element can be analyzed and the results are combined to represent global behavior. The element can be of various shapes such as triangles and quadrilateral elements (2D), or tetrahedron and hexahedron (3D). Hexahedron elements are more reliable than tetrahedron elements but generating such mesh may be more complicated and sometimes impossible. Tetrahedron elements are more suitable to complex objects but may be less accurate. Figure 2.5 shows an example of tetrahedral object. Soft tissue properties are represented by Young's modulus and Poisson ratio which can be assigned to each element individually. FEM and BEM provide accurate computation since the soft tissue properties can be transfer to the model directly, but the methods are computational expensive. It becomes a great challenge to apply these techniques to generate realistic and real time deformations. Lastly, MTM is a hybrid model between FEM and MSM [Mollemans 2007]. The method combines advantages of FEM and MSM in order to create computational efficient and realistic model.

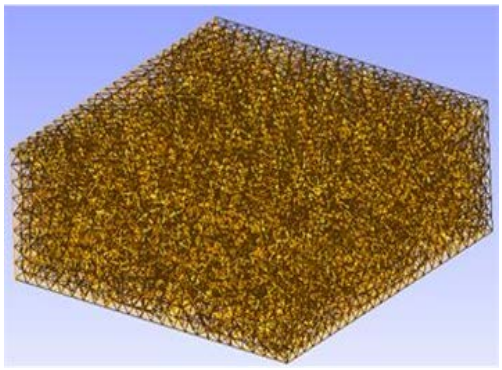

Figure 2.5. Example of tetrahedral mesh for finite element modeling [Boonma 2012a].

Soft tissue modeling is often used in an attempt to predict the amount of force applied on microneedles and the tissue deformation that determines the penetration depth. While the force is required in order to guarantee that microneedles will not break, the penetration depth is crucial to determine whether microneedles can deliver drugs successfully. However, these parameters do not quantitatively indicate how effective microneedles would be, especially in transdermal drug delivery where the performance of microneedles is measured by how well the drugs can be transported into skin. To systematically evaluate different transdermal microneedle designs, skin permeability may be considered and used in developing a measurement index.

2.7 Skin permeability

As microneedle is being developed towards clinical use, one of major concerns would be public response to the device and how it is administered. According to a recent study, the public would welcome the use of microneedle if it is at least as effective as conventional drug delivery method [Birchall 2011]. In transdermal drug delivery which is the primary target application of the device, microneedles are expected to deliver larger amount of drugs more effectively across the skin compared to traditional methods such as applying drugs directly on the skin or use of dermal patch. The amount of drug being delivered to or received by the body can be measured by a certain measurement index such as skin permeability.

Skin permeability represents the path length of a solute across a skin thickness over a period of time [Al-Qallaf 2008]. Higher permeability means the body is able to take in larger amount of drugs, making it is more efficient for the drugs to take effect and thus is more

preferable. Based on this result, determination of microneedle design aiming to achieve the best geometric parameters through the study on skin permeability should be reasonable.

A number of variables directly contribute to skin permeability and the resulting design of microneedles. They are consists of geometric parameters such as number of microneedles being used, dimensions (e.g. tip/base diameter and length), thickness of skin, properties of material and skin which are usually in the form of strength of fabricating material and elasticity respectively. The geometric parameters affect the permeability by defining the dimensions and shape of the hole caused by penetration. Thickness of skin determines penetration depth that microneedle is required to reach in order to achieve highest permeability (depth where perfect absorption is achieved).

The concept of using skin permeability to evaluate the performance of microneedles can be applied in other applications where the knowledge of the targeted soft tissue is known. For example, in treatment of brain cancer where exact amount of drug must be determined in order to minimize damage to other healthy cells in the area. Such application may be a new frontier for microneedles to play their role.

2.8 Future trends of microneedle

Due to their capability to puncture into skin or deliver drugs while causing only small damage to the surrounding soft tissue, we believe that in near future microneedles may be applied in more delicate medical procedures other than transdermal drug delivery. The future applications of microneedle may include; 1) diagnosing and treatment of certain diseases like

stroke, Parkinson's, or other brain-related diseases and, 2) activating paralyzed limb or controlling other devices such as prostheses, robots, cars, computer, and etc.

A stroke is the major cause of adult fatality and disability in the US and Europe. It is the second leading cause of fatality worldwide. A stroke is defined as a rapid loss of brain function due to malfunctions of blood supply to the brain. Such abnormalities include ischemia or the lack of blood flow, thrombosis or arterial embolism which is a type of blockage, or hemorrhage (bleeding). Intracranial hemorrhage or bleeding within a skull is one type of hemorrhage that may cause stroke. It is rooted from ruptured or leaked blood vessels. Intracranial hemorrhage severely increases pressure inside the skull. If this persists, it will eventually lead to swelling and shifting of the brain down through the small hole at the base of the skull. This is known as brain herniation or cistern obliteration. The parts of the brain that are compressed with the bones around this opening stop working due to accumulated stress. Since these parts of the brain control breathing and heart rate, intracranial hemorrhage can result in death.

Treatment of intracranial hemorrhage typically involves removal of bleeding part or decompressive craniectomy where a part of skull is removed to relieve the pressure and allow the swollen part to expand. The surgery begins by removing a bone flap and using a catheter or other devices to remove the blood. The use of these traditional devices may induce a risk of infections and lead to other complications which are undesirable. The medical world is seeking therapeutic intervention such as the development of neurosurgical techniques that are minimally invasive to brain tissue [Hanley 1999].

The use of micro-devices in diagnosis and treatment of brain function has been realized in the past, as evidenced in probing and stimulation of the brain. Microprobes have been used in many applications to study neuronal tissue and to restore neuronal function [Motta 2005]. Many types of microprobes have been reported [Campbell 1991, Kovacs 1994, Ensell 1996]. Microprobes are signal recording devices that are usually formed into needle-like shape. The neural signal collected by a microprobe can be used to control robot, prosthetic limbs, and etc, while deep brain stimulation through the microprobe can eliminate the tremors associated with Parkinson's disease.

For microneedles to be used in this application, several factors must be considered. First, typical transdermal microneedles cannot be applied in the new applications directly. This is because the required cutting depth in transdermal drug delivery is much shallower (less than 200 μm) than the brain-related applications where microneedles must achieve the cutting depth of 300 - 1000 μm. For this reason, super high aspect ratio microneedles may be required. However, development of such device will not be an easy task as microneedles can be easily buckled when they retain long length. A very strong and biocompatible material will be needed.

Moreover, in such applications, it is required that microneedles must be held in place for a reasonable amount of time until the procedure is complete. Slight change in inserting location may cause severe damage to the brain and other surrounding tissues. For these reasons, microneedles built on a traditional rigid substrate may not suitable. We believe that microneedles built on a flexible substrate may be more desirable as it tends to stay on curved

surface better than a rigid one. However, the fabrication of flexible substrate is still limited to only a few materials (one of them is PDMS [Huang 2007]).

2.9 Summary

In this chapter, we briefly review various applications of microneedles, geometry, fabricating materials, and their fabrication methods. We also provide some background in the area of failure modes in microneedles, physical-based method for soft tissue modeling, and skin permeability. We believe that this summary may help the readers to understand the subsequent contexts even better and may inspire them to search for more knowledge and understandings in the area of microneedle technologies.

CHAPTER 3

MICRONEEDLE AND SOFT TISSUE INTERACTION MODELING FOR MICROINDENTATION AND MICROCUTTING IN SOFT TISSUE

This chapter presents a two-stage analytical modeling technique that can be used to model interactions between microneedle and heterogeneous soft tissue during microindentation and microcutting. The technique divides microneedle insertion process into pre-puncture and post-puncture stages and uses nonlinear finite element, fracture mechanics, and distribution load to predict the possible outcomes.

3.1 Introduction

There has been a great interest in modeling an interaction between soft tissue and rigid body over the last few decades. Its benefits are widely recognized in various fields such as surgical simulation and training, medical imaging, pre-surgical planning, and etc. Soft tissue is usually known as an extremely complex body. To characterize such intricate organ, traditional and simple modeling technique such as monotonous modeling is inadequate and does not demonstrate accurate tissue behavior. As a result, researches have introduced another technique, known as heterogeneous modeling, to represent various aspects of soft tissue.

A heterogeneous object refers to a body that possesses a number of different material compositions or illustrates different mechanical properties. It is used in several fields such as mechanical, electrical, thermal, optical, biomedical, geophysical, and etc. As of today,

heterogeneous objects are essential in modeling realistic computerized entities. An example of studies that employ this concept is a surgical simulation system introduced by [Lin 2008].

A primary purpose of developing soft tissue model is to create a computerized mock up entity that is able to illustrate realistic graphic and physical behaviors, while minimizes computation resources required to complete the tasks. To achieve the goal, several modeling schemes such as heuristics, continuum, and hybrid approaches, have been studied but yet to satisfy all requirements. We will briefly introduce these methods and point out their pros and cons. This review later becomes a factor that helps us to select a technique used in developing our soft tissue model.

Heuristics approaches consist of deformable spline, chain mail, and mass spring model (MSM). They are simpler and easier to implement compared to continuum or hybrid techniques. In an object created using a heuristics approach, elements are typically represented by a number of nodes connected by springs. From these links, a system of equations can be constructed and easily solved by a computer. The major disadvantage, however, is the lack of volumetric information, such as difficulty of setting stiffness and poisson parameter for each spring to mimic soft tissue properties. This flaw lessens the accuracy of demonstrating realistic behavior of the object being modeled.

Finite Element Method (FEM) and Boundary Element Method (BEM) – based modeling are good examples of continuum approaches. The main concept of the methods falling within this category is to divide the object into several small elements. Then, a system of equations is constructed. After defining unknown, known variables, and boundary conditions, approximated solution can be drawn by solving a large sparse matrix system. The

major advantage of the continuum approaches is the realistic demonstration of the created model. This can be obtained since the techniques allow property defining inputs such as Young's modulus and Poisson ratio. Despite of this benefit, the continuum approaches suffer greatly from computational expensiveness. Since the techniques require solving a system of equations, they consume and require a large memory cluster, for a considerable long run time. This creates difficulties or hinders implementation of these techniques for real time simulation.

The last set of methods is called hybrid methods. An example of techniques that falls within this category is Discontinuous Free Form Deformation (DFFD). These methods combine advantages of both heuristic and continuum approaches in order to achieve fast computation and reasonable accuracy. Most hybrid methods employ the concept of FEM to pre-compute a motion response of the soft tissue and encode it into simulation module to illustrate soft tissue interaction.

In this chapter, we will first introduce a modeling technique that can be used to develop a heterogeneous soft tissue model for microindentation simulation. Then, we will introduce a nonlinear finite element for microneedle and soft tissue interaction modeling during the pre-puncture stage. Finally, a cutting force model based on distribution load will be presented for predicting the cutting force during post-puncture.

The remainder of this chapter is organized as follows. Section 3.2 provides an overview of soft tissue modeling in microindentation and microcutting. Section 3.3 introduces microneedle and heterogeneous soft tissue modeling. The smallest building block in the models is four-node tetrahedron. Tissue properties are explicitly assigned to each

element. The data structure of tetrahedrons, triangles, and nodes is also discussed in this section. Section 3.4 describes the implementation of Nonlinear Finite Element for microindentation simulation. A method of choosing contact and non-contact nodes along with boundary conditions are presented. Section 3.5 introduces puncture point determination based on fracture mechanics. Section 3.6 presents the post-puncture stage where microneedle cuts into soft tissue. The whole chapter is then summarized in Section 3.7.

3.2 Overview of microneedle insertion process.

An overview of the related processes is illustrated in Figure 3.1. The whole processes can be categorized into model preparation and indentation simulation. In model preparation, we first create a rectangular solid block using SolidWorks. Then, this block is converted to Stereolithography (STL) format by Rhinoceros. At this stage, the tissue block is represented by a triangular surface model. Next, the model is discretized into a set of four-node tetrahedral elements using Gmesh. Properties of soft tissue are then assigned to each element by determining the associated Young's modulus and Poisson ratio. At the end of model preparation stage, data structures that link nodes, triangular, and tetrahedral elements together are constructed.

The indentation simulation begins by moving the microneedle from the rest position, which is above the tissue block, to the soft tissue surface. Then, the user can determine whether he/she wants to subdivide the elements around the contact site in order to improve model resolution and achieve better graphic. After that, contact, non-contact nodes, and boundary conditions are determined. Nonlinear finite element is then employed to compute

deformation and forces at contact and non-contact nodes. The resulting deformation and force are used to create realistic graphic and to analyze microneedle design. Once a certain criteria has reached e.g. the stress at the insertion point exceeds certain threshold, the microneedle begins to puncture into skin and the cutting force can be then predicted based on the geometry of microneedle and the distributed load. Detail of this will be described in the following sections.

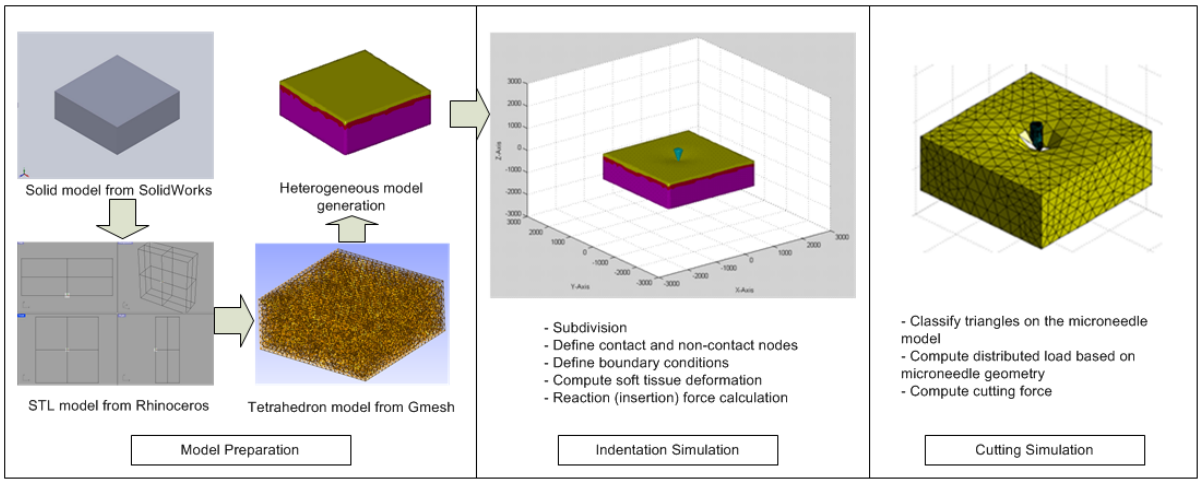

Figure 3.1. Overview of soft tissue modeling for microindentation and cutting.

3.3 Microneedle and soft tissue modeling.

In this section, we will introduce a modeling technique that can be employed to develop a computerized heterogeneous soft tissue model. First, a volumetric rectangular solid block is created using SolidWorks. The object is then forwarded to Rhinoceros and converted to a surface model represented by a collection of triangles. Next, the triangular model is saved into a Stereolithography (STL) format and transferred to Gmesh [Geuzaine 2009]. The

actual reasons that we need Rhinoceros to create and save the surface model are the following: 1) Gmesh requires surface model as an input, and 2) Rhinoceros creates a surface model that consists of triangles with better aspect ratio than those generated by SolidWorks. Once importing data, Gmesh converts the surface model into a solid one and discretizes it into several small elements including triangles and tetrahedrons. This element-full volumetric model will be used in our microindentation simulation, which will be described later in this chapter.

We will now give a brief introduction of tetrahedron element and the volumetric model made up by a large set of tetrahedrons. Although the accuracy of tetrahedral model is less than that provided by hexahedral model, it is more versatile, suitable for complex geometries and transitioning from coarsely to finely meshed regions. Soft tissue anatomy will also be reviewed in order to show the method of setting parameters that reflects mechanical properties of the soft tissue. Lastly, a data structure that links all elements together will be described.

3.3.1 Tetrahedron element and volumetric soft tissue model

A tetrahedron is a form of polyhedrons with four nodes and triangular faces, and six edges. In other words, a tetrahedron is an extension of triangles in third dimension. If it is arranged properly, a set of five tetrahedrons can form a hexahedron (a polyhedron with six faces or a cube). It should be noted that in our study the nodes in any tetrahedron must be arranged according to the right hand rule. A tetrahedron formed in accordance with this statement is shown in Figure 3.2. For example, given a tetrahedron with four nodes P_1, P_2, P_3

and P_4, if we visit node P_1, P_2, P_3 respectively and in counterclockwise direction, node P_4 will be located in the positive direction of normal vector of the plane $\langle P_1, P_2, P_3 \rangle$.

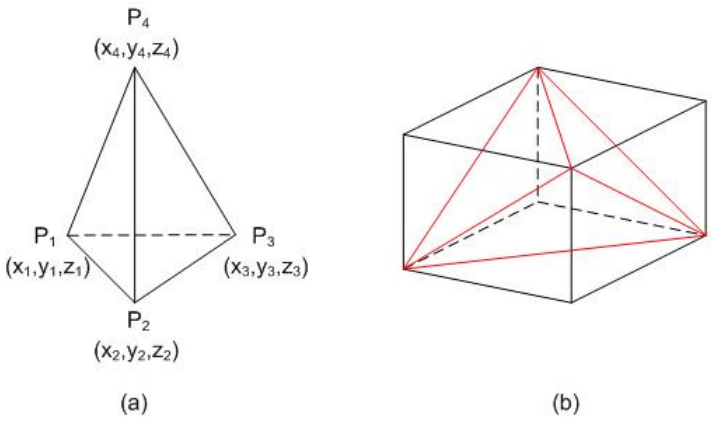

Figure 3.2. A four-node tetrahedron consists of four triangular faces and six edges. (a) A tetrahedron whose nodes are described by the right hand rule. (b) A hexahedron can be formed by five tetrahedrons.

As we have described earlier, a tetrahedral model can be constructed by following the model preparation processes as shown in Figure 3.1. Volumetric soft tissue and microneedle models made up of tetrahedrons are originated by the similar approach. Figure 3.3 shows an example of such models.

In this study, a single tip microneedle is utilized instead of a multiple-tip microneedle (e.g. microneedle patch) due to model simplicity and the capability of estimating the result of multiple-tip microneedle. Since microneedles are usually made of a single material, similar parameter values that control the mechanical properties can be set to all of the tetrahedral elements inside the microneedle model. This allocation is not applicable for soft tissue though, since soft tissue consists of several different types of material. Different parameter

values must be set to tetrahedral elements accordingly in order for the tissue model to demonstrate realistic posture. In the following topic, we will discuss about anatomy of soft tissue which we hope would provide a great benefit for readers as to understand how related parameter values are allocated.

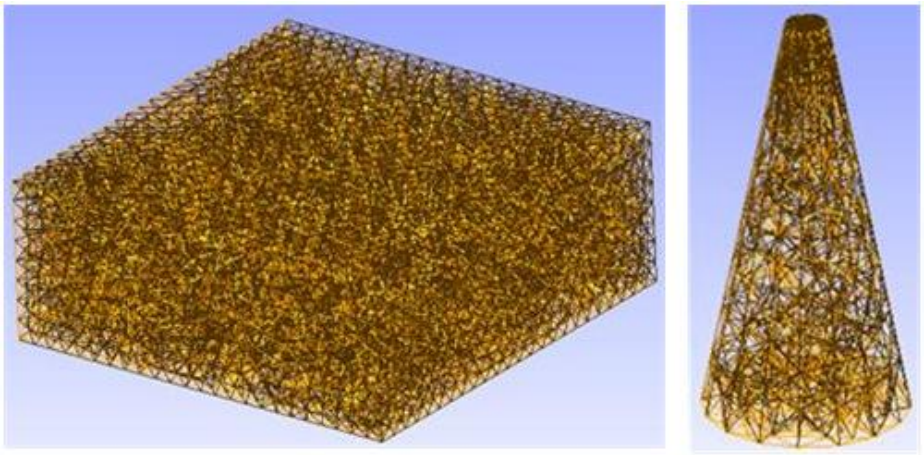

(a) (b)

Figure 3.1. An example of tetrahedral soft tissue and microneedle model. (a) Soft tissue. (b) Microneedle.

3.3.2 Soft tissue anatomy

Human soft tissue is a collection of several different types of tissues. In this study we consider only major tissue structures residing in the skin organ. More details of soft tissue anatomy were discussed earlier in Chapter 2. These structures include Stratum Corneum (SC), Epidermis (EP), and Dermis (DM). Stratum Corneum is the outermost and toughest layer of the skin. The layer is approximately 10 – 20 μm 0.01 – 0.02 mm) thick. Beneath Stratum Corneum lies the Epidermis with the thickness of about 30 – 150 micron (0.03 – 0.15 mm). The next layer is Dermis, which is approximately 1100 micron (1.1 mm) thick.

The properties of human Stratum Corneum in micro-scale were studied by [Wu 2006]. They reported that Young's modulus of human SC (in-plane measurement) is approximately 1 GPa at the extreme surface and under 100 MPa at about the depth of 10 μm. EP and DM layers have much less Young's modulus at 0.134 MPa and 0.08 MPa respectively [L'Etang 2006]. As for Poisson ratio, its value varies within short range of 0.3 – 0.5. In this study, we set the ratio to 0.4 for every type of tissue.

From this information, we set Young's modulus of 100 MPa to SC layer. Young's modulus of EP and DM layer are assigned the value of 0.134 MPa and 0.08 MPa. In order to allocate these parameters to the tissue elements, tetrahedrons must be classified into SC, EP, and DM. Any tetrahedron whose one of its node lies within 20 μm from the tissue surface is considered as SC. Tetrahedrons whose every node is located below 160 μm are assigned as DM. All the remaining tetrahedrons are set to EP. After different types of tissues are determined, the parameters are set to each element accordingly. The soft tissue model after parameters allocation is shown in Figure 3.4. The color profile illustrates different types of tissue; Yellows represent SC, Reds are EP, and Purples serve as DM. This tissue characterization is suitable especially for micro-scale soft tissue since real tissues obviously separate themselves in micro level.

The last step of model preparation stage is data structure development. This step is important for topology validation and other successive processes such as subdivision. Basically, it is the step where different types of data are linked together. Changing one piece of data, as a result, will cause the others to alter accordingly. We will discuss about how to set up the data structure next.

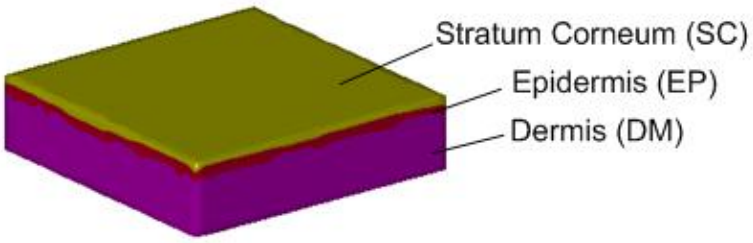

Figure 3.4. Heterogeneous soft tissue model.

3.3.3 Data structure of volumetric soft tissue model

As described previously, the elements inside the soft tissue model include tetrahedrons, triangles, and nodes. To link all three datasets systematically, special arrangement must be made. First, the basic data structures are created as follows; 1) node list, 2) tetrahedron list, and 3) triangle list. Node list is an array that holds coordinate XYZ of each node. Tetrahedron list is an array that contains positions of member nodes in node list. Member nodes must be sequenced according to the right hand rule. Triangle list is similar to tetrahedron list but each triangle has only three member nodes. Examples of node, triangle and tetrahedron list are shown in Table 3.1.

Next, the linkage between tetrahedron and triangle is developed. Considering the tetrahedron list, every three member nodes in a tetrahedron form a triangle. Switch around all nodes and four different triangles can be obtained. For example, a tetrahedron consists of node (P_1, P_2, P_3, P_4). Four node combinations that form triangles are the following; (P_1, P_2, P_3), (P_2, P_3, P_4), (P_3, P_4, P_1), and (P_4, P_1, P_2).

Lastly, we set connections between similar element, such as tetrahedron-tetrahedron or triangle-triangle. Considering tetrahedron-tetrahedron as an example, assume there are five

adjacent tetrahedrons as follows; $T_1 = (P_1, P_2, P_3, P_4)$, $T_2 = (P_1, P_2, P_3, P_5)$, $T_3 = (P_2, P_3, P_4, P_6)$, $T_4 = (P_3, P_4, P_1, P_7)$, and $T_5 = (P_4, P_1, P_2, P_8)$. Neighboring element structure for tetrahedron T_1 can be assigned as shown in table 3.2. Tetrahedron T_1 connects to tetrahedron T_2, T_3, T_4, T_5 via a face formed by nodes (P_1, P_2, P_3), (P_2, P_3, P_4), (P_3, P_4, P_1), (P_4, P_1, P_2) respectively. Links between triangle-triangle can be created in the similar fashion. Each triangle has only three neighboring triangles though.

Table 3.1. Examples of node, triangle and tetrahedron list. (a) Node list. (b) Triangle list. (c) Tetrahedron list.

NodeID	**X**	**Y**	**Z**
Node1	X1	Y1	Z1
Node2	X2	Y2	Z2
Node3	X3	Y3	Z3
…	…	…	…

TriangleID	**Node1**	**Node2**	**Node3**
Triangle1	Node1_tri1	Node2_tri1	Node3_tri1
Triangle2	Node1_tri2	Node2_tri2	Node3_tri2
Triangle3	Node1_tri3	Node2_tri3	Node3_tri3
…	…	…	…

TetrahedronID	**Node1**	**Node2**	**Node3**	**Node4**
Tetrahedron1	Node1_tet1	Node2_tet1	Node3_tet1	Node4_tet1
Tetrahedron2	Node1_tet2	Node2_tet2	Node3_tet2	Node4_tet2
Tetrahedron3	Node1_tet3	Node2_tet3	Node3_tet3	Node4_tet3
…	…	…	…	…

Table 3.2. Neighboring element structure for tetrahedron T_1.

TetrahedronID	**Node on each face**			
	P_1, P_2, P_3	**P_2, P_3, P_4**	**P_3, P_4, P_1**	**P_4, P_1, P_2**
T_1	T_2	T_3	T_4	T_5

The connections among elements do not only maintain topology of the model, they also provide better utilization of computer resources. For example, in the case of tetrahedron-triangle structure, since internal tetrahedrons cannot be seen, displaying only triangles on tetrahedron faces that do not have neighbors will obtain sufficient graphical illustration of the model. As the number of tetrahedrons is much larger than the number of triangles, displaying triangles rather than tetrahedrons significantly minimizes computational resources required by the graphic unit.

This marks the last step in model preparation, the soft tissue model is now ready for microindentation experiment. Before we begin the simulation, we will devote some of the following sections describing the computational concepts employed in our study.

3.4 Nonlinear finite element modeling for microindentation during pre-puncture

Our nonlinear strain-displacement function is developed from the traditional linear strain-displacement function. Considering a small element in two dimensions as shown in Figure 3.5, the element is displaced by the magnitudes of u and v in X and Y direction respectively at node A. Node B is dislocated by the amount of $\frac{\partial v}{\partial x}dx$ in the Y direction. Node C is relocated by a magnitude of $\frac{\partial u}{\partial y}dy$ in the X direction. Moreover, the edges AB and AC are extended by the amounts of $\frac{\partial u}{\partial x}dx$ and $\frac{\partial v}{\partial y}dy$ respectively. From this information, we can write general expressions of normal and shear strain for a small element as:

$$\varepsilon_x = \frac{\partial u}{\partial x}$$
$$\varepsilon_y = \frac{\partial v}{\partial y} \tag{3.1}$$
$$\gamma_{xy} = \frac{\partial u}{\partial y} + \frac{\partial v}{\partial x}$$

Where ε_x and ε_y are normal strains in X and Y direction, γ_{xy} is a shear strain on the XY plane.

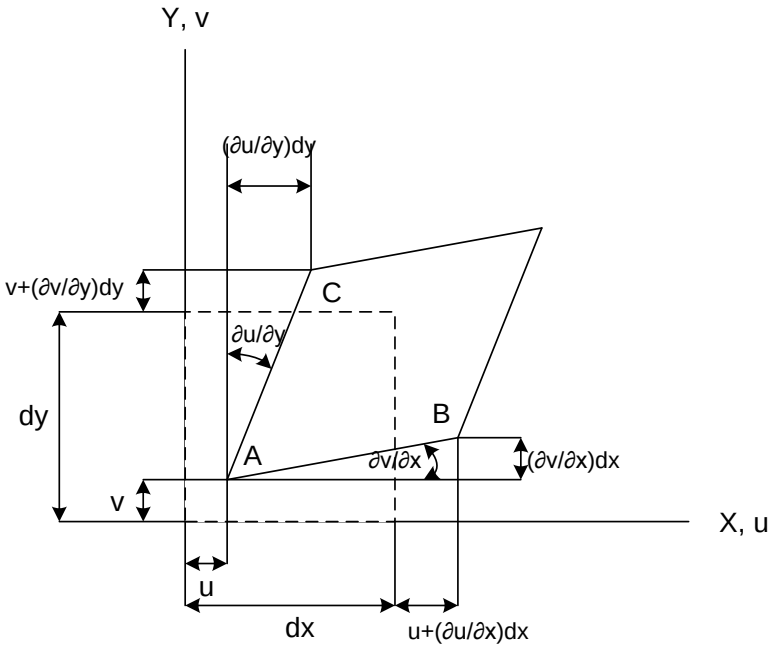

Figure 3.5. Two dimensional strains in a small element.

For a three dimensional linear elastic finite element model, we consider a small 3D element with dimensions *dx*, *dy*, and *dz* in X, Y, Z directions. Extending from the 2D case, the 3D object has three normal strains and three shear strains. The linear strain-displacement function can be formed by the following expression:

$$
\begin{aligned}
\varepsilon_x &= \frac{\partial u}{\partial x} \\
\varepsilon_y &= \frac{\partial v}{\partial y} \\
\varepsilon_x &= \frac{\partial w}{\partial z} \\
\gamma_{xy} &= \frac{\partial u}{\partial y} + \frac{\partial v}{\partial x} \\
\gamma_{yz} &= \frac{\partial v}{\partial z} + \frac{\partial w}{\partial y} \\
\gamma_{zx} &= \frac{\partial w}{\partial x} + \frac{\partial u}{\partial z}
\end{aligned}
\tag{3.2}
$$

where ε_x, ε_y, ε_z are strains defined as the unit elongation of the elastic body in the direction X, Y, Z of the Cartesian space respectively. The terms γ_{xy}, γ_{yz}, and γ_{zx} are shear strains defined as the distortion of the angle between XZ-YZ, YX-ZX, ZY-XY planes.

It has been widely known that soft tissue typically shows nonlinear effects and could be illustrated by a polynomial model [Fung 1984]. In our case, to implement nonlinear relationship, we select and add quadratic terms into Equation (3.2). This method has been introduced in a previous work presented by [Yan 2007]. After modified, the strains and shears strains are now nonlinearly dependent to nodal displacement and can be expressed by the following form.

$$
\begin{aligned}
\varepsilon_x &= \frac{\partial u}{\partial x} + \frac{1}{2}\left[\left(\frac{\partial u}{\partial x}\right)^2 + \left(\frac{\partial v}{\partial x}\right)^2 + \left(\frac{\partial w}{\partial x}\right)^2\right] \\
\varepsilon_y &= \frac{\partial v}{\partial y} + \frac{1}{2}\left[\left(\frac{\partial u}{\partial x}\right)^2 + \left(\frac{\partial v}{\partial x}\right)^2 + \left(\frac{\partial w}{\partial x}\right)^2\right] \\
\varepsilon_x &= \frac{\partial w}{\partial z} + \frac{1}{2}\left[\left(\frac{\partial u}{\partial x}\right)^2 + \left(\frac{\partial v}{\partial x}\right)^2 + \left(\frac{\partial w}{\partial x}\right)^2\right] \\
\gamma_{xy} &= \frac{\partial u}{\partial y} + \frac{\partial v}{\partial x} + \frac{\partial u}{\partial y}\frac{\partial u}{\partial x} + \frac{\partial v}{\partial y}\frac{\partial v}{\partial x} + \frac{\partial w}{\partial y}\frac{\partial w}{\partial x} \\
\gamma_{yz} &= \frac{\partial v}{\partial z} + \frac{\partial w}{\partial y} + \frac{\partial v}{\partial z}\frac{\partial v}{\partial y} + \frac{\partial w}{\partial z}\frac{\partial w}{\partial y} + \frac{\partial u}{\partial z}\frac{\partial u}{\partial y} \\
\gamma_{zx} &= \frac{\partial w}{\partial x} + \frac{\partial u}{\partial z} + \frac{\partial w}{\partial x}\frac{\partial w}{\partial z} + \frac{\partial u}{\partial x}\frac{\partial u}{\partial z} + \frac{\partial v}{\partial x}\frac{\partial v}{\partial z}
\end{aligned}
\tag{3.3}
$$

The stress $\left[\sigma_x\ \sigma_y\ \sigma_z\ \tau_{xy}\ \tau_{yz}\ \tau_{zx}\right]^T$ and strain elements $\left[\varepsilon_x\ \varepsilon_y\ \varepsilon_z\ \gamma_{xy}\ \gamma_{yz}\ \gamma_{zx}\right]^T$ are assumed to have a linear relationship between them i.e. $\sigma = D\varepsilon$, where D is called constitutive matrix and can be computed from the following:

$$
D = \frac{EG}{(1+v)(1-2v)} \tag{3.4}
$$

where E is the Young's modulus, v is the Poisson ratio, and:

$$G = \begin{bmatrix} 1-v & v & v & & & \\ v & 1-v & v & & & \\ v & v & 1-v & & & \\ & & & 0.5-v & & \\ & & & & 0.5-v & \\ & & & & & 0.5-v \end{bmatrix} \tag{3.5}$$

The stiffness matrix K of a tetrahedral element can be obtained from:

$$K = B^T DBV = \frac{EV}{(1+v)(1-v)} B^T GB \tag{3.6}$$

where *B* is a matrix relative to the position of the elements, and *V* is the volume of an element. The nonlinear strain/displacement makes the internal force dependent to nodal displacement (u(x,y,z)). The force can be formulated as:

$$K = B^T DBV = \frac{EV}{(1+v)(1-v)} B^T GB \tag{3.7}$$

where *B* is a matrix relative to the position of the elements, and *V* is the volume of an element. The nonlinear strain/displacement makes the internal force dependent to nodal displacement (u(x,y,z)). The force can be formulated as:

$$F = K \cdot u + g(u) \cdot u \tag{3.8}$$

Equation (3.8) is based on quasi-static state. We postulate that there is no acceleration and the needle is moving at constant pace. To describe how to solve Equation (3.8), we rewrite the equation in full form and obtain:

$$\begin{bmatrix} F_n \\ F_c \end{bmatrix} = \begin{bmatrix} k_{11} & k_{12} \\ k_{21} & k_{22} \end{bmatrix} \begin{bmatrix} u_n \\ u_c \end{bmatrix} + g(u) \begin{bmatrix} u_n \\ u_c \end{bmatrix} \tag{3.9}$$

where u_n and u_c is the displacement at non-contact and contact nodes respectively. F_n and F_c represent force at non-contact and contact nodes. The unknowns here are the displacements at non-contact nodes and the force at contact nodes. Equation (3.9) can be extracted further and yield:

$$F_n = k_{11}u_n + k_{12}u_c + g(u) \cdot u_n \tag{3.10}$$

$$F_c = k_{21}u_n + k_{22}u_c + g(u) \cdot u_c \tag{3.11}$$

Since F_n is zero and u_c is known, we can determine u_n by using Equation (3.10). Substitute all known variables into the equation and we eventually obtain:

$$k_{11}u_n + g(u) \cdot u_n = -k_{12}u_c \tag{3.12}$$

Solve Equation (3.12) for u_n then substitute u_n and u_c into Equation (3.11) and the force F_c at contact node can be computed. For boundary conditions, we prohibit movement of all the nodes on the side and bottom of the tissue block. Nodes on the top surface are able to move subject to external force. The movement of contact nodes, where microneedle comes in contact with, will not be restricted in XY directions. In other words, the contact nodes must be moved along Z direction together with the microneedle's tip but they can freely move in XY direction during the process.

Equations (3.10), (3.11), and (3.12) cannot be solved easily though. In this paper, we use iterative method called the Trust – Region algorithm with Powel dogleg procedure. The algorithm is embedded and ready for use through Matlab software. In general, this method is more efficient and robust than the Newton method. The function can be easily retrieved and used directly from available Matlab function module.

It should be noted here that an iterative method needs to have the initial guessed answer closest to the correct solution. The closer it gets to the correct answer, the faster and better chance that the solution is going to converge. For some simple problems, the guessed answer could be either one or zero. Our simulation, on the other hand, is a bit more complex and thus these simple guessed values should not be used as it could prolong the computation time. We therefore apply the solution obtained from the linear finite element as our initial guessed answer. From our experience, the solution converges much faster than starting from both one and zero.

3.5 Puncture point determination based on fracture mechanics

When microneedles cut into soft tissue, the cutting force of microneedles can be predicted by interchange of energy between the work created by microneedles, the work for creating the crack, and the internal strain energy due to deformation. The governing energy function may be formulated by the following equation:

$$Fdx + dU = JdA + d\Delta + d\tau + dR \tag{3.13}$$

where F is the force acting on the microneedle and dx is microneedle displacement. dU is the strain energy stored in the tissue. J is the resistance to fracture or sometimes called fracture toughness. Considering Equation (3.13), the strain energy dU stored in the tissue is ignored as the tissue not being pre-stressed. The term $d\tau$ become zero as well due to the assumption that the soft tissue will regain its original shape after removal of microneedle. Lastly the friction term dR can be ignored since, at the puncture point, microneedle just initiates the crack and there is no friction just yet. Based on these observations, Equation (3.13) can be reduced to:

$$Fdx = JdA + d\Delta \tag{3.14}$$

That is, the force at puncture can be determined by the size of the crack and the deformation of soft tissue at the time. The fracture toughness J can be computed from experimental data. A microneedle was inserted into the same spot twice. In the first time,

Equation (3.14) is still valid as all the terms contribute to the process. In the second time that the needle was pushed through the skin, Equation (3.14) must be modified as there is no energy related to initiate the crack in the tissue anymore (since the tissue was already cracked in the first cut). The modified function is formulated as the following:

$$F'dx = d\Delta \tag{3.15}$$

By substituting Equation (3.15) into (3.14), the following can be found:

$$J = \frac{(F - F')dx}{dA} \tag{3.16}$$

Puncture point is where the force on the tissue is larger than the tissue rupture force [He 2007]. Considering Equation (3.14), pressure over the cracking area can be computed by dividing the equation with (dAdx), and thus can find the following:

$$P_s = \frac{F}{dA} = \frac{J}{dx} + \frac{d\Delta}{dAdx} \tag{3.17}$$

where $d\Delta = \frac{1}{2}u^T Ku$, u is displacement matrix and K is the stiffness matrix. Substitute all the expressions into Equation (3.17), one can find the amount of critical pressure P_s or stress at the inserting point when microneedle starts to puncture into skin. According to the equation, punctuation is reach when the pressure on the soft tissue underneath the

microneedle (P_s, P_b) exceeds the critical pressure of the material (P_c), which can be obtained from the experiment.

Once the puncture force is reached, the modeling technique shifts into the post-puncture force modeling. Details of the post-puncture force analysis are discussed in the following sections.

3.6 Post puncture insertion force modeling

Post-puncture insertion force is crucial for deciding whether a needle can reach the target depth. In this study, we use the concept of distributed load to predict the forces exert to a microneedle. Since microneedle pushes soft tissue away from original position during the insertion, we postulate that the direction that soft tissue is pushed away is perpendicular to the surface of microneedle. It is also assumed that microneedle is subjected to different types of distributed loads during insertion process depending on its geometry.

Moreover, since we are modeling insertion force in micro-scale, it is assumed that gravitation force due to the mass of microneedle is ignored, and the forces on the surface of microneedle are the combination of the force that pushes soft tissue away from its position and the force resulted from friction which is relative to the surface area. Our post puncture force modeling takes advantage of the stereolithography format (STL). We select triangles as the smallest unit since most computerized model especial those retaining STL format can be either created or converted to triangular mesh easily. The relevant forces on each element are computed based on the concept of distributed load and computation geometry. Finally, the

total forces that microneedle experiences can be then determined by combining all element forces together.

Our method begins by finding triangles on microneedle surface that contribute to insertion force, which can be described in the following section.

3.6.1 Classification of triangles on microneedle surface

Considering triangles on the surface of microneedle, only some triangles actually experience the reactive forces from soft tissue. To define these triangles, we categorize all the triangles on the microneedle into the following groups based on their normal vectors and inserting direction of microneedle.

(1) Group_1 consists of triangles whose normal points perpendicularly to inserting direction

(2) Group_2 consists of triangles whose normal points to similar direction as inserting direction.

(3) Group_3 consists of triangles whose normal points to opposite direction as inserting direction.

Figure 3.6 shows these different types of triangles on microneedle models. A triangle can be categorized into group 1 if the angle between its normal vector and inserting direction is close to $\pi/2$. Triangles that are categorized into group 1 do not affect insertion force as they are on the “side” of the needle’s body and soft tissues simply “slide” over them. They,

however, may play a major role in defining friction force which could be determined by cohesion and adhesion between body fluid and microneedle's surface. At this point, we simply ignore friction effect of microneedle and focus on insertion force created by cutting only. Group 3's triangles are those lying on the "back" side of needle. They do not come in contact with soft tissue and as a result do not have any effect on insertion force.

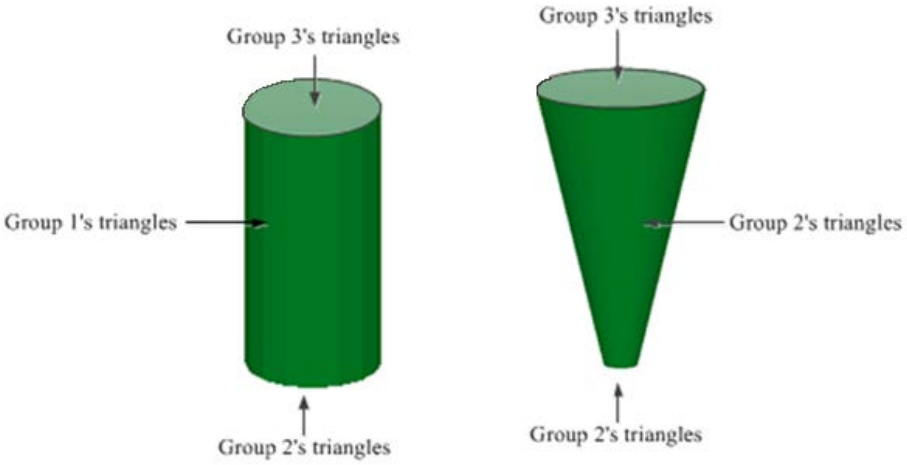

Figure 3.6. Modeling of microneedle geometries

Our focus is on group 2's triangles since they may affect the insertion force due to the "cutting" action. For special shape such as jagged needle, another condition may be included. For example, a ray casted out from at least one vertex in inserting direction should not intersect with other triangles. It should be noted that the triangles on the internal structures e.g. channel do not affect the insertion force and are not considered.

Once we obtain group 2's triangles, we will need to determine how forces are distributed on these triangles. This will be discussed in the next section.

3.6.2 Force distribution on microneedle

To model the microneedle insertion force, we first subdivide the triangles into two sub-types: α and β. As shown in Figure 3.7, α-triangles are those whose normal vectors are exactly in similar direction to insertion direction (cross product of the two vectors is close to zero). An example of α-triangles is a triangle on the tip of blunt or cone shape needles. β-triangles, on the other hand, are those whose normal vectors are deviated from the insertion direction but still points toward the insertion path (dot product of the two vectors yields positive value). An example of β-triangles is a triangle on the slope portion of cone shape needles as shown in Fig. 3.7.

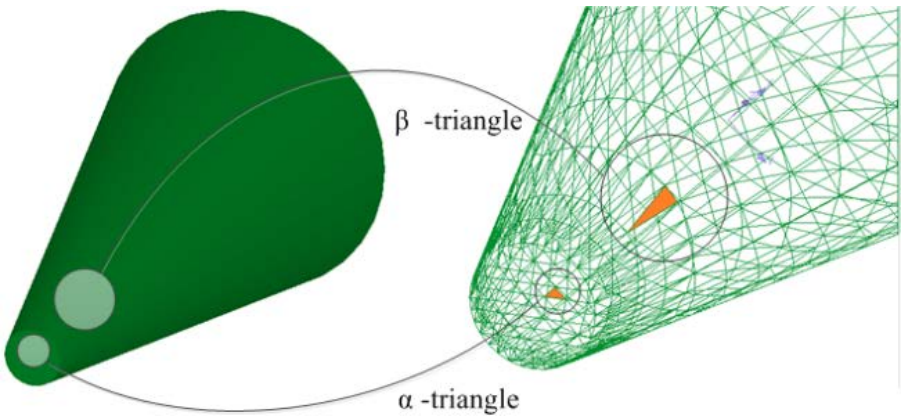

Figure 3.7. Example of α-triangles and β-triangles in cone tip microneedle.

During the insertion process, given that the surface of the tip is perpendicular to the insertion direction and the tip of microneedle is always pressed against the skin, the α-triangles lying on the tip will be subjected to uniformly distributed load across their surface area. In the meantime, the β-triangles located on the sloped body of the needle will cause

triangular distributed load. This can be portrayed by Figure 3.8, where round and blunt tip cone-shaped needles are shown on the left and right respectively.

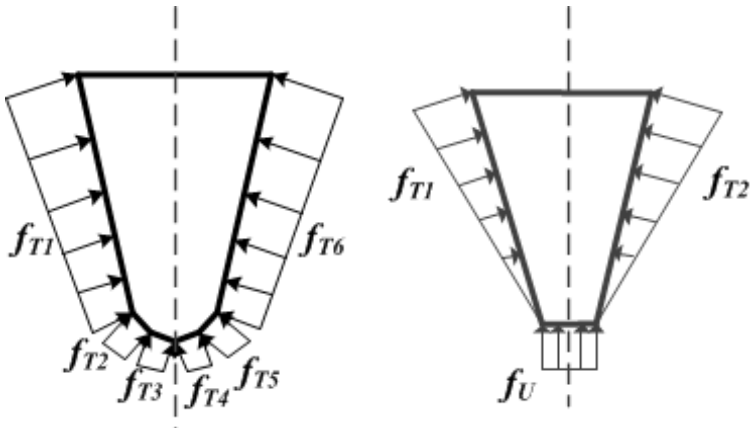

Figure 3.8. Insertion force distribution on the α- triangles and β-triangles.

Insertion force on α-triangle can be represented by a concentrated load F_U which is a computation of uniformly distributed load f_U. F_U can be computed as a load with magnitude equal to multiplication of the constant force and the area under load The general expression for resultant of uniformly distributed load is given as:

$$F_{U,i} = KS \sum_{i=1}^{n} A_i \tag{3.18}$$

where *K* is the stiffness of the skin per unit length of the needle, *S* is a scale constant defined from the experiment, A_i is area of an α-triangle *i*, *n* is total number of α-triangles at the area under uniform load. Similar to the case of α-triangle, insertion force on a β-triangle can be computed from the volume of the load over the area of the triangle. The difference,

however, is that the distributed load over a β-triangle is in a form of triangularly distributed load. This type of distributed load is dependent to location of the three vertices and distance to the needle's tip. Computation of the resulting force representing the triangularly distributed load can be divided into three cases according to these factors, as shown in Figure 3.9. In Figure 3.9(A), only one vertex of β-triangle is located at the tip of the needle. In Figure 3.9(B), two vertices of β-triangle are located at the tip of the needle. In Figure 3.9(C), none of the vertices is located at the tip of the needle.

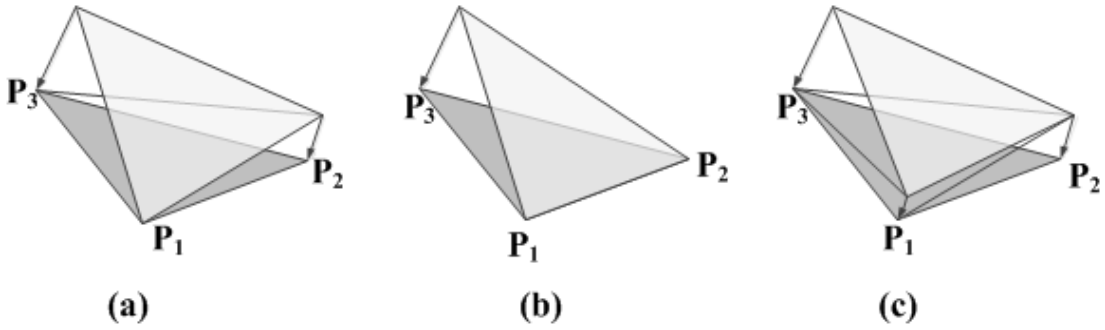

Figure 3.9. Different cases in computing distributed load on β-triangle.

To compute triangularly distributed load over a β-triangle, we first compute the distributed load on each vertex of the triangle. Considering a β-triangle *i* consisting of three vertices P_1, P_2, and P_3 as shown in Figure 3.10, if vertex P_2 is not on the needle's tip (the distributed load is not zero), the load $f_T(P_2)$ at vertex P_2 can be computed by the following procedure:

Algorithm 3.1: **Computation of distributed force on β triangle**

Input: Triangles and coordinates of all nodes
Output: Distributed force on β triangle

FIND two points (O_1, O_2) on the center axis of microneedle
COMPUTE centroid CG_i of β-triangle
COMPUTE a reference plane from O_1, O_2, and CG_i.
COMPUTE projection vertices P_1, P_2 and P_3 onto the reference plane and find the projected points Q_1, Q_2 and Q_3.
COMPUTE angle θ between the center axis $\overline{O_1O_2}$ and $\overline{Q_1Q_2}$ as shown in Figure 3.10.
COMPUTE distributed force at P_1, P_2 and P_3 using the following formulations:

$f_T(P_1) = 0$; P_1 is on the needle's tip

$f_T(P_1) = f_T(Q_1) = KS(\frac{b}{\cos(\frac{\theta_{Q2}+\theta_{Q3}}{2})})$; P_1 is not on the needle's tip

$f_T(P_2) = f_T(Q_2) = KS(a\tan\theta_{Q2} + \frac{b}{\cos\theta_{Q2}})$; P_2 is not on the needle's tip

$f_T(P_3) = f_T(Q_3) = KS(a\tan\theta_{Q3} + \frac{b}{\cos\theta_{Q3}})$; P_3 is not on the needle's tip

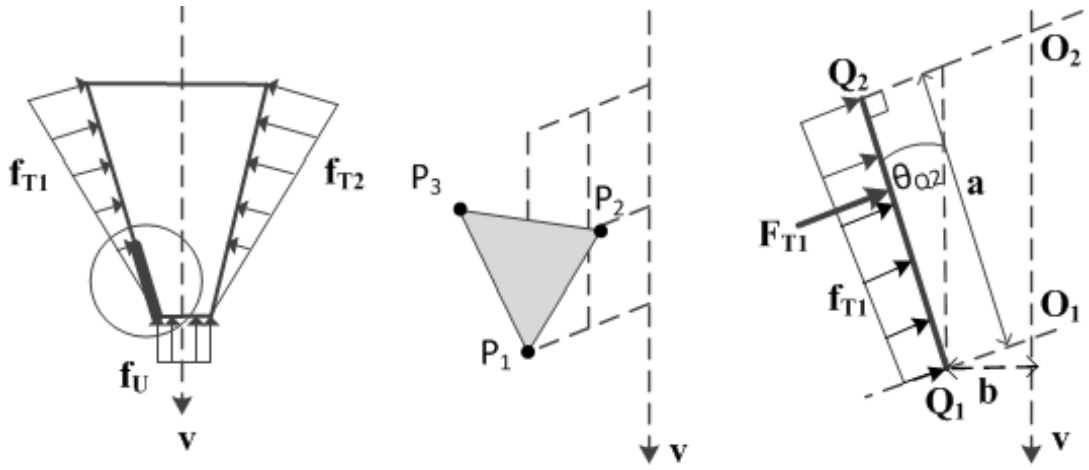

Figure 3.10. Force diagram of a triangular element (β-triangle) and the method used to compute the distributed load at each vertex.

The distributed load on the three vertices could become either one of the three cases (see Figure 3.9) that we have described earlier. The volume of a tetrahedron can be computed from its four vertices P_1, P_2, P_3, and P_4 as shown by follows.

$$V = \frac{1}{6}|(P_1 - P_4) \cdot ((P_2 - P_4) \times (P_3 - P_4))| \tag{3.19}$$

And the total volume of pentahedron which is equal to the concentrated load on the triangle can be obtained from:

$$F_T = \sum_{i=1}^{n} V_i \tag{3.20}$$

The presented techniques were developed as algorithms and implemented into a software program. Figure 3.11 shows the flowchart of the algorithm of determining the insertion force and puncture point.

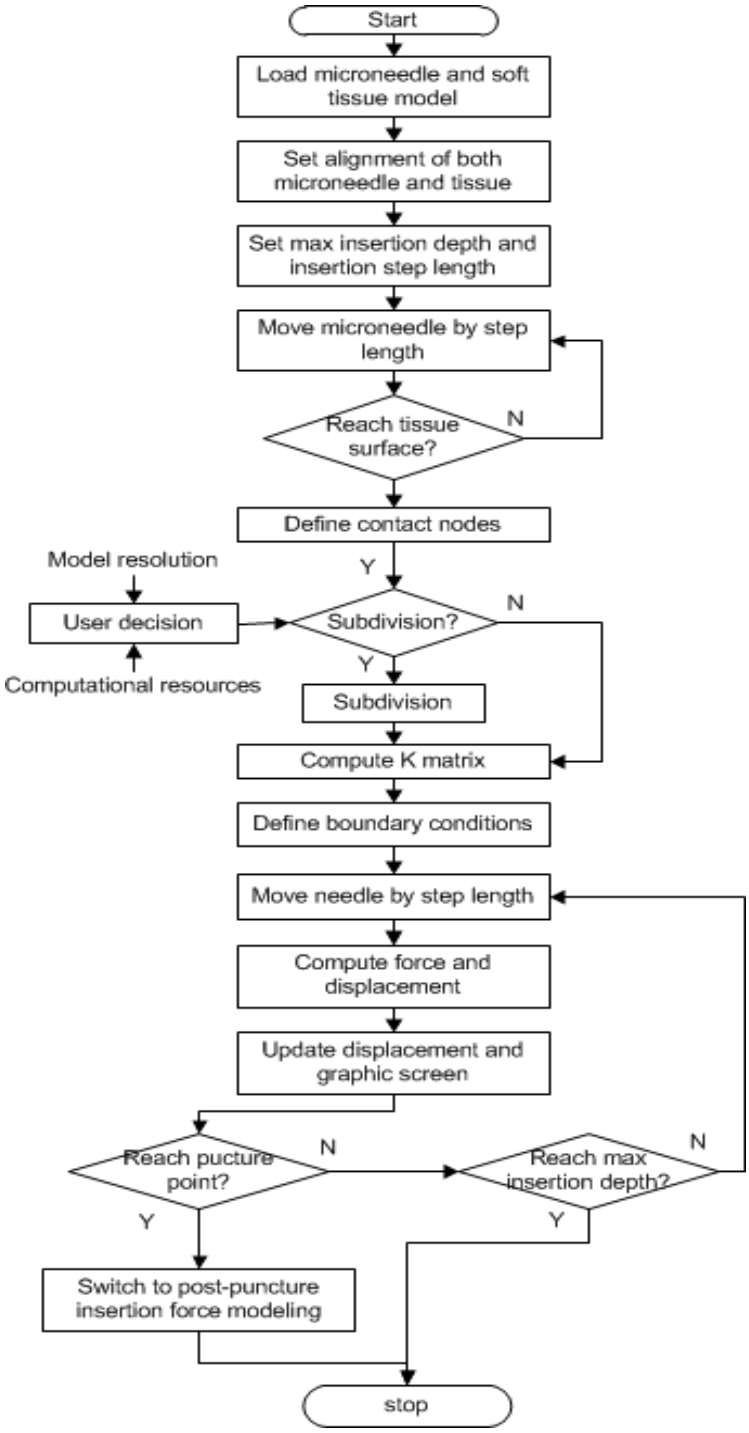

Figure 3.11. Overview of the algorithm for the insertion force computation.

3.7 Summary

In this chapter, a two-stage analytical modeling technique is presented to analyze microneedle insertion force and evaluate different microneedle designs by considering different geometric design parameters. The presented method divides microneedle insertion process into pre-puncture and post-puncture stages, and employs the concept of finite element analysis, fracture mechanics and distributed load. The method keeps track of change in forces and soft tissue deformation. Once the energy equation derived using fracture mechanic is balanced, the puncture point is reached and recorded. The insertion force during the post-puncture is lastly computed based on distributed load and computational geometry method. The presented techniques can be used for the design and development of microneedle apparatus for biomedical applications. In the next chapter, we will discuss an analytical tool that can be used to measure the performance of microneedles assuming different geometries based on skin permeation.

CHAPTER 4

ANALYTICAL MODELING AND MICRONEEDLE PERFORMANCE EVALUATION BASED ON GEOMETRY AND SKIN PERMEATION

In this chapter, an analytical performance measurement tool called Microneedle Performance Index (MPI) is presented for microneedle design and assessment. As typical microneedles are required to satisfy several criteria mostly related to safety of the patients and effectiveness of the device, MPI takes a number of design requirements into account and quantify the performance of each microneedle design based on 3D microneedle geometry and skin permeation. As a result, MPI can reduce the process and time of design analysis while providing reasonable evaluation result. The presented technique can be used in microneedle design for biomedical applications.

4.1 Introduction

In an attempt to find the most suitable design, microneedles have been fabricated into a variety of different geometries such as cylinder, cone, bevel, rectangle, and etc. Microneedle are typically required to; 1) puncture into skin without damaging itself, and 2) effectively perform its function e.g. to release drugs, create pathways, or extract some biosamples. During insertion process, a microneedle must withstand external forces generated from tissue deformation and propagation, and may suffer from structural damage due to these forces. In order to strengthen microneedles, some potential solutions involving fabricating material, needle geometry, and piercing technique were proposed.

High strength materials such as silicon, titanium and metal have been investigated and used as raw materials for microneedles [Teo 2006]. Different geometries such as cylinder, cone, and rectangular shape were analyzed by theoretical methods and finite element analysis [Aggarwal 2004]. Supporting device such as guiding mechanism was proposed in order to prevent buckling when microneedles are inserted into skin [Khumpuang 2003]. Piercing performance of the device can be also improved by increasing the speed of insertion [Verbaan 2008]. Among all the techniques, enhancing strength through geometric design is perhaps the most inexpensive and could be very effective approach. With the theory of solid mechanics and finite element method, the strength of microneedle made into different geometries can be estimated. However, it is still unclear of how to evaluate whether a microneedle can satisfy the second requirement.

According to a recent study, the public would welcome the use of microneedle if it is at least as effective as conventional drug delivery method [Birchall 2011]. In transdermal drug delivery, the effectiveness of microneedle may be measured by skin permeability which represents the path length of a solute across a skin thickness over a period of time [Al-Qallaf 2008]. Higher permeability means the body is able to take in larger amount of drugs, making it more efficient for the drugs to take effect and thus is more preferable. Therefore, measuring microneedle performance based on skin permeability should be reasonable.

McAllister et al proposed a mathematical formulation to models the permeability in skin [McAllister 2003]. Al-Qallaf et al presented a method to optimize geometric parameter of square microneedle array based on skin permeability [Al-Qallaf 2008]. However, since technique is based on the 2D annular gap, it can only evaluate microneedles that retain

uniform cross section. Olatunji et al extends the concept to optimize geometric parameter of conic microneedle array [Olatunji 2009]. Optimization of microneedle arrangement on the substrate was also presented [Al-Qallaf 2009]. These studies assume that microneedles with the given shapes are sufficiently strong, and that the whole bodies of microneedles are completely inside the soft tissue. However, this scenario may not always exist. Since soft tissue tends to deform prior to getting cut, the depth of cut is perhaps smaller than the length of microneedles. This paper presents a new method of modeling and evaluating microneedle designs, namely Microneedle Performance Index, to account for this scenerio.

In this chapter, a new method, namely the Microneedle Performance Index (MPI), is presented. The overview of MPI can be shown in Figure 4.1. Microneedle Performance Index takes the following factors into account; 1) structural stability, 2) effectiveness through permeability, 3) 3D geometry of microneedle, and 4) actual depth of cut. By combining these decisive requirements and constraints into a single measurement tool, process of design evaluation and analysis should be much shorter and more efficient. By taking 3D geometry of microneedle into account, we can extend the analysis to bevel microneedles which have never been investigated before. Although the proposed concept is demonstrated using only three geometries including cylindrical, conic, and bevel shape, the basic idea of this research can be extended to other microneedle geometries as well. Moreover, MPI can also be used to quantify the performance of microneedles in other applications where the desired cutting is different from that of transdermal drug delivery, such as in aesthetic treatment, or brain probing and stimulation [Boonma 2012c].

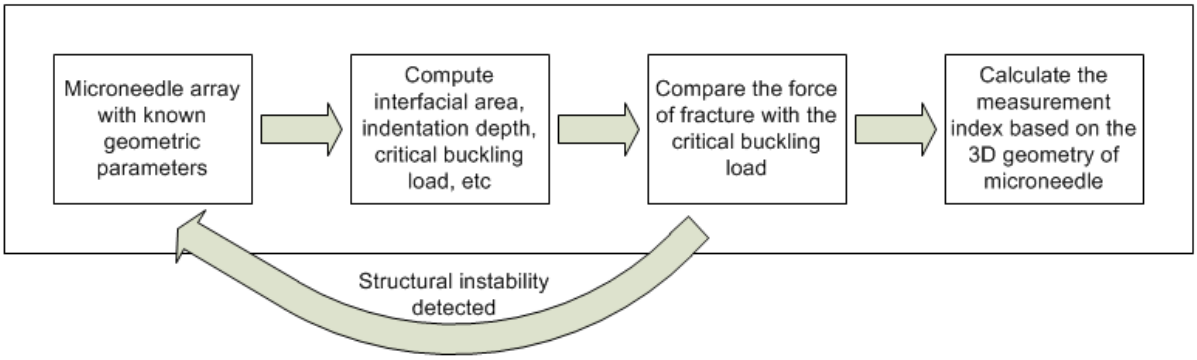

Figure 4.1. The overview of MPI computation process.

The remainder of chapter is organized as follows. Section 4.2 present how to determine actual cutting depth of microneedle based on the interfacial area. Section 4.3 presents the structural stability problem in microneedle. Section 4.4 introduces the concept of skin permeation. Section 4.5 describes how to calculate the embedded volume of microneedle. Section 4.6 defines the fractional skin volume. Section 4.7 determines the depth of ideal permeation. Section 4.8 introduces the Microneedle Performance Index. Summary is presented in Section 4.9.

4.2 Determination of actual cutting depth of microneedle

To determine the severity of skin deformation, an interaction model between microneedle and soft tissue is required. As a microneedle is pushed toward the skin, it starts to deform the surface of the soft tissue and takes resistant force generated from soft tissue deformation. Assume that microneedles are always oriented perpendicular to skin surface, actual penetration depth of microneedle can be computed by subtracting the amount of skin

deformation from the total length of the microneedle. Once the energy created by microneedle movement is large enough to initiate a crack inside the skin, the skin will yield and allow microneedle to cut inside. In our earlier works, a study on the medical surgical cutting on soft tissues was conducted and presented in [Lin 2008, Ko 2010]. Effect of microneedle geometry on the forces was previously studied in part [Kim 2010, Davis 2004, Lin 2008, Ko 2010]. And recently the microneedle and soft tissue interaction model was developed [Boonma 2012a].

Considering the mechanics of microneedle insertion into the skin where skin deformation usually appears before breakage, the force required to insert a microneedle into human skin can be modeled using fracture mechanics. Assume that the energy required for initiating a crack in the skin equal to the work created by microneedle displacement, relationship between insertion force and needle displacement can be formulated by the following equation [Davis 2004]:

$$F(d) = \alpha e^{\tau d} \tag{4.1}$$

Where α is pre-exponential constant, τ is exponential constant and d is displacement of microneedle in inserting direction. By energy balancing equation, the force *F(d)* obtained from Equation (4.1) is the force required to move the microneedle against the skin with displacement (d). And d is equivalent to the amount of skin deformation (caused by microneedle displacement) as shown in Figure 4.2.

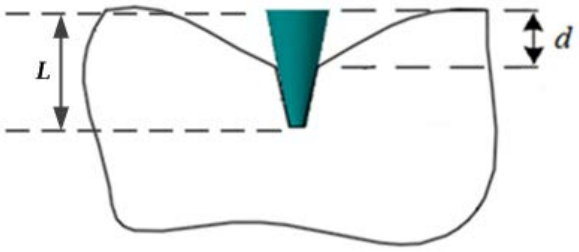

Figure 4.2. Skin deformation during the insertion of microneedle.

Also, the relationship between the force of puncture and the interfacial area of microneedle is formulated as:

$$F(A) = 0.00019A - 0.66 \tag{4.2}$$

where *F(A)* is the amount of force that a microneedle must withstand at the time that the crack begins to appear on the skin, and *A* is the interfacial area which is identical to the area on the cross section of microneedle's tip.

Since our goal is to find skin deformation before microneedle actually cuts into the skin, the relationship between needle displacement and the interfacial area is required. To achieve this, we set Equation (4.1) equal to (4.2), and rearrange the term to obtain needle displacement (*d*). This can be done since the force *F(A)* is equal to *F(d)* when microneedle punctures into skin. The final expression is then formulated as:

$$d = \left(\frac{1}{\tau}\right) \ln\left(\frac{0.00019A - 0.66}{\alpha}\right) \tag{4.3}$$

Microneedle displacement before cutting (d) is equivalent to the amount of skin deformation at the contact site. It is the distance required for a microneedle to push against the skin in order to create enough energy to penetrate into it. For Equation (4.3) to be valid, the value of the logarithmic term must be larger than 1. This implies that the minimum tip diameter that we can use to approximate skin deformation is limited to 67.4 μm. Prediction of skin deformation for a microneedle with smaller tip diameter could be estimated by linear approximation. Once skin deformation is obtained, actual cutting depth can be computed using the following equation:

$$h = L - d \tag{4.4}$$

where h is the actual cutting depth, L is the total length of the microneedle, and d is the amount of tissue deformation before crack appears. The force of puncture (Equation (4.2)) is required to determine whether a microneedle is able to satisfy the first requirement, “stability”, while the penetration depth is required to determine volume of hole in subsequent process (Equation (4.4)). In the next section, we will describe the definition of structural stability and how to justify whether a microneedle is safe to use.

4.3 Structural stability of microneedle during insertion

When a microneedle touches the skin, it behaves similar to a slender object under external loads in axial direction. One end of the needle is fixed since it is held rigidly by a substrate. Another end of the needle is similar to either free or hinge-liked object. This

phenomenon could cause buckling failure in the structure. It was reported earlier that buckling is the primary mode of failure in microneedle [Aggarwal 2004]. A threshold used to measure the ability to withstand buckling is called critical buckling load (P_{cr}). Typically, buckling will never occur if the external load applied to the structure is smaller than the critical buckling load. To compute this index, theory of elasticity in beam and column is utilized [Timoshenko 1961].

In this study, six types of microneedles are considered including solid and hollow cylindrical, conic, and bevel microneedles. Some examples of these microneedles are as shown in Figure 4.3. Critical buckling loads of these microneedles with different dimensions are obtained and compared with insertion force computed using Equation (4.2). If the critical buckling load is smaller than the insertion force, buckling in the structure is detected and microneedles are considered unable to penetrate into skin due to structural failure. This is where φ becomes zero. On the contrary, if the critical buckling load is larger than the insertion force, the external force is not large enough to cause buckling to the structure. The parameter φ therefore becomes 1. Determination of φ can be formulated as:

$$\varphi = \begin{cases} 1 & ; F < P_{cr} \\ 0 & ; F \geq P_{cr} \end{cases} \tag{4.5}$$

Critical buckling load is usually calculated from geometric parameters of microneedle. Computations of buckling load of cylindrical and conic microneedles are shown in Table 4.1, where P_{cr} is critical buckling load, E is the Young's modulus of the material, L is the length of the microneedle, I_1, I_2 are the moment of inertia at the tip and base of

microneedle respectively, *m* is a constant related to the rational between I_1 and I_2, D_1 is the diameter of the tip of microneedle, D_2 is the diameter of the base, and D_3 is the diameter of the hole inside the microneedle. The critical buckling load of bevel microneedle, on the other hand, is obtained from buckling analysis performed by SolidWorks Simulation software.

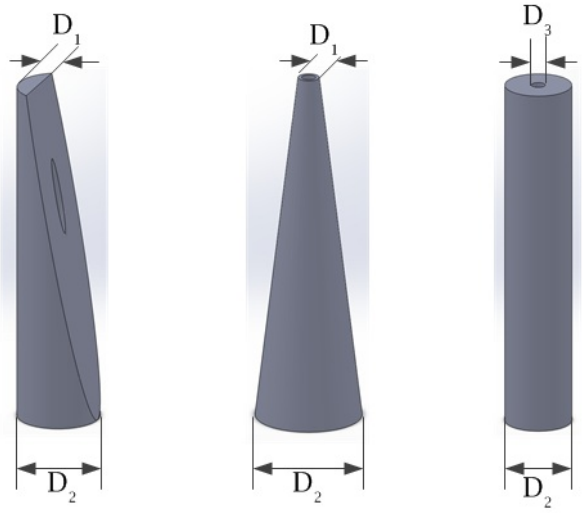

Figure 4.3. Some examples of microneedles used in this study including hollow bevel, conic, and cylindrical microneedles. Solid microneedles are not shown here as they hold similar dimensions.

If microneedles do not suffer from buckling, it should be safe to insert into skin without damage. To calculate the effectiveness of transdermal microneedles, skin permeation may be used to measure how well the given microneedles perform. We will describe how to determine skin permeation related to 3D microneedle geometry in the next section.

Table 4.1 Critical buckling load of various microneedles.

Geometry	**Critical buckling load**
Solid cylinder	$P_{cr} = \frac{0.25E\pi^3 D_2^4}{64L^2}$
Hollow cylinder	$P_{cr} = \frac{0.25E\pi^3 (D_2^4 - D_3^2)}{64L^2}$
Solid cone	$P_{cr} = \frac{mE\pi D_2^4}{64L^2}$
Hollow cone	$P_{cr} = \frac{mE\pi (D_2^4 - D_3^4)}{64L^2}$

4.4 Skin permeation during microneedle insertion

The effectiveness of drug delivery is significantly dependent on the amount of drug that can be absorbed by the body. Usually, diffusion of a substance in a medium can be represented by a parameter called permeability. By this definition, skin permeability is a term used to demonstrate the diffusion of a substance through the skin. McAllister et al proposed a mathematical formulation that is able to models the permeability in skin [McAllister 2003]. In their model as shown in Equation (4.6), skin permeation (k) is computed based on the holes created by microneedles during the cutting process:

$$k = f\frac{U}{H} \tag{4.6}$$

where f is defined as fractional skin area containing holes from microneedles, U is effective solute diffusivity within the holes, and H is the desired cutting depth where ideal

permeation is achieved (e.g. all drugs are completely absorbed). From the Equation (4.6), U is usually calculated using the Stokes-Einstein equation and may be treated as a constant [Al-Qallaf 2008]. If this is the case, then the Equation (4.6) can be simply reduced to:

$$k' = \frac{f}{H} \tag{4.7}$$

In Equation (4.7), the parameter k' is the multiplier of Equation (4.6) and can be used to represent the skin permeability. To obtain k', the fractional skin area (f) must be defined. Considering a microneedle when it penetrates the skin, there is a small space, called annular gap, between the microneedle and soft tissue surrounding it as shown in Figure 4.4. The fractional gap is usually computed from the following equation.

$$f = \frac{area\ of\ annular\ gap}{skin\ area\ under\ the\ patch} \tag{4.8}$$

It is assumed that body fluid or water will always fill this gap [McAllister 2003]. Once drug is released from the microneedle either from the coated surface or the internal pathway, the drug will mix with the biofluid and gradually diffuse through adjacent tissues. During the insertion, microneedle causes skin deformation before tearing while always oriented perpendicular to the skin surface. Since friction between microneedle and soft tissue is relatively small, the insertion force can be computed from interfacial area of microneedle's tip.

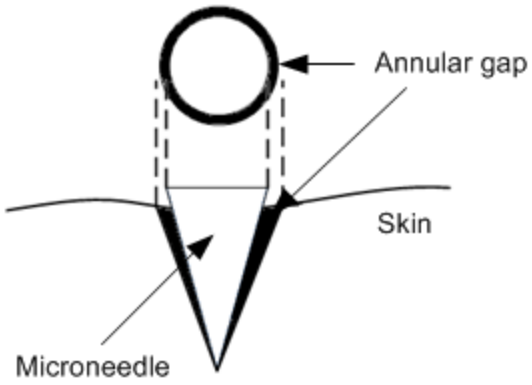

Figure 4.4. Definition of annular gap created from conic microneedle.

By the traditional definition of the fractional gap, only microneedle geometry in 2D or cross sectional plane is considered. In our case, since we want to relate microneedle geometry with fractional skin area, both numerator and denominator in Equation (4.8) are multiplied with depth of hole L_h (see definition of L_h in Figure 4.5). Although the definition of the fraction changes, its contribution in Equation (4.7) remains the same as the added terms cancel each other. The modified equation can be written as follows.

$$f = \frac{area\ of\ annular\ gap * L_h}{skin\ area\ under\ the\ patch * L_h}$$

$$f_v = \frac{volume\ of\ annular\ gap}{skin\ volume\ under\ the\ patch} \tag{4.9}$$

$$f_v = \frac{volume\ of\ annular\ gap}{skin\ volume\ under\ the\ patch}$$

From Equation (4.9), f_v is called fractional skin volume. Instead of representing it as a cylindrical volume, we postulate that the volume retains similar shape as the microneedle

being inserted. Calculation of fractional skin volume must therefore consider the geometry of the microneedle. For example, Figure 4.5 illustrates the definition of volume of annular gap for the insertion of conic and bevel microneedles. The figure shows side view of the microneedles when they are inserted into skin with the cross section of the needles at the skin surface. The dark area indicates fractional skin volume created by the microneedles. D_1 is the diameter at the tip of conic microneedle and width of circular segment at the tip of bevel microneedle respectively. D_2 is the diameter at the base of microneedle. h is the depth that microneedle penetrates into the skin (Equation 4.4). b is the diameter of conic microneedle and width of circular segment of bevel microneedle measured at skin surface. D_{h1} is diameter of the bottom of the hole. D_{h2} is the diameter of the top of the hole (at skin surface). Lastly, L_h is the depth of the hole.

The skin volume under the patch can be computed from number of microneedles in the patch and distance between each microneedle as shown by follows:

$$skin\ volume = w^2 h = n^2 P_{xy}^2 L_h \tag{4.10}$$

where w is the width of a square microneedle patch, n is the number of microneedles in each row and column on the patch, and P_{xy} is the pitch or the distance between any two microneedles in each row and column ($P_{xy} = w/n$). The definitions of these parameters are shown in Figure 4.6. Volume of annular gap can be computed by subtracting volume of the hole from the volume of microneedle that is inside the hole (embedded volume of microneedle). It should be noted that in this paper, the volume of channel inside a hollow

microneedle will not be treated as a part of annular gap volume since it is not connected directly to the surrounding skin.

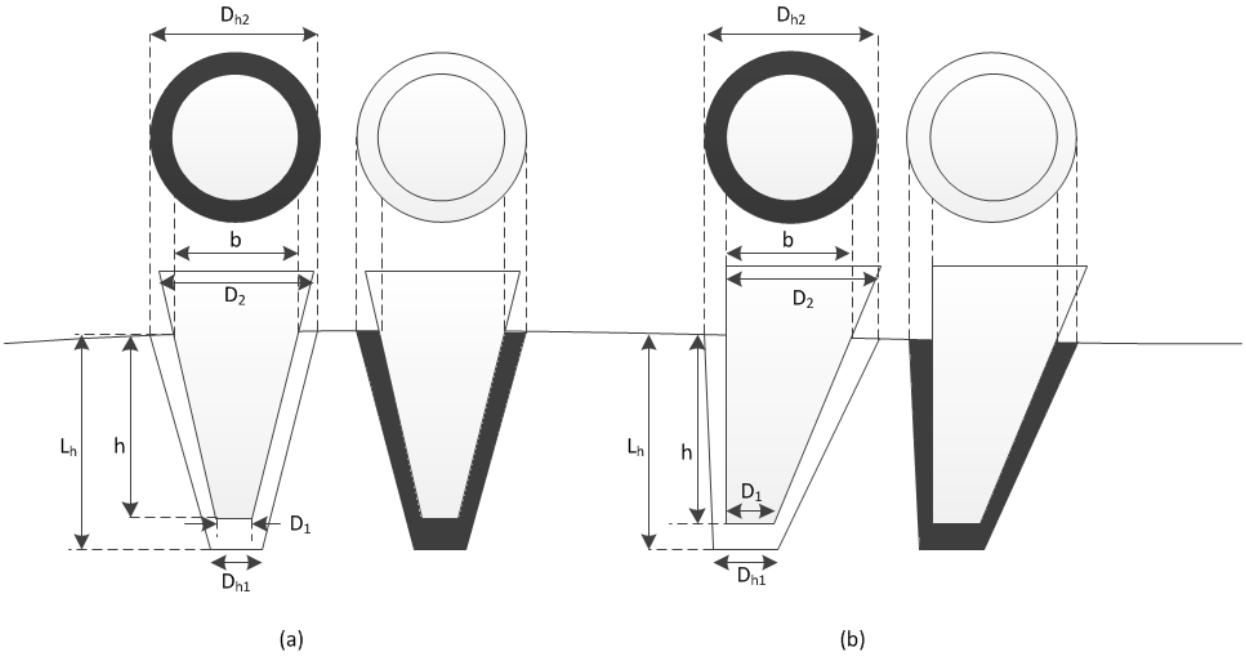

Figure 4.5. Volume of annular gap (shown by dark area) for the insertion of conic and bevel microneedles.

In general, the embedded volume can be computed based on microneedle geometry. Unfortunately some geometric parameters (such as diameter of microneedle measure at the skin surface and the length of microneedle that is inside the skin) may vary depending on how deep the microneedle penetrates inside the skin. Therefore, prior to calculating the embedded volume, it is necessary to determine the actual penetration depth of microneedle. Calculation of the embedded volume of cylinder, conic, and bevel microneedle is presented next.

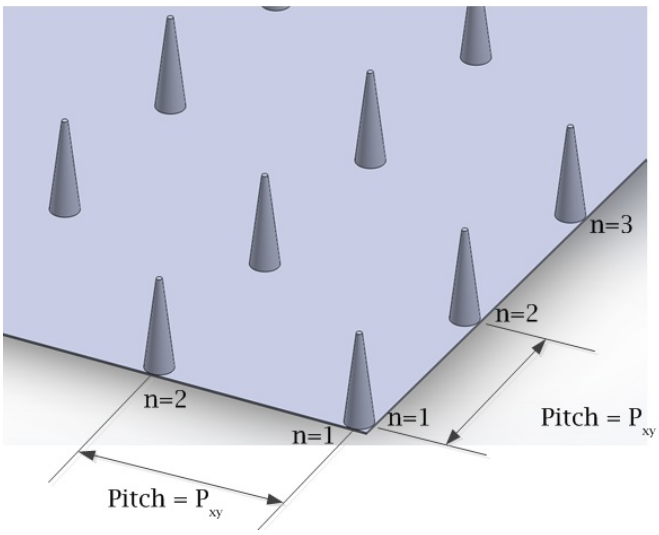

Figure 4.6. Arrangement of microneedles matrix on a square patch. Pitch (P_{xy}) is the distance between the center of any microneedle pair. *n* is number of microneedles in each row and column

4.5 Embedded volume of microneedle during insertion

The embedded volume of cylindrical microneedle can be calculated quite easily since cylindrical microneedle has constant diameter. Such parameter of conic microneedle is a bit more difficult to obtain since we need to know how much the microneedle actually penetrate into the skin. However, it is not so difficult to become a problem. The in-the-hole volume of bevel microneedle, on the contrary, is much more complicated to obtain due to the complexity of the geometry. Since bevel shape is basically created by removal of a cylinder wedge out of a full cylinder, finding volume of a cylinder wedge leads to obtaining volume of the bevel object.

A cylindrical wedge is created by cutting a cylinder with an angled plane. Equation of a plane constructed from three points e.g. [x1, y1, z1], [x2, y2, z2], and [x3, y3, z3] is usually

in a form of $\mathrm{Ax} + \mathrm{By} + \mathrm{Cz} + \mathrm{D} = 0$, where vector [A, B, C] is normal vector of the plane and can be computed from determinants as shown by follows.

$$A = \begin{vmatrix} 1 & y1 & z1 \\ 1 & y2 & z2 \\ 1 & y3 & z3 \end{vmatrix}, B = \begin{vmatrix} x1 & 1 & z1 \\ x2 & 1 & z2 \\ x3 & 1 & z3 \end{vmatrix},$$

$$C = \begin{vmatrix} x1 & y1 & 1 \\ x2 & y2 & 1 \\ x3 & y3 & 1 \end{vmatrix}, D = -\begin{vmatrix} x1 & y1 & z1 \\ x2 & y2 & z2 \\ x3 & y3 & z3 \end{vmatrix} \quad (4.11)$$

Assume that a cylindrical wedge has base width of *c*, circular segment width and length of D_1 and *2a*, and angle θ. According to Figure 4.7, if the cutting plane is defined by three points e.g. [*r, 0, L*], [*r-c, a, 0*], and [*r-c, -a, 0*], parameter *A, B, C* and *D* of this plane is computed as *-2aL, 0, 2ac*, and *2aL(r-b)* respectively. The equation of this cutting plane is as a result formulated by the following equation.

$$-Lx + cz + L(r - c) = 0 \quad (4.12)$$

To determine volume of the cylindrical wedge, the wedge object is cut into several slices by cutting planes that pass through the base of the wedge (yz planes as shown in Figure 4.7). The volume of the wedge is then computed by integrating all the slices such as:

$$Vol = \int_{r-c}^{r} z(x)y(x)dx \tag{4.13}$$

where z(x) and y(x) are derived from Equation (4.12) and equation of a circle (i.e. $x^2+y^2 = r^2$) respectively.

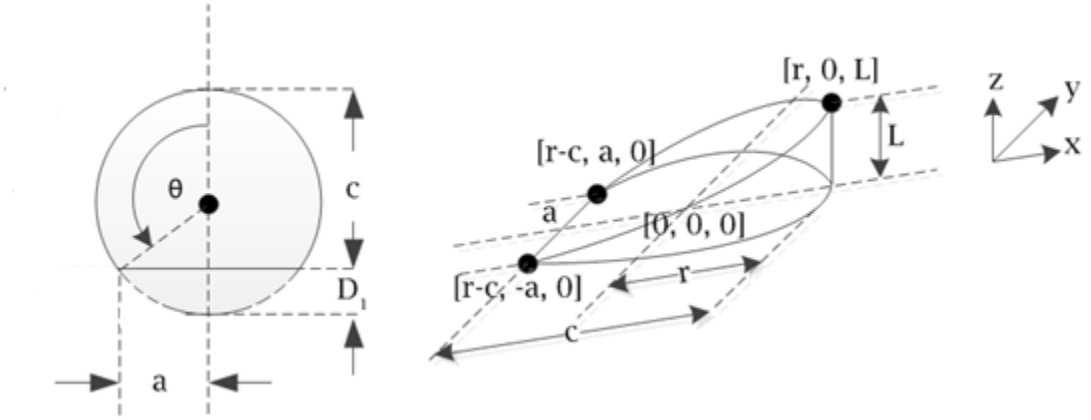

Figure 4.7. Cylindrical wedge created by cutting a cylinder with a plane that passes through three points; [*r, 0, L*], [*r-c, a, 0*], and [*r-c, -a, 0*].

Substitute z(x) and y(x) into Equation (4.13) and obtain:

$$Vol = \int_{r-c}^{r} \left[\frac{h}{c}(x - r + c)\right]\left[2\sqrt{r^2 - x^2}\right] dx \tag{4.14}$$

Therefore,

$$Vol = \frac{L}{6c}[2\sqrt{2rc - c^2}(3r^2 - 2ac + c^2) - 3\pi r^2(r - c) + 6r^2(r - c)\sin^{-1}(\frac{r - c}{c})] \quad (4.15)$$

Simplify Equation (4.15) by substituting the following terms into it (see their definitions in Figure 4.7).

$$\begin{gathered} a = r\sin\theta \\ c = r(1 - \cos\theta) \\ c^2 = 2cr - a^2 \\ \theta = \frac{\pi}{2} + \tan^{-1}\frac{c - r}{a} \end{gathered} \quad (4.16)$$

The final expression of the volume of a cylindrical wedge is therefore as shown by follows.

$$Vol = \frac{L}{3c}[a(3r^2 - a^2) + 3r^2(c - r)\theta] \quad (4.17)$$

Volume of bevel shape is then obtained by subtracting the volume of cylindrical wedge out of the volume of cylindrical shape. Figure 4.8 illustrates the process of computing volume of the embedded part of bevel microneedle in skin. All mathematical formulas used to compute the embedded volume of cylindrical, conic, and bevel microneedles are shown in Table 4.2, while Figure 4.9 shows the definitions of related parameters.

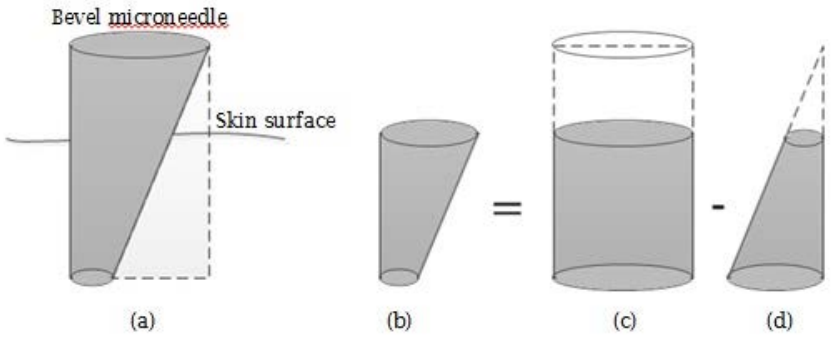

Figure 4.8. Computation of the embedded volume of bevel microneedle. (a) Bevel microneedle when it is inside the skin. (b) Embeded volume of bevel microneedle. (c) Embeded volume of cylinder microneedle. (d) Embeded volume of unwanted wedge. By subtracting (d) from (c), (b) can be obtained.

To compute the fractional skin volume of a bevel microneedle, the embedded volume that is inserted in skin (as shown in Figure 4.8(b)) is required. Figure 4.8(a) shows the full length bevel microneedle, while the solid and dash lines in figure 4.8(c) shows the extrapolated full length cylindrical microneedle. The volume of bevel needle that is inside the skin can be obtained by first computing the embedded volume of cylindrical shape (shown by solid line in Figure 4.8(c)) and then removing a cylindrical wedge out of it (shown by solid line in Figure 4.8(d)). The volume of removing cylindrical wedge is obtained by subtracting small wedge (dashed line in Figure 4.8(d)) out of the larger one (combination of both solid and dash line in Figure 4.8(d)). Volume of the large cylindrical wedge can be computed by substituting $a = \sqrt{2cr - c^2}$, $c = D_2 - D_1$ and $r = \frac{D_2}{2}$ into Equation (4.17). The final expression becomes:

$$Vol_{LW} = \frac{L}{3(D_2 - D_1)}\left[\sqrt{D_1(D_2 - D_1)}\left(\frac{3}{4}D_2^2 - D_1D_2 + D_1^2\right) + \frac{3}{4}D_2^2\left(\frac{D_2}{2} - D_1\right)\left(\frac{\pi}{2} + \tan^{-1}\frac{\frac{D_2}{2} - D_1}{\sqrt{D_1(D_2 - D_1)}}\right)\right] \quad (4.18)$$

Computation of small cylindrical wedge (as shown by dash line in Figure 4.8(d)) can be done by substituting $a = \sqrt{2cr - c^2}$, $c = \frac{D_2 - D_1}{L}(L - h)$ and $r = \frac{D_2}{2}$ into Equation (4.17). To avoid confusion and simplify the equation, the term $\frac{D_2 - D_1}{L}(L - h)$ is now replaced by *x*. The resulting expression is as shown by the following.

$$Vol_{SW} = \frac{L - h}{3x}\left[\sqrt{x(D_2 - x)}\left(\frac{3}{4}D_2^2 - x(D_2 - x)\right) + \frac{3}{4}D_2^2\left(x - \frac{D_2}{2}\right)\left(\frac{\pi}{2} + \tan^{-1}\frac{x - \frac{D_2}{2}}{\sqrt{x(D_2 - x)}}\right)\right] \quad (4.19)$$

Table 4.2. Mathematics formulations used to compute volumes of cylindrical, conic, and bevel microneedles that are embedded inside skin.

Type of microneedle	Embedded volume of microneedle
Cylindrical microneedle	$V_{cyl} = \frac{1}{4}\pi h D_1^2;\ D_1 = D_2$
Conic microneedle	$V_{con} = \frac{1}{12}\pi h\left[D_1^2 + D_1 b + b^2\right]$
Bevel microneedle	$V_{bev} = \frac{1}{4}\pi h D_2^2 - (Vol_{LW} - Vol_{SW})$

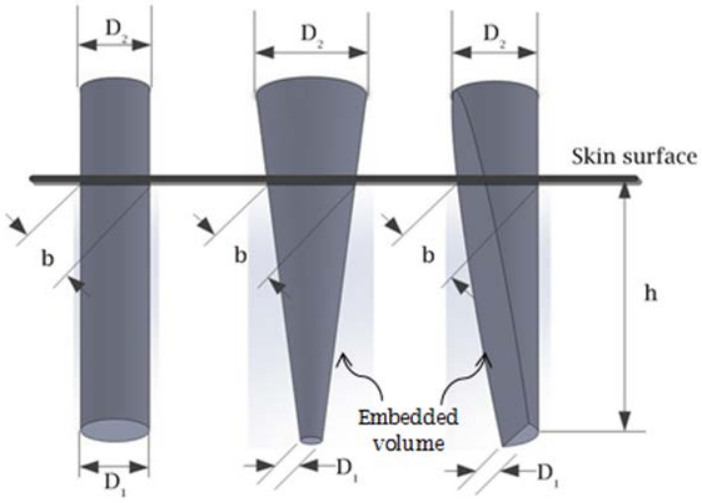

Figure 4.9. Embedded volume of different microneedles during insertion.

After the volume of the inserted part of microneedle is obtained, the volume of holes created by microneedle during the cutting process must be determined in order to calculate the annular gap and fractional skin volume.

4.6 Calculation of fractional skin volume during microneedle insertion

Volume of hole can be computed by assuming that the hole takes the shape of the microneedle being inserted. The dimension of hole is however slightly larger than the volume of microneedle since the gap portion is included. For conic microneedle, let L_h be the length of the hole embedded inside the skin, D_{h1} and D_{h2} be the hole diameters at the bottom and top of the hole, their magnitude can be computed by $L_h = h+\delta h$, $D_{h1} = D_1+\delta D_1$ and $D_{h2} = b+\delta b$, where δ represents ratio between the gap and needle dimension. The definition of δ is shown

in Figure 4.10. Hence, the total volume of the hole created by a conic microneedle can be calculated from the following formula.

$$V_{t,cone} = \frac{1}{3}\pi(h+\delta h)\left[\left(\frac{D_1}{2}+\delta\frac{D_1}{2}\right)^2+\left(\frac{D_1}{2}+\delta\frac{D_1}{2}\right)\left(\frac{b}{2}+\delta\frac{b}{2}\right)+\left(\frac{b}{2}+\delta\frac{b}{2}\right)^2\right]$$

$$V_{t,cone} = \frac{1}{12}\pi h(1+\delta)^3\left[D_1^2+D_1 b+b^2\right] \quad (4.20)$$

In case of cylindrical microneedle, the tip and base diameters of cylindrical microneedle are similar. Equation (4.20) is modified by substituting $D_1 = b = D_2$ into it. The volume of hole created by cylindrical microneedle is therefore expressed by the following equation.

$$V_{t,cyl} = \frac{1}{4}\pi h(1+\delta)^3 D_1^2 \quad (4.21)$$

For bevel microneedle, volume of hole is calculated in the similar fashion. By substituting associated length (L, h), and tip/base size (D_1, D_2) with modified values accounted for the gap between skin and microneedle ($L+\delta L$, $h+\delta h$, $D_1+\delta D_1$, and $D_2+\delta D_2$), the final formula for computing volume of hole is in the following form.

$$V_{t,bev} = (1+\delta)^3\left[\frac{1}{4}\pi h D_2^2-(Vol_{LW}-Vol_{SW})\right] \quad (4.22)$$

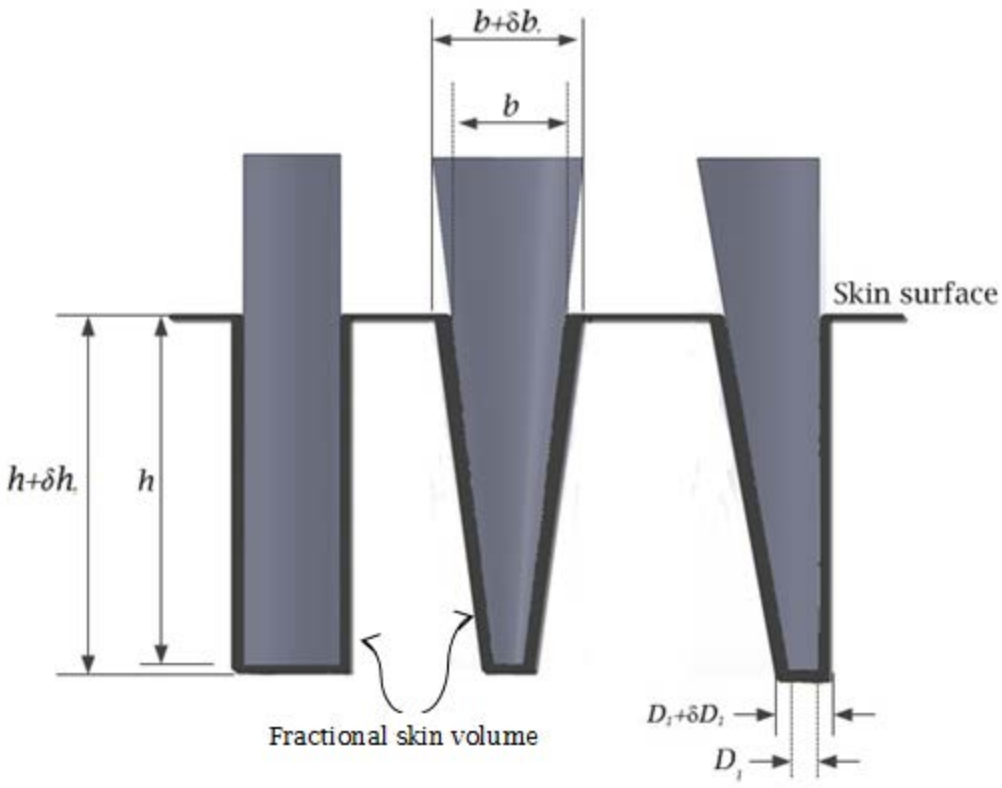

Figure 4.10. Fractional skin volume (dark area) enclosing different microneedles during insertion.

At this point, we have the volume of hole created by a microneedle and the volume of microneedle that is inside the hole. The annular gap volume can be then computed by subtraction of the two numbers. Finally the fractional skin volume (f) is computed by dividing the annular gap volume with volume of skin under the patch as shown in Equation (4.9). It should be noted that Equation (4.20) – (4.22) and the equations listed in Table 4.2 are based on only one microneedle. To compute the fractional skin volume created by the whole array, number of microneedle per patch (n^2) and the pitch distance (P_{xy}) must be considered.

Equations for computing the fractional skin volume of cylindrical, conic, and bevel microneedle arrays are listed in Table 4.3.

Table 4.3. Formulas used in computing the fractional skin volume of n^2 cylindrical, conic, and bevel microneedles.

Type of microneedle	Fractional skin volume
Cylindrical microneedle	$f_{v,cyl} = \frac{(\delta^3 + 3\delta^2 + 3\delta)\pi D_1^2}{(1+\delta)4P_{xy}^2}$
Conic microneedle	$f_{v,con} = \frac{(\delta^3 + 3\delta^2 + 3\delta)\pi\left[D_1^2 + D_1 b + b^2\right]}{(1+\delta)12P_{xy}^2}$
Bevel microneedle	$f_{v,bev} = \frac{(\delta^3 + 3\delta^2 + 3\delta)\left[\frac{1}{4}\pi h D_2^2 - (Vol_{LW} - Vol_{SW})\right]}{(1+\delta)P_{xy}^2 h}$

At this point, the required information for computing the numerator in Equation (4.7) is obtained. The denominator is the only remaining part that needs to be determined. Definition of the denominator, the ideal permeation depth, is provided in the following section.

4.7 Determination of ideal permeation depth

In the content of transdermal drug delivery, the parameter *H* in Equation (4.6) and (4.7) refers to the distance from skin surface where ideal permeation can be achieved. Simply put, this is the depth where microneedle will be most effective since the drug released from the microneedle will all be absorbed by the body. This depth is typically defined as the depth of the interface between epidermis and dermis layer or comparable to the thickness of

epidermis. By considering the way the drugs are released from microneedle, determination of *H* may be depended on whether the microneedle is solid or hollow.

In case of hollow microneedles, (assumed to have a channel through the center line similar to traditional mesoscale needles), *H* is considered as the distance that drugs need to travel through the channel in order to reach the opening at the tip of microneedle. Since drugs cannot seep through the body of microneedle, the traveling distance is equal to the length of microneedle (*L*) deducted by deformation of skin (*d*) (Figure 4.11(a)). This is valid only when microneedle is longer than the combination of epidermis thickness and indentation depth. Otherwise, drugs are released while the needle opening is still in epidermis layer and the ideal absorption cannot be achieved.

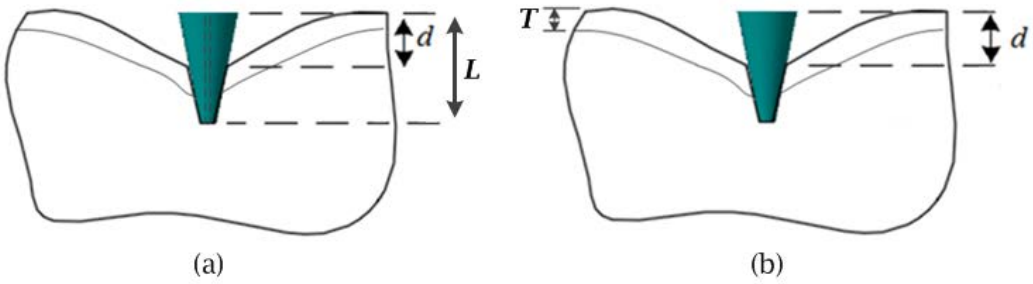

Figure 4.11. Determination of parameter *H* for (a) hollow and (b) solid microneedles.

In case of solid microneedles, drugs are usually coated on the needle surface and ready to be released to the surrounding skin. As long as the length of microneedle exceeds the combination between epidermis thicness (*T*) and skin deformation (*d*), the microneedle is considered as effective. The definitions of these parameters are shown in Figure 4.11(b).

Therefore, the parameter H in case of solid microneedle is similar to the thickness of epidermis layer. On the contrary, if the length of microneedle is less than the threshold, the microneedle cannot reach the depth where ideal absorption happens and MPI cannot be computed. In brief, the depth of ideal permeation can be determined by the following equation:

$$H = \begin{cases} T & ; L \geq d + T, solid\ needle \\ L - d & ; L \geq d + T, hollow\ needle \\ 0 & ; Otherwise \end{cases} \quad (23)$$

where L is the length of microneedle, and d is indentation depth or deformation of skin prior to being cut open by microneedle. T represents the location of the interface between epidermis and dermis layer beneath the skin which is approximately 50 μm.

In other applications, the value of H may differ from what we have described, for example, in a case where microneedles are used to create a pattern on the skin for aesthetic purpose (e.g. tattooing), or brain probing and stimulation. In aesthetic case, for the pattern to remain visible for a long time, microneedles must be able to reach a layer beneath the dermis layer. In other words, the parameter T in Equation (4.23) will be identical to the combination of the thickness of epidermis and dermis layer which would be about 1 – 2 mm.

Up to this point, all information required to determine k' in Equation (4.7) is obtained. However, k' only represents the second requirement of microneedle. In order to develop an efficient performance measurement tool, the first and second requirements, must be incorporated. The Microneedle Performance Index, which will be introduced in the

following section, combines the two requirements and thus can be used to determine the goodness of a microneedle.

4.8 Development of Microneedle Performance Index (MPI) for analysis and evaluation of microneedle during insertion

The Microneedle Performance Index can now be determined. It is postulated that the microneedle array assumes a square shape with similar number of rows and columns, and contains a total of n^2 microneedles. By substituting the fractional skin volume equations listed in Table 4.3, and the ideal permeation depth as derived in Equation (4.23) into Equation (4.7) and multiply with Equation (4.5), MPI can be written in the following expression:

$$MPI = \left[\frac{(\delta^3 + 3\delta^2 + 3\delta)}{1+\delta}\right]\frac{\varphi Q}{P_{xy}^2 H} \tag{4.24}$$

Where φ is a constant indicating the resistance of microneedle against buckling. φ is either equal to 0 or 1. The determination of can be described by buckling mode in microneedle. Recall that $P_{xy} = w/n$ where n is number of needle per row or column, w is width of the substrate, H is the desired actual penetration depth (equivalent to epidermis thickness in transdermal drug delivery application), and Q is the remaining terms of the fractional skin volume (f) as shown in Table 4.4.

Table 4.4. Definition of parameter Q based on microneedle geometry

Type of microneedle	**Parameter Q**
Cylindrical microneedle	$Q_{cyl} = \frac{\pi}{4} D_1^2$
Conic microneedle	$Q_{con} = \frac{\pi}{12}\left[D_1^2 + D_1 b + b^2\right]$
Bevel microneedle	$Q_{bev} = \frac{1}{4}\pi D_2^2 - \frac{(Vol_{LW} - Vol_{SW})}{h}$

Since the δ terms remain constant for all geometries being tested, they are eliminated from the equation. Equation (4.24) as a result is reduced to;

$$MPI = \frac{\varphi Q}{P_{xy}^2 H} \tag{4.25}$$

By maximizing Equation (4.25) subjected to geometric constraints, the design parameters of microneedle array that maximizes Microneedle Performance Index can be obtained. The geometric constraints may include but not limited to the following. The diameter at the tip (D_1) must be less than or equal to the diameter at the base (D_2) of the microneedles. D_3 which is the diameter of the pathway inside the microneedles must be smaller than both D_1 and D_2. L must be larger than summation of the depth of ideal permeation (H) and the amount of tissue deformation (d) or the microneedles never penetrate deep enough into skin. The insertion force at penetration depth must be smaller than the critical buckling load or the microneedles are damaged before puncture. Lastly, the size of

the patch must be large enough for the specific number of microneedles. These constraints may be expressed as the following.

$$L \geq d + H$$
$$F < P_{cr}$$
$$D_1 \leq D_2$$
$$D_3 < D_1 \,\&\, D_3 < D_2$$
$$w \geq 3n \cdot D_2$$

A system of equations is developed based on the objective function and constraints described above. Prior to solving for the objective function, every input value of related variables is considered and checked whether all the constraints are satisfied. If any of the constraints is violated, the associated variables are skipped and new set of such parameters are reviewed. Geometric parameters that result in highest permeability are recorded. Overview of the computation procedure is illustrated in Figure 4.12. This method is comparable to a brute force method where all possible solutions are examined. The algorithm guarantees to obtain the best global solution in exchange of exhaustive search and computation time.

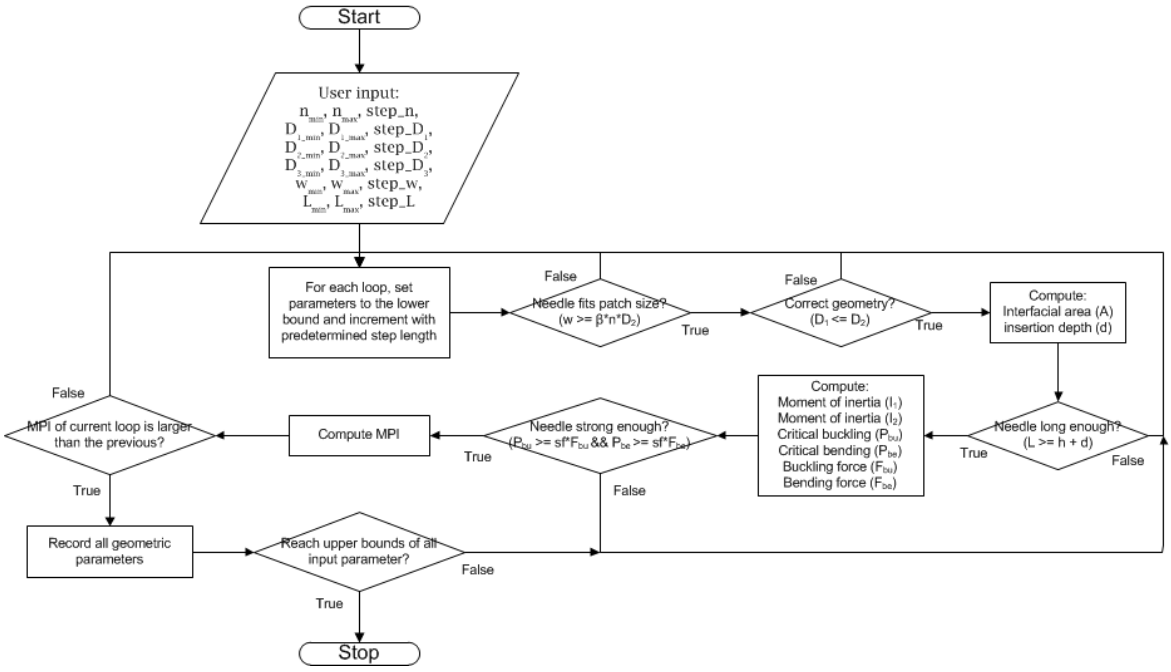

Figure 4.12. Computation procedure for obtaining geometric parameters of microneedle array that maximize the Microneedle Performance Index.

4.9 Summary

In this chapter, a new method to analyze and evaluate microneedle designs is presented. The Microneedle Performance Index can be used to quantify whether a microneedle is able to satisfy structural stability and skin permeability requirements. By predicting the cutting depth, 3D geometry of microneedle can be applied in the performance analysis. MPI is relatively simple and can be extended to other microneedle geometries. It can be used in microneedle and biomedical device design and analysis. In the next chapter, we will discuss an energy based surface fitting technique that can be used for design and assessment of new type of microneedle array.

CHAPTER 5

ENERGY BASED SURFACE FITTING FOR FLEXIBLE MICRONEEDLE PATCH DESIGN

In this chapter, a modeling technique that can be used to create and fit a flexible microneedle patch onto al skin is presented. Microneedle patch is represented by a mass spring system. A 3D surface fitting techniques is presented for fitting a set of mass nodes onto the skin surface based on the geodesic distance and the energy minimization. Analysis and evaluation method of the microneedle patch based on Microneedle Permeability Index (MPI) is also presented. The proposed technique can be used in design and analysis of biomedical devices.

5.1 Introduction

An array of microneedles fabricated on a soft substrate, known as deformable or flexible microneedle patch (Figure 5.1(a)), was introduced as a promising substitute for the traditional transdermal microneedle patch. Transdermal microneedle array is usually developed on a rigid substrate such as silicon wafer (Figure 5.1(b)). Although, it provides robust supporting structure and easy handling, a rigid patch tends to displace and eventually fall off the skin quite easily. This is due to the fact that a hard body may not be able to account for the curvature and deformation of the soft tissue where it is attached to. A possible solution to this problem is to use adhesive materials to help in fixing the microneedle patch with the skin. However, the use of adhesive materials may impose several other problems.

For example, glue that gets mixed with drug and absorbed into the body may be aggregated and eventually be harmful. Microneedle patch with highly adhesive material may be difficult to remove and the removal process may damage the needles. Moreover, it may leave some residues that may cause irritation or other side effects to the skin. These problems are very important in transdermal drug delivery and could be even more crucial in specific part of the body such as brain.

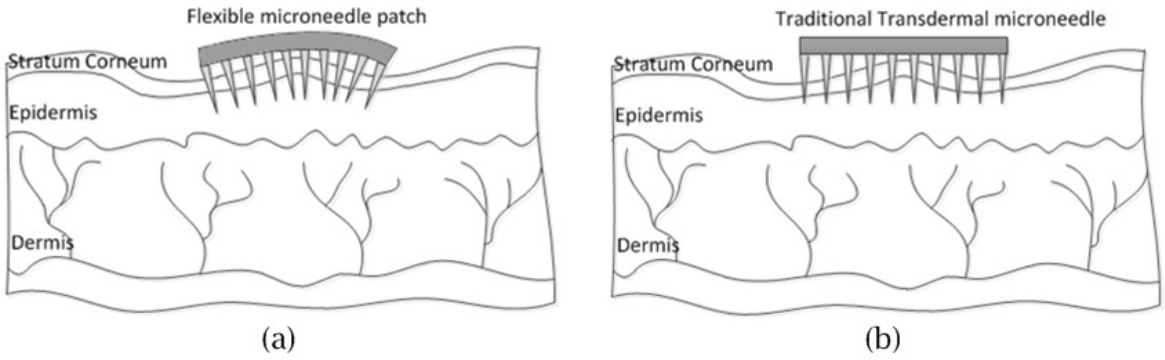

Figure 5.1. Transdermal microneedle patches. (a) Flexible microneedle patch. (b) Rigid microneedle patch.

Some microneedle applications can be found in brain-related surgery. The use of needle-liked microdevices has been long performed in brain-related applications including brain probing and stimulation. For example, microprobes or electrodes have been used in diagnosing and treatment of certain diseases like Parkinson's. Or, they can be used in activating paralyzed limbs or controlling other devices such as prostheses, robots, cars, and etc. In such tasks, microprobes are inserted into the brain while maintaining minimum damage to the surrounding cells. Once they arrive at the predetermined depth, the electrodes

can detect and send the patterned neural signal emanated from neurons to external recording unit. Also, they can be used to release electrical signal to re-energize a part of the brain that has been damaged or to transmit the signal directly to the functional motor parts (e.g. muscles) in the body while bypassing the obstruction parts (e.g. damaged spinal cord).

Traditional microprobes are either in a form of single insulated wire (Figure 5.2(a)), or in-plane electrode arrays (Figure 5.2(b)). The major drawback of these devices is that each microwire can only contain one electrode. Although microprobes built with a series of electrodes were already developed in order to measure neural signal from several depths simultaneously [Motta 2005], they are still fabricated as a single unit or an in-plane bundle of several units. Since the surface of the brain is relatively large, the ability to analyze neural signals from several sites simultaneously is very important and required in order to find specific area of the brain that controls individual motor parts. Moreover, the devices are usually required to stay in place for a mid- to long-period of time in order to minimize the damage and increase the effectiveness of diagnosing and treatment. These may be difficult to achieve using traditional microprobes.

It is believed that out-of-plane or patch-liked microneedles may perform better than the traditional microprobes due to their capability of covering much larger area. This is supported by a study where multiple electrodes were fabricated in the form of array and used in recording neural signal in 2D over the target area of the brain [Maynard 1997]. However, as the brain is one of the organs that are highly sensitive and easily damaged, traditional transdermal microneedles built on a rigid substrate may not be suitable to the task. Not only the hard substrate can cause damage to the brain directly, it also tends to move away from the

original inserting position. The use of adhesive materials is prohibited as they may be harmful to the brain. In order to apply microneedles safely onto the brain, a new technique must be developed.

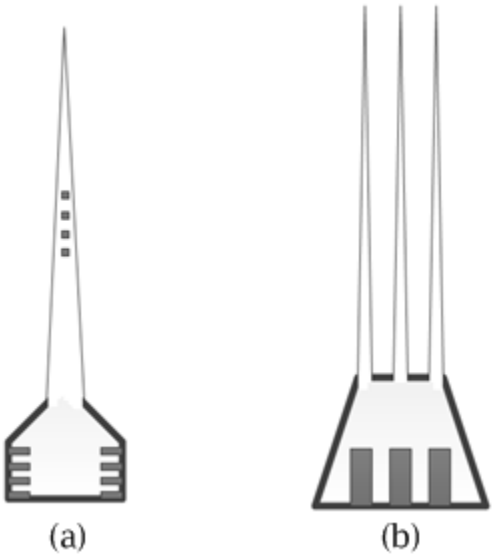

Figure 5.2. Microprobes made from microwires. (a) Single microprobe. (b) In-plane microprobes

Microneedle array fabricated on a flexible patch, as shown in Figure 5.1(a), was introduced in order to overcome the shortenings of the traditional rigid patch. It may be utilized in various applications, such as transdermal drug delivery, local cancer treatment, control-released treatment, brain implant, intracranial hemorrhage treatment, brain probing and stimulation, and etc. Flexible microneedle patches are more likely to remain implanted at a precise location compared to rigid patch [Huang 2007, Takeuchi 2004], and attain implantation with less damage [Stieglitz 1997, Takeuchi 2000, O'Brien 2002]. Due to these

advantages, flexible microneedle patch may be suitable for brain probing and stimulation more than the traditional microprobes.

However, there exist some difficulties relating to the device. Depending on the material property used in the fabrication, the patch may or may not accommodate perfect-fitting to the skin curvature. This may cause some microneedles unable to penetrate into the soft tissue. Also, since the patch is fabricated from a deformable material, it may be bent or twisted into undesirable shape especially on a certain area where skin curvature change abruptly. Moreover, microneedles attached on the patch may be damaged during the insertion process by different modes of failures such as buckling and bending due to angled insertion. To design effective flexible microneedle patch, these factors must be thoroughly analyzed and taken into account.

This chapter presents a modeling technique to be used in demonstrating the characteristics of the flexible microneedle patch when it is being fitted onto a free form surface. A three dimensional computer model of flexible microneedle patches is developed with a mass spring system. Once fitted onto a free form surface, the deformation of the patch is calculated based on the internal strain energy which represents the physical property of the fabricated material. With the developed performance measurement tool, the effectiveness of different microneedle patches can then be measured. Also, by varying the physical properties of the patches via the maximum allowable strain energy, their effects on the microneedle performance can be predicted and analyzed.

The organization of this Chapter is shown as the following. Section 5.2 indicates the problems in developing flexible microneedle patch. Section 5.3 presents a method to

determine the performance of microneedle. Section 5.4 presents the design configuration of microneedle array used in brain probing and stimulation. Section 5.5 introduces a method to model a flexible microneedle patch using mass spring system. Section 5.6 describes a skin modeling technique. Section 5.7 presents a surface fitting algorithm that fits the developed flexible patch model onto a 3D surface. Summary is presented in Section 5.8.

5.2 Problem in developing flexible microneedle patch

Buckling and bending are the typical failure modes that may damage microneedles during the insertion process [Aggarwal 2004]. In typical needle insertion experiments, it is always assumed that the needle is oriented in the same direction as the inserting direction which is perpendicular to the skin surface. As a result, only buckling failure is considered. However, in the insertion of flexible microneedle patch, this may not always true. Since it is almost impossible to maintain needle's vertical orientation due to the curvature of the skin, each microneedle may encounter external forces of different magnitude and directions.

We divide the possible cases of microneedle insertion into skin into two cases; 1) the needle is inserted perpendicularly to the skin, and 2) the insertion occurs at an angle. These different insertion modes are illustrated in Figure 5.3. In the Figure, d is the insertion depth in the direction of the needle displacement, M is the moment caused by the lateral force component, θ is the angle between surface normal of the skin and axial direction of microneedle.

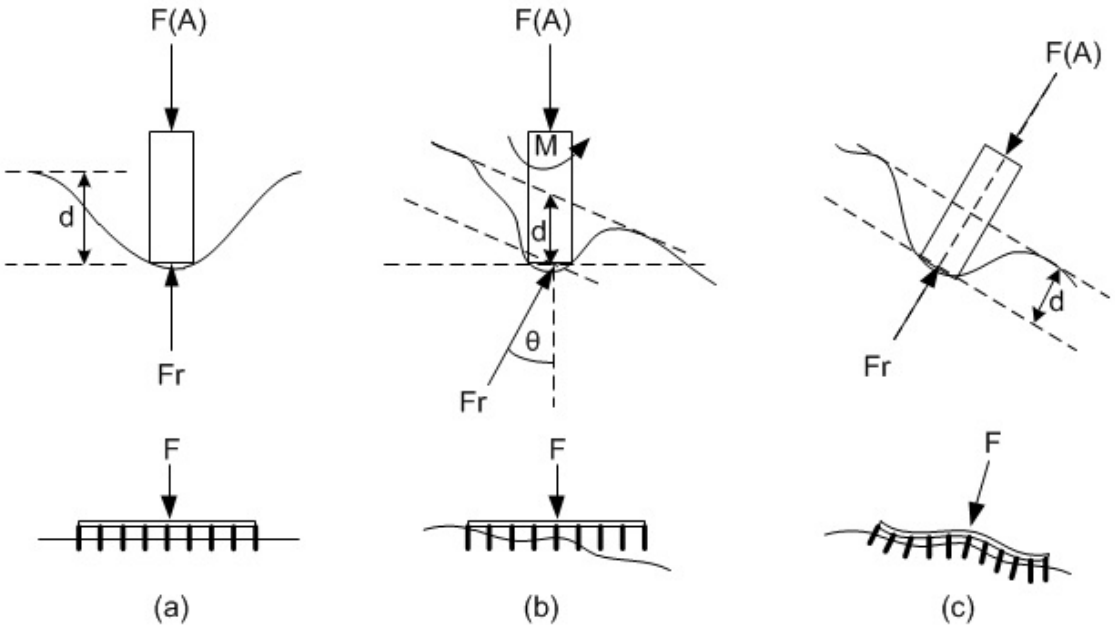

Figure 5.3. Force diagram of microneedles when it is in contact with the skin. (a) Axial force in rigid patch. (b) Angled force in rigid patch. (c) Axial force in flexible patch.

It is postulated that the input force is always in vertical direction and points downward (-Z). The first case (Figure 5.3(a)) demonstrates the ideal posture of microneedle insertion into skin. The insertion direction is perfectly perpendicular to the skin surface. As a result, the major type of failure in this situation is buckling. The second case (Figure 5.3(b)), on the other hand, shows a more realistic situation where the angle of insertion (θ) is not zero. In this case, both buckling and bending may be experienced due to axial force and the force normal to the surface of the skin. Figure 5.3(c) shows the ideal posture of flexible microneedle patch where the insertion direction of each microneedle is perpendicular to the skin surface. The forces obtained from these circumstances may be calculated by the following.

Assuming that the insertion force reaches the peak at the moment of puncture, the relationship between tip size (represented by tip's area *A*) and the insertion force at puncture (*F(A)*)can be expressed by the following equation [Davis 2004].

$$F(A) = 0.00019A - 0.66 \tag{5.1}$$

In the first case (Figure 5.3(a) and Figure 5.3(c)), the microneedle's body is aligned perpendicular to the contact surface of the skin. Needle displacement is in vertical direction and in similar direction of the axial line. Therefore, the reactive force (F_r) that may cause buckling can be simply formulated using the predictive function of the force in vertical direction. The resulting reactive force becomes:

$$F_{Bu} = F_r = F(A) \tag{5.2}$$

In the second case (Figure 5.3(b)), the microneedle does not lie perpendicular to the surface. The input force is, however, passed through the axial line of the needle. The reactive force in the normal direction to the skin may create bending while the reactive force in the axial direction of the needle contributes to buckling. The reactive force (F_r) in the normal direction to the surface may be computed by:

$$F_r = \frac{F(A)}{cos\theta} \tag{5.3}$$

Thus, the force contributes to bending is;

$$F_{Be} = F(A) \cdot tan\theta \tag{5.4}$$

The force component that is in the axial direction of the microneedle is the major part that causes buckling, while the force component that is in lateral direction contribute greatly to bending failure. As microneedles are usually made in the array format, each microneedle may contact with the skin at different angles and result in different degrees of the two failure modes. A microneedle that is able to withstand buckling may suffer from bending if such encounter is inevitable. In our case, any microneedle that has either one of the two failure modes is considered as ineffective. To determine whether a microneedle has any failure, we compute the forces obtained from Equations (5.2) and (5.4), and compare them with the critical buckling and bending load which can be computed using Equations (5.5) – (5.8). The critical buckling load that a uniform body can withstand can be written as:

$$P_{Bu} = \frac{C\pi^2 EI}{L^2} \tag{5.5}$$

Where P_{Bu} is the critical buckling load, c is a constant related to fixed-end condition (C = 0.25 for the case of one end fixed, another end free), *E* is the Young's modulus of the material, *I* is the moment of inertia, and *L* is the length of the microneedle. And the critical buckling load that a uniform varying cross section body can withstand is formulated by:

$$P_{Bu} = \frac{mEI_2}{L^2} \tag{5.6}$$

where I_1 and I_2 are the moment of inertia at the tip and base of microneedle respectively, and m is a constant related to the rational between I_1 and I_2 [Timoshenko 1961]. The critical bending load for a uniform body is as shown by the following.

$$P_{Be} = \frac{\sigma\pi D_1^3}{32L} \tag{5.7}$$

While the critical bending load of a uniform varying cross section is determined by:

$$P_{Be} = \frac{27\sigma(t-1)\pi D_1^3}{128L} \tag{5.8}$$

where P_{Be} is the critical bending load, σ is the maximum allowable stress, t is the ratio between D_2 and D_1 i.e. $t = D_2/D_1$, D_1 is the tip diameter of the microneedle, D_2 is the diameter at the base of microneedle, and L is the length of the microneedle.

When a microneedle becomes ineffective due to the failures described earlier, its performance drops to zero. However, if the microneedle is not rendered ineffective, its performance must be rated and quantified. In order to measure the performance of the whole microneedle patch, the performance of each microneedle must be analyzed and determined. In this paper, we used a parameter called Microneedle Performance Index (MPI) to measure how well the flexible microneedle patch performs [Boonma 2012c]. In the next section, we

will briefly explain how to compute MPI and use it to measure the performance of the whole microneedle patch.

5.3 Computation of Microneedle Performance Index (MPI)

We use a parameter called the Microneedle Performance Index (MPI) to quantify the effectiveness of flexible microneedle patch. The parameter is developed based on the skin permeability. Skin permeability is basically a parameter used to determine the transdermal diffusion of drugs into skin. It represents the path length of a solute across a skin thickness over a period of time. As MPI increases, the skin permeability will increase accordingly. High MPI is more preferable as it means the body can take in large amount of drugs. MPI can be computed using the relationship between ability to withstand buckling and bending, fractional skin area, and the length of holes corresponding to the soft tissue thickness. The equation used to calculate MPI can be formulated as the following

$$MPI = \frac{\varphi \omega Q}{P_{xy}^2 H} = \frac{\varphi \omega n^2 Q}{w^2 H} \tag{5.9}$$

where φ is a constant indicating the resistance of microneedle against buckling, ω is a constant indicating the resistance of microneedle against bending, n is number of microneedle on the patch, w is the width of the patch, H is the skin thickness or distance to the level of perfect permeation measured from the skin surface, and Q is a parameter related to the geometry of microneedles. φ and ω could have the value of either 0 (if microneedle

buckles or bends) or 1 (if microneedle can withstand those failures). It should be noted that Equation (5.9) is slightly different from our previous work [Boonma 2012b] as we consider one more type of failure (bending) in this study.

In order to calculating Q, the depth that microneedle can make in the insertion process must be determined. The insertion depth of a microneedle can be determined by tip size, length of the microneedle, and the resistance of soft tissue. Previous studies have shown that the punctuation into soft tissue can be described by energy method. Assuming that the energy required for initiating a crack in the skin equal to the work created by microneedle displacement, the relationship between insertion force required for puncture and needle displacement can be formulated as shown by follows [Davis 2004]:

$$F(d) = \alpha e^{\tau d} \tag{5.10}$$

where α is the pre-exponential constant, τ is the exponential constant and d is the displacement of microneedle in inserting direction. According to the energy equation, the force obtained from Equation (5.10) is the force required to puncture into skin and the microneedle displacement (d) is equivalent to the amount of skin deformation before the crack appears.

At puncture point, the force created by soft tissue deformation is equal to the force required for penetration. Therefore, the amount of insertion depth that a microneedle must travel before successful puncture into the skin can be determined. This can be done by setting

Equation (5.1) equal to (5.10) and rearranging the terms to obtain the insertion depth before puncture (d), which appears to be:

$$d = \left(\frac{1}{\tau}\right) \ln\left(\frac{0.00019A - 0.66}{\alpha}\right) \tag{5.11}$$

For Equation (5.11) to be valid, the value of the logarithmic term must be larger than 1. This implies that the minimum tip diameter that we can use to predict the insertion depth using Equation (5.11) is limited to 67.4 μm. The insertion depth of a microneedle with smaller tip diameter may be estimated by linear approximation. Based on Equation (5.11), a microneedle is considered as effective when the position of microneedle's tip is buried beneath the skin by at least the amount of needle insertion before puncture (d). This is shown in Figure 5.4. Let a distance that a microneedle travels in relative to the skin surface be defined as:

$$x_{i,j} = \left\| Ntip_{i,j} - Nint_{i,j} \right\| \tag{5.12}$$

Where $Ntip_{i,j}$ is tip point of microneedle, and $Nint_{i,j}$ is the intersection point between microneedle and the 3D surface. Skin permeability generated by a microneedle can be calculated only if $x_{i,j}$ computed from Equation (5.12) is larger than d computed from Equation (5.11).

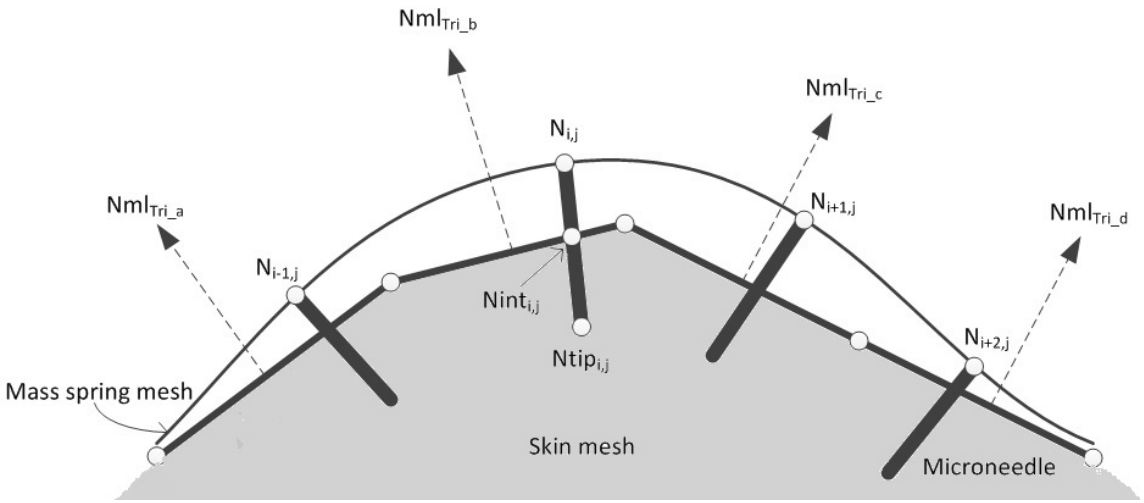

Figure 5.4. Insertion of microneedles into soft tissue.

The performance of flexible microneedle patch is only computed after the patch is applied onto the skin surface. Before we describe the development of microneedle and skin models, design parameters of microneedles and the soft substrate must be determined.

5.4 Design parameters of flexible microneedle patch in brain probing and stimulation

In our attempt to create a computer model of flexible microneedle patch for brain probing and stimulation, geometric parameters of the patch must be determined. The design parameters of the flexible microneedle patch consists of needle geometry, dimension of the patch, and spacing between any pair of microneedles. In the past, single electrodes have uniform thickness except at the tip where they are sharpened. The thicker shank facilitates the handling while the thinner tip supports the ease of insertion [Najafi 1994, Cheung 2000,

Sugai 1999]. These geometries have been used mainly to minimize damage to the brain and achieve easy insertion and handling.

In term of the distance between microneedles, it was reported that the diameter of efferent pathways were between 200 μm and 1.0 mm [Asanuma 1975, Murray 1981]. The efferent pathways are the nerve structures through which an electric signal travels. A separation spacing was found to be ranging from 500 μm to 1.0 mm [Jones 1977]. The size of a region where all insertions generate a similar motor activity was defined to be between 500 μm to 2.0 mm [Kwan 1978]. From these values, the proper electrode spacing should be in the order of 500 μm [Maynard 1997].

In this study we create microneedles into cylinder and cone since they have been used in fabrication of microneedle patch. Based on the previous studies that we have described earlier, we believe that the appropriated design for microneedle for brain probing and stimulation should be at least 1 mm long and each microneedle should be about 0.5 – 1 mm apart. Once the geometric parameters of microneedle patch are obtained, a computer model is used to represent the flexible microneedle patch. A three dimensional model of soft tissue is developed as well since it is required in measuring the characteristics and performance of the microneedle patch. In the next section, the development of a computer model representing a flexible microneedle patch is presented.

The length of microneedles is designed according to the function of the device. In general, brain probing applications are composed of cortical and deep brain probing. In cortical probing, the length of cortical electrodes needs to be about 1 – 1.2 mm while in the deep brain probing the parameter must be at least 10 mm (10 times longer) to reach

subthalamic nucleus (in rats) [Motta 2005]. The width of the arrays is usually ranging between 1.5 – 4.2 mm [Rousche 1998, Maynard 1997]. Moreover, as the microprobes need to be inserted into the brain, the proper insertion depth of these microprobes was approximately 1 mm.

5.5 Modeling of flexible microneedle patch

We postulate that the characteristics of flexible microneedle patch are more fabric-liked, similar to traditional dermal patch. Generally, a fabric is made of yarns that are arranged in a certain orientation such as vertical and horizontal as shown in Figure 5.5(a). The way that these yarns are organized is rather similar to the mass spring structure. Thus, we decided to model the flexible microneedle patch using a mass spring model (Figure 5.5(b)) although some other existing modeling techniques such as finite element method (FEM) and mass tensor model (MTM) may be used in the same task. Moreover, mass spring model could be a good start as it allows more control over the mass nodes, and fast computation.

In theory, mass spring model (MSM) represents an object by a set of mass points [Bielser 2000, Mohr 2003, Mollemans 2003]. Each point, called mass node, is connected to one another by springs. Stiffness of each spring can be specified individually by spring constants. Since dermal patch can be deformed in any direction, a mass spring model is developed such that it is able to demonstrate this behavior. Throughout the paper, we will call the model as “Flexi-patch”. The Flexi-patch model can be described as follows. Assume that we have a local coordinate system with only two dimensions (e.g. U-axis and V-axis) set

on the microneedle patch, a 2D mass spring mesh *M* representing the patch consists of mass nodes $N_{i,j}$ where $0 < i \leq n_h$, $0 < j \leq n_v$, n_h and n_v are number of mass nodes in horizontal (U-axis) and vertical direction (V-axis) respectively, where U and V-axis are two dimensions coordinate system on the microneedle patch. Each mass node is connected to adjacent mass nodes called neighbors by springs. Each spring can be assigned different properties by setting the spring constant. If set properly, the mass spring model can demonstrate either isotropic or anisotropic response. For example, to simulate the ability to extend in every direction, the spring constant in horizontal, vertical and diagonal spring are set to the same value.

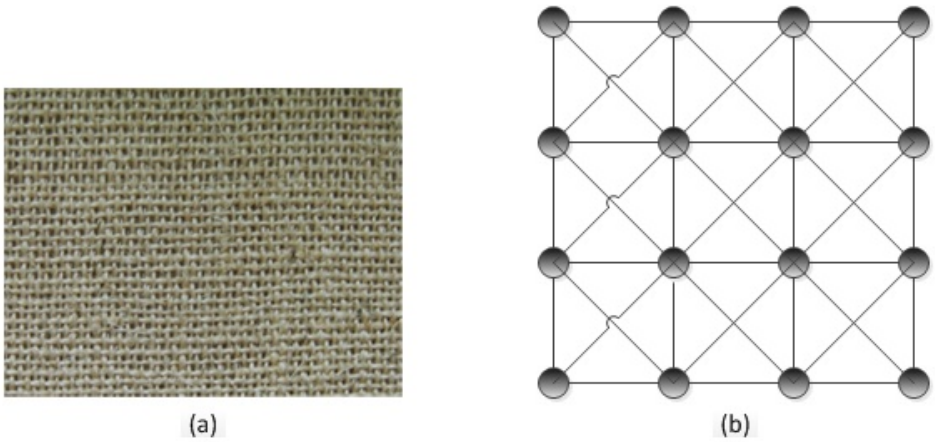

Figure 5.5. (a) An example of fabric made of vertical and horizontal yarns. (b) Mass spring structure.

To define the neighbors, for any mass node $N_{i,j}$, mass nodes $N_{i\pm1,j\pm1}$ are considered as neighbor nodes to $N_{i,j}$. Similar to triangles, there are two types of mass nodes, including inner and outer nodes. A mass node whose number of neighbors is less than eight is outer mass node. The inner mass node on the contrary must have exactly eight neighbors. Figure

5.6 shows mass spring structure of Flexi-patch while Figure 5.7 shows data structure of the Flexi-patch model. It is assumed that a microneedle with a specific length is attached to each mass node and its tip points to the opposite direction of normal vector of the node. All microneedles on the entire patch are of the same length.

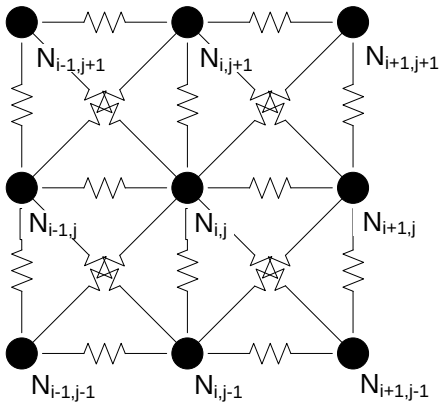

Figure 5.6. Mass spring structure of Flexi-patch. Node $N_{i,j}$ is an inner node while node $N_{i+1,j}$ is an outer node.

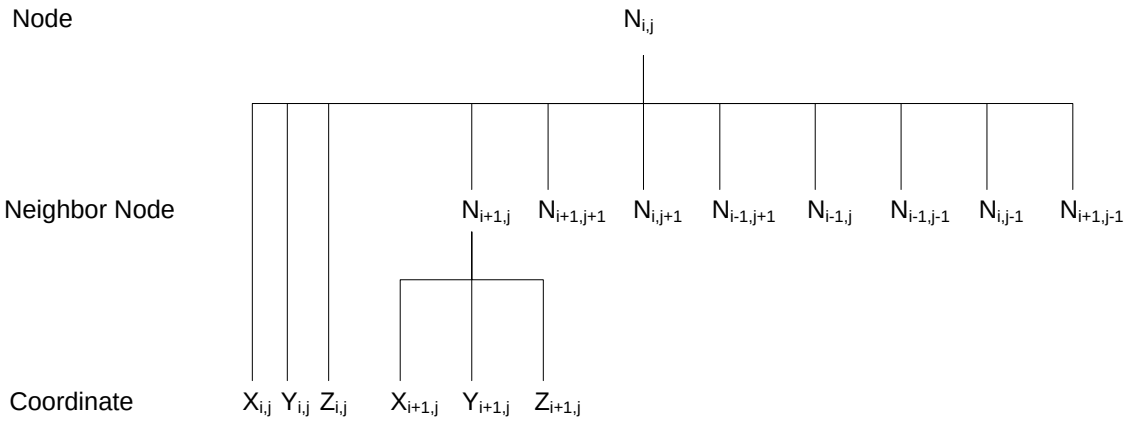

Figure 5.7. Data structure of Flexi-patch model.

The development of a skin model is less complex compared to the microneedle patch as it does not require mass spring structure. However, the linkages between each element in the surface model are still required to facilitate the mapping process. As the skin model consists of a large number of elements (e.g. triangles), setting up such connection usually take certain computation time. We will describe the skin model and its structure next.

5.6 Development of triangulated skin model

The surface representation of the skin model used in this study is demonstrated by a set of points and triangles called triangular mesh. These triangles are connected seamlessly (watertight), thus there is no hole or island in the model. An example of a watertight triangular surface is shown in Figure 5.8. Each triangle has three vertices and three edges. A vertex contains a XYZ coordinate or location in 3D space, while an edge is formed by two vertices of the same triangle. When an edge of a triangle is a reverse representation of another edge of a different triangle, the triangle has a neighbor. A triangle could have up to three neighbor triangles.

To facilitate the subsequent processes, we classified the triangles into two categories, inner and outer triangles based on the number of neighbor triangles of individual triangle. Inner triangles are triangles whose all three edges are connected to other triangles. We call an adjacent triangle to triangle T_i as a neighbor triangle to triangle T_i. Outer triangles, on the contrary, are those whose number of neighbor triangles is less than three.

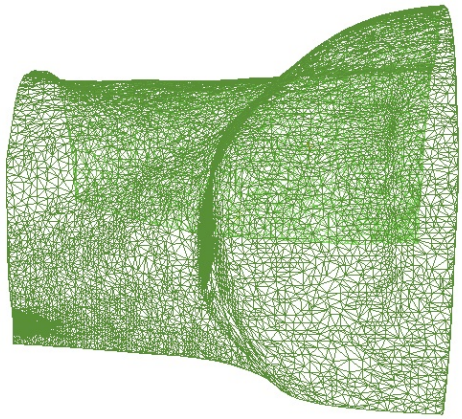

Figure 5.8. A skin model represented by a watertight triangular mesh.

Figure 5.9 shows the data structure of the skin model used in this study. When the model is being read, vertices in a triangle are ordered in the counter clockwise format. This causes the surface normal N_i of triangle T_i to always point outward. Once the skin model is ready, a searching algorithm is initiated in order to gaining neighboring information. Each triangle is linked to its neighbors by pointers. These setups are crucial as they can significantly reduce run-time in later stages.

Once both Flexi-patch and skin models are created, the process of applying microneedle patch onto the skin surface may begin. Since the patch model is considered soft and deformable, it may be stretched or shrunk when applied on the skin depending on the allowable strain energy and the skin surface. The following surface fitting technique may be used to approximate the topology and characteristics of the flexible microneedle patch during the applying process.

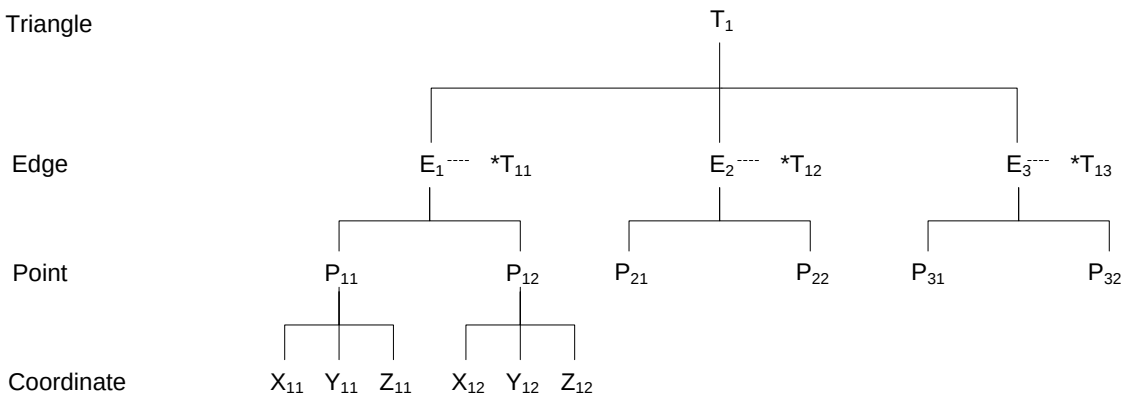

Figure 5.9. Data structure of the skin model used in this study.

5.7 Surface fitting algorithm for flexible microneedle patch

Fitting microneedle patch onto skin surface is similar to the problem of 3D surface fitting. It is also a reverse process of surface flattening where a 3D object is mapped onto a 2D plane. Mass spring model has been used in surface flattening [Fan 1998], along with energy minimization [McCartney 1999]. At the beginning of the process, 3D object must be converted into a mass spring system and then mapped onto a 2D plane based on mass spring properties [Wang 2002]. The fitting of 2D woven-like mesh onto 3D surface based on discrete geodesic distance was introduced before [Wang 2005]. These methods did not map the mass node according to the way the dermal patch is applied to the skin. Thus, the final orientation of the mesh may not replicate the actual orientation of dermal patch. Moreover, the techniques tend to restrict the stretchability of the mesh and thus do not reflect the actual property of dermal patch.

Our method consider a physical habit of applying a dermal patch to the skin, where one corner of the patch is positioned first, then the rest of the patch is gradually swept onto

the skin by hand. Assuming that the insertion direction is in –Z direction, the surface fitting process begins by projecting the first mass node ($N_{0,0}$) onto the surface. This node could be one of the nodes on the four corners of the patch (assuming that the patch has a square shape). Typically, we choose the node that has minimum X and Y coordinates (the bottom left corner of the patch) to be the first mapping node.

We then set the node $N_{0,0}$ as an active node *AN*. Next, in a sweeping fashion, the neighbor nodes of the first node $N_{0,0}$ such as $N_{1,0}$, $N_{1,1}$, and $N_{0,1}$ are fitted onto the surface. After all neighbors have been set, node $N_{0,0}$ is not an active node anymore. Instead, we set one of the recently mapped node e.g. $N_{1,0}$ to be the next active node *AN*. This process is repeated until all mass nodes are mapped onto the surface. We call this technique the Flexible Patch Fitting algorithm. The flow chart of this algorithm is shown in Figure 10 and its pseudo code is shown in Algorithm 1. Also, the way we search for and map the next point onto the surface is called node sweeping technique. Its concept is similar to region growing where neighbors are considered first and the search gradually progresses outward. Figure 5.11 illustrates the node sweeping method where neighbor nodes of the mapped nodes are subsequently fitted onto the surface until all mass nodes on the patch are considered.

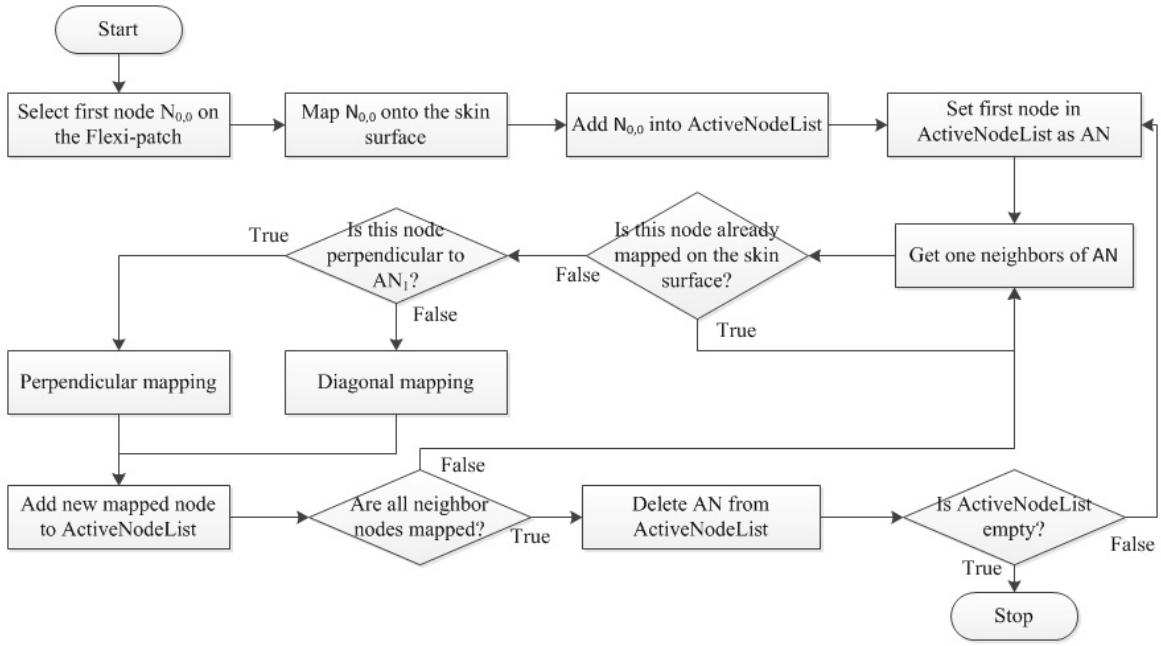

Figure 5.10. Flow chart of the Flexible Patch Fitting algorithm

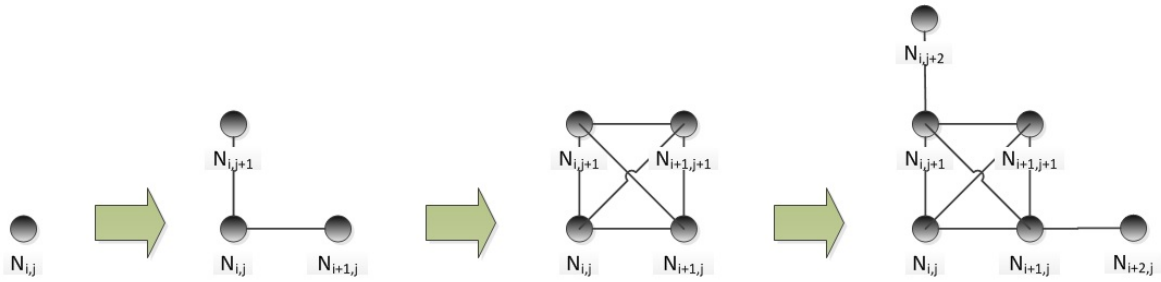

Figure 5.11. Progression of Flexible Patch Fitting by node sweeping method. From node $N_{i,j}$, map neighbor nodes $N_{i,j+1}$ and $N_{i+1,j}$ by perpendicular mapping. Then, map neighbor node $N_{i+1,j+1}$ by diagonal mapping. The process continues until all nodes in Flexi-patch are fitted onto the skin surface.

Algorithm 5.1: **Flexible Patch Fitting (*M*)**
Input: List of mass nodes *M* which contains original positions of mass nodes
Output: List of mass nodes *M* which contains original positions and mapped positions of all mass nodes.

FIND the first mapping node
COMPUTE projection of the first mapping node on the surface
ADD the mapped node into container ActiveNodeList
WHILE ActiveNodeList is not empty
    SET the first node in ActiveNodeList as active node
    FOR each neighbor node of the current active node
        IF the node is not mapped yet AND the node is perpendicular to the current active node
        DO perpendicular mapping
        ADD this mapped node in the back of ActiveNodeList
    END IF
    IF the node is not mapped yet AND the node is not perpendicular to the current active node
        DO diagonal mapping
        ADD this mapped node in the back of ActiveNodeList
    END IF
    END FOR
    DELETE current active node from ActiveNodeList
END WHILE

The flexible patch fitting algorithm needs subroutines such as perpendicular mapping and diagonal mapping. Detail of these subroutines can be described by the following sections.

5.7.1 Perpendicular mapping for fitting axial mass nodes

Perpendicular mapping is used to fit new mass nodes that are in the vertical and horizontal direction from the current active node (such as mapping of nodes $N_{i,j+1}$ and $N_{i+1,j}$ from node $N_{i,j}$ shown in Figure 5.11). In this subroutine, three input nodes are required, 1) the first mapped node, 2) the current active node $N_{i,j}$, and 3) the mapping node e.g. $N_{i,j+1}$. First,

we calculate the moving direction $\vec{d}$ from the original position of $N_{i,j}$ and $N_{i,j+1}$. Second, we find a cutting plane that $\vec{d}$ is on. Then, the original distance between $N_{i,j}$ and $N_{i,j+1}$ is computed. Finally, we calculate the final position of $N_{i,j+1}$ by traveling on the surface with the original distance. This can be computed by another subroutine called geodesic traverse. Now, if $N_{i,j+1}$ is not directly perpendicular to the first mapped node (e.g. it is not on the boundary of the patch), it is possible that this node can be stretched or shrunk. Thus, the energy minimization subroutine is called and used to compute the mapped located of a node based on the maximum allowable strain energy. The process of perpendicular mapping can be described by the following algorithm, while its flow chart is shown in Figure 5.12.

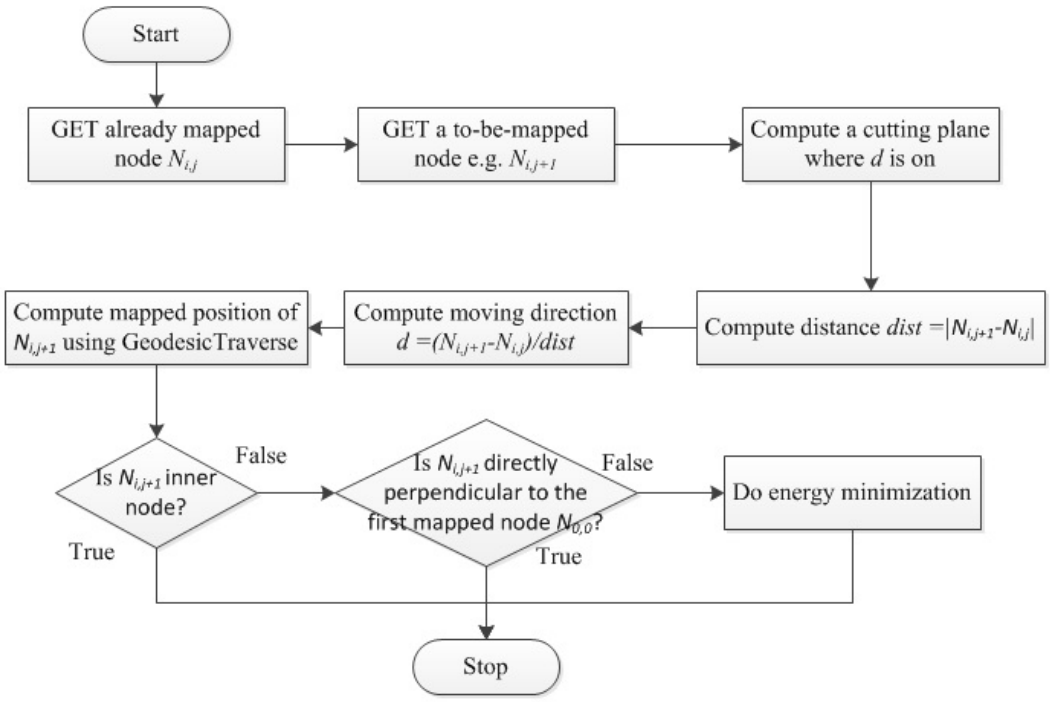

Figure 5.12. Flow chart of Perpendicular Mapping algorithm

Algorithm 5.2: **Perpendicular Mapping**
Input: First mapped node $N_{0,0}$, current active node $N_{i,j}$ and the mapping node $N_{i,j+1}$.
Output: Final position of the mapping node $N_{i,j+1}$.

COMPUTE original distance *dist* between $N_{i,j}$ and $N_{i,j+1}$.
COMPUTE moving direction $\vec{d}$ from original position of $N_{i,j}$ to $N_{i,j+1}$.
COMPUTE a cutting plane which vector $\vec{d}$ is on.
COMPUTE the final position of node $N_{i,j+1}$ by using subroutine Geodesic traverse (traveling from $N_{i,j}$ with the distance *dist* on the skin surface and in the direction $\vec{d}$).
IF node $N_{i,j+1}$ is an inner node and not in perpendicular to the first mapped node $N_{0,0}$
    DO energy minimization
END IF

The perpendicular mapping is used to handle nodes that are either in vertical or horizontal of the current active node. For nodes that are in other directions e.g. diagonal direction, the diagonal mapping is required. We will now describe the process of diagonal mapping.

5.7.2 Diagonal mapping for fitting non-axial mass nodes

Diagonal mapping is applied to mass nodes other than those handled by perpendicular mapping. As an example, for an active node $N_{i,j}$, node $N_{i+1,j+1}$ is handled by diagonal mapping (Figure 5.11), while nodes $N_{i+1,j}$, and $N_{i,j+1}$ are handled by perpendicular mapping. Diagonal mapping is performed almost similar to the perpendicular mapping. Except that all nodes processed by the technique must be placed under energy minimization subroutine to determine how much the nodes are allowed to stretch or shrink.

The subroutine Geodesic traverse is used to calculate the final position of a node when traveling on the free form surface by a specific distance. Its procedure will be described next.

5.7.3 Geodesic traverse for surface fitting

The term “geodesic” roots from the shortest path between two locations on the earth’s surface. In our case, the geodesic distance is a distance on the free form surface. As introduced in the work of [Wang 2005], geodesic distance can be used in surface fitting technique and provides good result. We employ the concept of the geodesic path and instead of computing intersection between all triangle edges and the cutting plane, we conduct the intersection test only for those triangles that are adjacent to the active triangle. Active triangle is the triangle that the active point is on. This way, run-time of the algorithm can be improved by sacrificing initial setup of data structure.

Figure 5.13 shows the ideal case where the original length of a spring remains constant even after the spring is mapped onto a free form surface. However, in actual case, this will be difficult to achieve since the length of spring tends to change after the fitting process. Therefore, the geodesic traverse algorithm is developed to monitor9 the difference between the original distance ($|d|$) and the current distance between the active node and the mapping node ($|d_1|+|d_2|+|d_3|$). If the current distance is smaller, the mapping node is moved away by the difference. However, if the current distance is larger, the mapping node is moved closer by the difference amount. The algorithm stops when the difference is less than a threshold value. The process of geodesic traverse algorithm is described as follows.

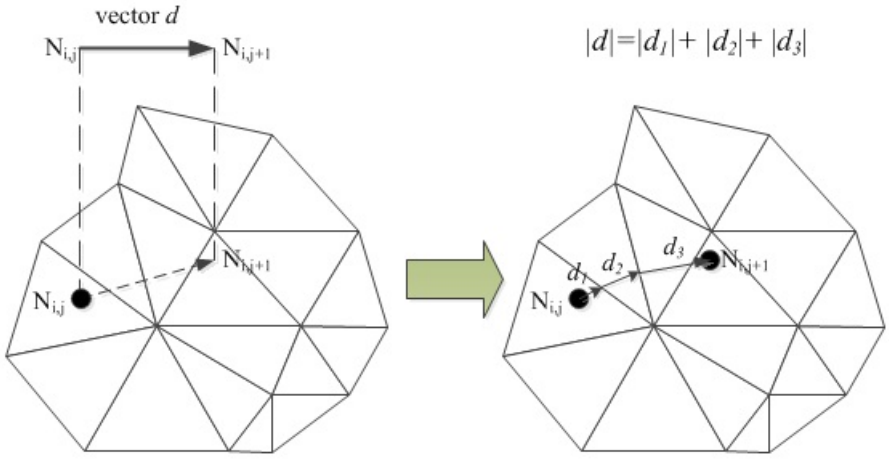

Figure 5.13. Geodesic distance of $|\vec{d}|$ in the direction $\vec{d}$ over a free form surface.

Algorithm 5.3: **Geodesic traverse**

Input: Moving direction $\vec{d}$, active node N_i (node that is already mapped), and mapping node $N_{i+1,j+1}$ (next node to be mapped)

Output: Mapped position of node $N_{i+1,j+1}$

COMPUTE cutting plane that the moving direction vector $\vec{d}$ is on
COMPUTE distance vector $dist_0$ between original position of active node N_i, and original position of mapping node $N_{i+1,j+1}$
COMPUTE moving step e.g. $S = 0.25*dist_0$
COMPUTE mapped position of $N_{i+1,j+1}$ by adding S to the mapped position of the active node N_i
COMPUTE the current distance *dist* between the mapped position of the active node N_i and the mapped position of $N_{i+1,j+1}$
FIND triangle T_i that the active point is on
WHILE $dist < dist_0$
    SET active triangle to T_i
    FOR each edge of T_i
        IF the cutting plane intersect this edge
            COMPUTE the distance $dist_t$ between the intersection point P_{int} and the mapped active node
            IF $dist+dist_t < dist_0$ // mapped position is not on this active triangle
                SET mapped position of mapping node $N_{i+1,j+1}$ to the intersection point P_{int}
                SET active triangle to the neighbor triangle at this edge
                SET $dist = dist+dist_t$

BREAK
ELSE // mapped position is on this active triangle
COMPUTE the mapped position of mapping node $N_{i+1,j+1}$ e.g.
$P_{int} + (dist_0\text{-}dist)\ \vec{d}$
SET $dist = dist_0$
BREAK
END IF
END IF
END FOR
END WHILE

The geodesic traverse algorithm calculates the mapped position of the mapping (or to-be-mapped) node on the surface based on geodesic distance from the already mapped node to the mapping node. However, the position of newly mapped node may not always correct as it is dependent on the allowable stretch or shrinkage of the spring that links two nodes together. To define the maximum deformation of the spring, energy minimization technique is employed.

5.7.4 Energy minimization for surface fitting

It is postulated that the flexible microneedle patch retain minimum energy when it is exactly on a 2D plane. In other words, the patch contains zero energy when it is still flat. Once fitted onto a 3D surface, the strain energy generated inside the patch grows larger. Since the microneedle patch is represented by a mass spring system, the computation of total strain energy in the system is rather similarly to spring energy calculation, which is similar to the expression in Equation (5.13):

$$E_{i,j} = (0.5) \sum_{N_{k,l} \in P(N_{i,j})} K_{(i,j)(k,l)} (\Delta L_{(i,j)(k,l)})^2 \quad (5.13)$$

where $E_{i,j}$ is strain energy at node $N_{i,j}$, $K_{(i,j)(k,l)}$ is spring constant between $N_{i,j}$ and $N_{k,l}$, $\Delta L_{(i,j)(k,l)}$ is the difference between initial and current length of the spring that links $N_{i,j}$ to $N_{k,l}$ and can be computed by Equation (5.14).

$$\Delta L_{(i,j)(k,l)} = \left\| L^{t}_{(i,j)(k,l)} - L^{t=0}_{(i,j)(k.l)} \right\| \quad (5.14)$$

During the fitting process, the strain energy in newly created spring (created by locating new mass node) is always computed and compared with the maximum allowable threshold. If the calculated energy exceeds the threshold, a fractional energy is computed and used to determine the appropriated location of the new mass node. In this fashion, large allowable energy simply means that the flexible microneedle patch is easily stretchable and conformable to the surface. However, if this energy is small, the patch becomes more rigid and tends to resist the deformation. This can be demonstrated by an example.

Considering Figure 5.4, Let $E_{i,j}$ be the spring energy required to move node $N_{i,j}$ to $Nint_{i,j}$ with the distance $\overline{N_{\iota,J} N\imath nt_{\iota,J}}$, and E_{cri} be the maximum allowable strain energy in spring. The fitted location of $N_{i,j}$ represented by $N'_{i,j}$ can be determined by Equation (5.15). From this equation, it can be implied that the more flexible the patch is, the higher the value of maximum allowable strain energy would be.

$$N'_{i,j} = \begin{cases} Nint_{i,j} & , \quad if\ E_{i,j} < E_{cri} \\ N_{i,j} + \left(\dfrac{E_{cri}}{E_{i,j} - E_{cri}}\right)\overline{N_{\iota,J}Nint_{\iota,J}} & , \quad if\ E_{i,j} \geq E_{cri} \end{cases} \tag{5.15}$$

However, this may cause changes in other springs connected to $N_{i,j}$. Therefore, the energies in those springs must be monitored. If they exceed the allowable threshold, slight adjustment of $N_{i,j}$ can be done until $N_{i,j}$ reaches $N'_{i,j}$ or the energies are at the threshold. The flow chart of energy minimization method is shown in Figure 5.14.

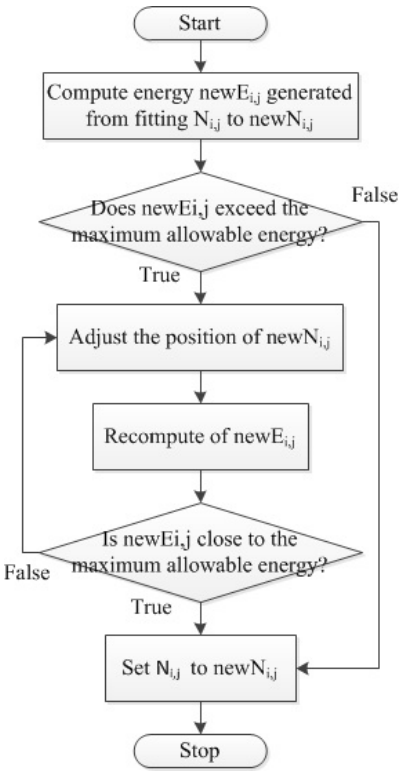

Figure 5.14. Flow chart of energy minimization method.

Up to this point, we have described how to create microneedle patch and skin model, and the related methods that may be used to fit the 2D microneedle patch onto a 3D free form surface of the skin based on applying procedure of dermal patch, geodesic distance, and energy minimization.

5.8 Summary

This chapter presents an energy-based surface fitting algorithm that can be used to fit a flexible microneedle patch onto a skin surface and analyze the effectiveness of the patch through a measurement tool called Microneedle Measurement Index (MPI). A mass spring model is used to represent the flexible microneedle patch. Fitting of the Flexi-patch model onto a skin surface is based on geodesic distance and internal strain energy minimization. The presented technique can be used in the design and analysis of flexible microneedle patch or other medical devices of similar nature.

CHAPTER 6

EXAMPLES AND RESULTS

This chapter presents some examples and results of the proposed techniques that we have introduced previously. In the previous chapters, the methodology of microneedle and soft tissue interaction modeling during the pre-puncture and post-puncture has been presented along with an analytical modeling for microneedle design evaluation and free form surface fitting techniques. The development of these tools may open a new opportunity for medical research communities to gain more knowledge in the area of microneedle technology and create new invention for diagnosis and treatment of diseases that may be difficult to cure with conventional medical devices.

6.1 System implementation

The proposed methods have been implemented at North Carolina State University on and Intel® CORE™ i3 CPU personal computer, loaded with Intel® HD graphics, 4GB of RAM, and Microsoft Windows 7 64 bit. Microsoft Visual Studio 2010, OpenGL®, and Matlab R2009a are used for program development and implementation.

6.2 Examples of pre-puncture, post-puncture force modeling and validation

The proposed two-stage modeling technique was implemented using Matlab R2009a. An example soft tissue model was first built as solid sample filled with monotonous material e.g. silicone rubber for validation purpose. Properties of the rubber are represented by

Young's modulus and Poisson ratio of 0.2 MPa and 0.48 – 0.49 respectively. The soft tissue model was later extended to assume heterogeneous properties of soft tissue consisting of three layers: Stratum Corneum, Epidermis, and Dermis. Their Young's moduli were set to 1 GPa, 0.134 MPa, and 0.08 MPa respectively. All tissue layers had the Poisson ratio of 0.4. The soft tissue model with the dimension of 3000 x 3000 x 1150 µm was first build as a solid object using SolidWorks and later converted to tetrahedral mesh model using Gmsh.

Three different solid microneedles were built using almost similar method. However, they are only represented by triangular mesh. The microneedles assumed the shape of cylinder, cone, and bevel. All microneedles had base diameter and length of 230 and 1000 µm respectively. Figure 6.1(a) and 6.1(b) show the example of heterogeneous soft tissue model and the microneedle geometries used in this study.

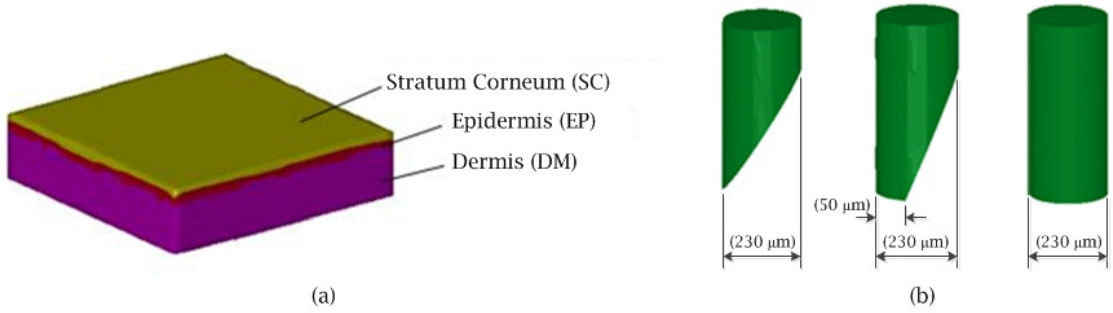

Figure 6.1. (a) Heterogeneous soft tissue. (b) Microneedles assuming different geometries

During the simulation, microneedle was originally held at a rest position and then slowly moved toward the soft tissue. Once the tip of microneedle touched the surface of soft tissue, it began to deform the surface and built up internal stress inside the soft tissue. This

stress is concentrated around the insertion spot and gradually fade away do to nonlinearity of soft tissue. Figure 6.2 shows an example of soft tissue deformation and stress concentration around the insertion point when a microneedle was inserted at the depth of 200 μm. Figure 6.2(a) shows stress concentration of sharp bevel microneedle while Figure 6.2(b) displays the stress caused by blunt bevel microneedle. Stress concentrated at smaller area as in the case of sharp bevel microneedle provides successful puncture at shorter insertion depth. This is confirmed by experimental data shown later in this section.

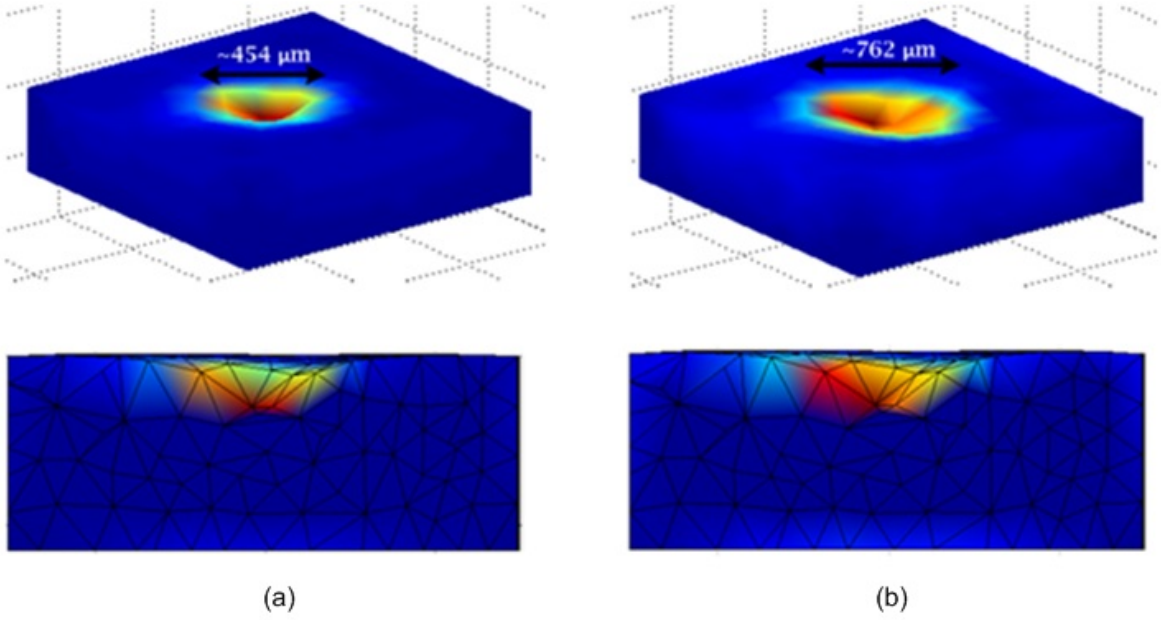

Figure 6.2. Stress built up near the insertion spot inside soft tissue (a) by sharp bevel microneedle; (b) by blunt bevel microneedle.

Figure 6.3 shows the stress concentration map on the soft tissue model after a patch of four microneedles were inserted on the example soft tissue. Each microneedle was positioned at each corner of the tissue and about 1600 μm apart from each other. All microneedles were

moved until they reached the insertion depth of 200 μm. High stress was detected around the area of insert and near the boundary of the tissue model. This is due to the preset boundary condition that no tissue nodes on the boundary faces are moveable.

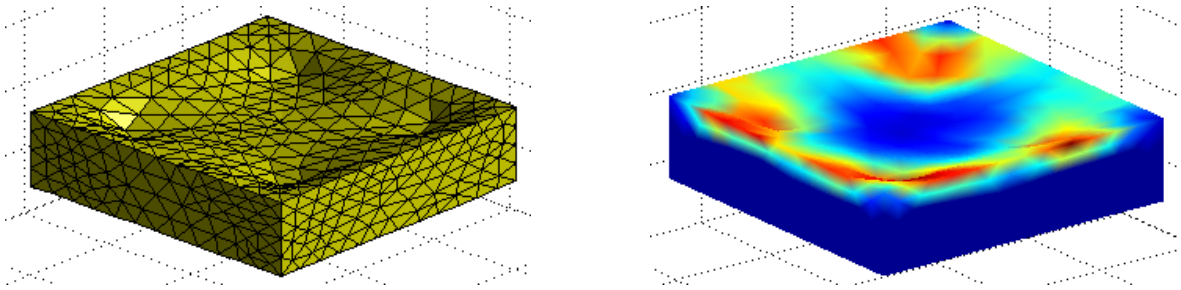

Figure 6.3. Deformation of soft tissue and stress concentration around insertion sites of four microneedles at insertion depth of 200 μm.

Figure 6.4(A) shows deformation of soft tissue with Young's modulus of 0.2 MPa (Silicone rubber). Figure 6.4(B) shows deformation of human skin where the Stratum Corneum (outermost layer) has the Young's modulus of 1 GPa. Deformation of soft tissue with high Young's modulus is rather shallow but covers large area. Soft tissue with low Young's modulus, on the other hand, has deeper deformation but the severity is confined at small area.

Figure 6.5 shows an example of puncture point by a sharp bevel microneedle. For silicone rubber, it was found that the sharp bevel microneedle can easily puncture into the material. The insertion depth of less than 20 μm was sufficient to create a pressure larger than the critical pressure (which is about 0.663 MPa on the average). A blunt bevel microneedle made a successful puncture at the insertion depth further than 250 μm. This is more than 10

times of the required insertion depth of the sharp bevel microneedle. And a cylinder microneedle was found to puncture at the insertion depth larger than 500 μm.

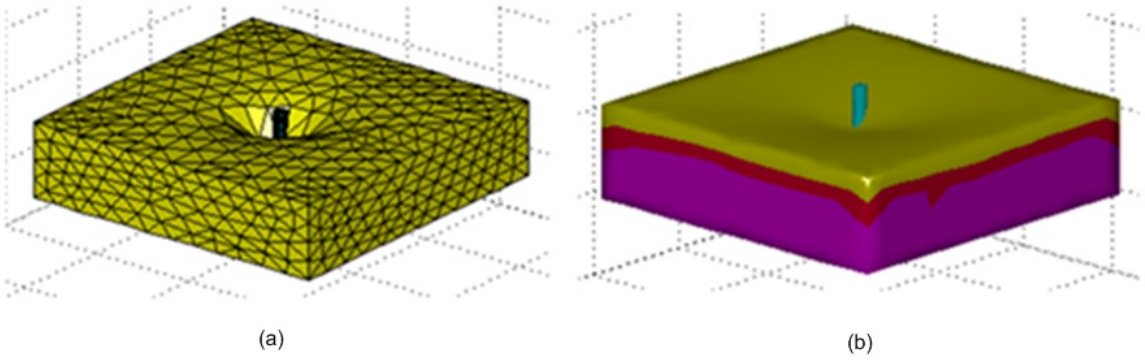

Figure 6.4. Deformation of soft tissue with different Young's modulus. (a) Young's modulus is 0.2 MPa. (b) Young's modulus at top, middle, bottom layers are 1 GPa, 0.134 MPa, and 0.08 MPa respectively

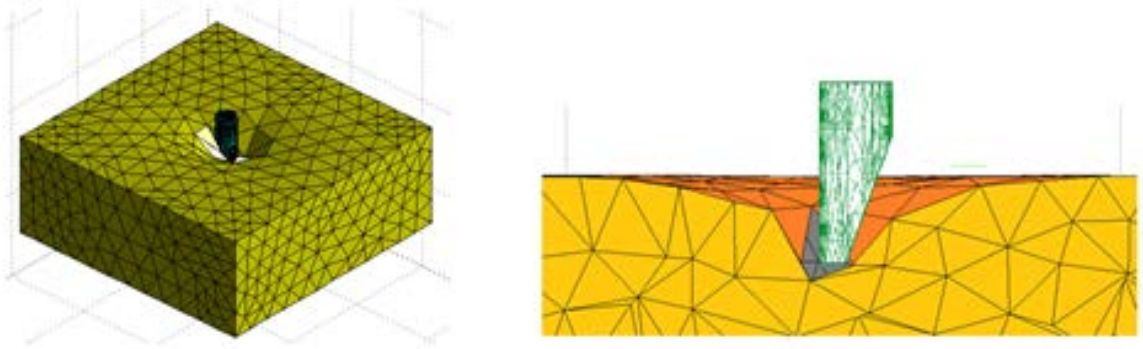

Figure 6.5. Profile of sharp bevel microneedle and soft tissue at puncture point.

Figure 6.6 shows a predicted insertion force when tissue property changes. With Young's modulus of 0.2 and 0.5 MPa, and tissue phantom which has the following dimension: diameter = 44.107 mm, height = 21.145 mm, tissue toughness of 1.043 x 10^{-7}

and 2.607 x 10^{-7} can be achieved. As shown in Figure 6.6, for an application where a blunt microneedle needs to penetrate into soft tissue phantom further than 300 μm (for bio-sampling, the microneedle must penetrate into human skin deeper than 700 μm), microneedle must be strong enough to withstand the force of 0.14 N. Therefore a microneedle that cannot resist this load should not be selected for the application. This is an example on how the insertion force model is used to pre-screening the microneedles. The technique can also be applied to various soft tissue properties.

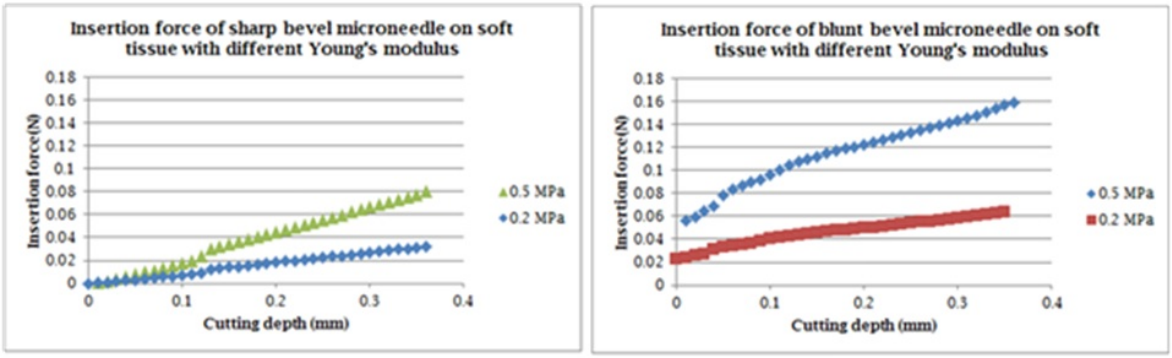

(a) (b)

Figure 6.6. The predicted insertion force of (a) sharp bevel microneedle and (b) blunt bevel microneedle when Young's modulus changes from 0.2 MPa to 0.5 MPa.

To investigate insertion force created by microneedles of different geometries, a number of experiments were conducted. Figure 6.7 shows different needle geometries used in the experiments. As shown in Figure 6.7, sharp bevel, blunt bevel and cylindrical needles were used in the experiments. All needles were fabricated out of silicon, with internal and external diameter of about 90 and 230 μm respectively. The flat area on the blunt bevel needle is approximately 50 μm wide. The tissue phantom was made from translucent silicone

rubber (Mold Max® 10T). Young's modulus of this silicone rubber is approximately 29 psi (0.2 MPa). While Young's modulus of human stratum corneum, epidermis, and dermis are 1 GPa, 0.134 MPa, and 0.08 MPa respectively, the silicone rubber positions itself slightly above the epidermis. For each set of experiment, the needle and tissue phantom were mounted onto the ElectroForce® 3100 test instrument as shown in Figure 6.8 In the experiment, the needle was slowly driven toward the tissue phantom at a constant speed until it reached the maximum needle displacement of 1 mm for sharp bevel needle and 2 mm for blunt bevel and cylindrical needle.

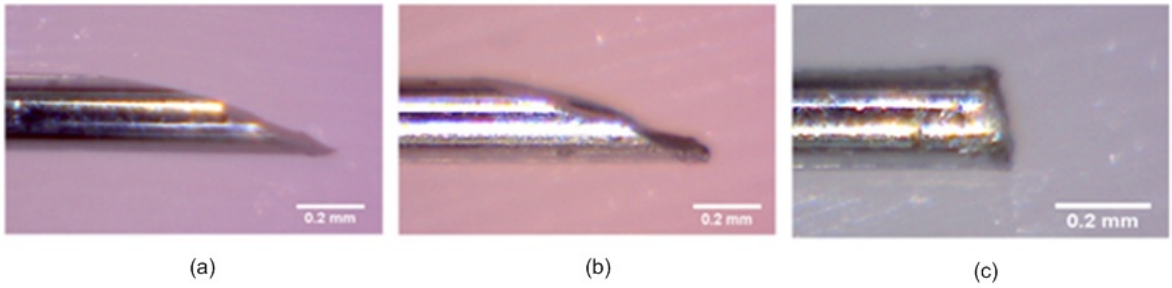

Figure 6.7. Three different needle tip used in the experiments: (a) sharp bevel tip needle, (b) blunt bevel tip needle, (c) cylindrical needle.

Figure 6.9 shows different insertion forces relative to insertion depth of all three microneedles used in our experiments. From the observation of experiments, once microneedle touched the tissue phantom, the insertion force increased with the increase of insertion depth. As expected, a sharp bevel needle encounters a much less insertion force, while a cylinder needle causes the largest insertion force, as shown in Figure 6.9. The blunt tip and the cylinder tip microneedles encountered higher penetration resistance, but once the

microneedles penetrated the tissue, the distance force dropped slightly, as shown in Figure 6.9. For the sharp bevel needle, it reached the maximum distance with much less resistance from the tissue and rapidly reached the maximum depth of insertion. In figure 6.9, we believe that the drop in force resistance after microneedle insertion could be due to the relaxation of tissue phantom. Similar phenomenon in needle insertion into liver had been reported earlier [Maurin 2004].

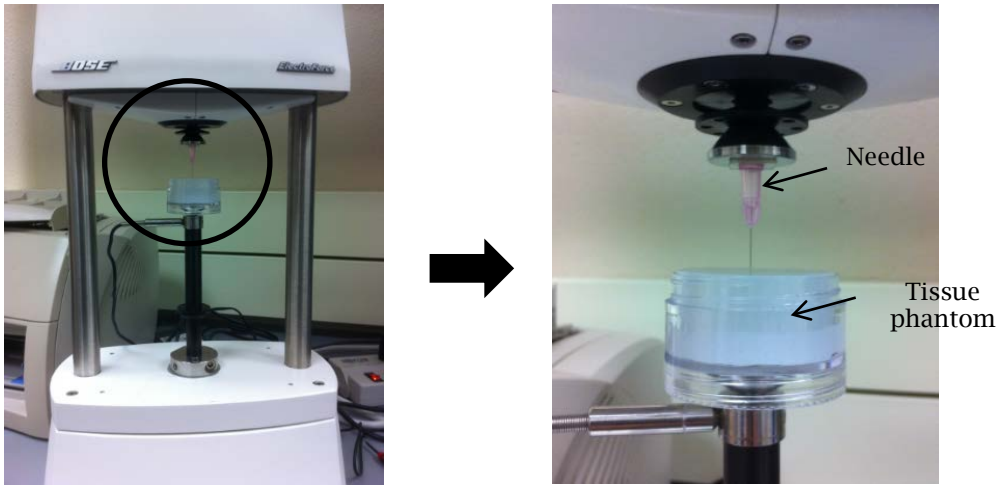

Figure 6.8. ElectroForce® 3100 test instrument with a needle and tissue phantom mounted on it.

Sharp and blunt bevel microneedles reached puncture point at approximately 0.23 mm and 1.226 mm respectively. These puncture point were achieved with insertion force of 0.014 N and 0.217 N with average critical pressure of 0.663 MPa at the tip. Figure 6.10 shows puncture point of sharp and blunt bevel microneedle. There was no puncture point for cylinder needle as it didn't penetrate the tissue phantom within 2 mm of needle displacement. From the data, sharp needle can penetrate into the tissue phantom quite easily compared to

other needles. Although blunt needle can also reach the puncture point, it needs to traverse four times more than the sharp needle and thus causes more deformation to the tissue phantom. Also, the relationship between the force and insertion depth appeared to change from second degree polynomial to linear.

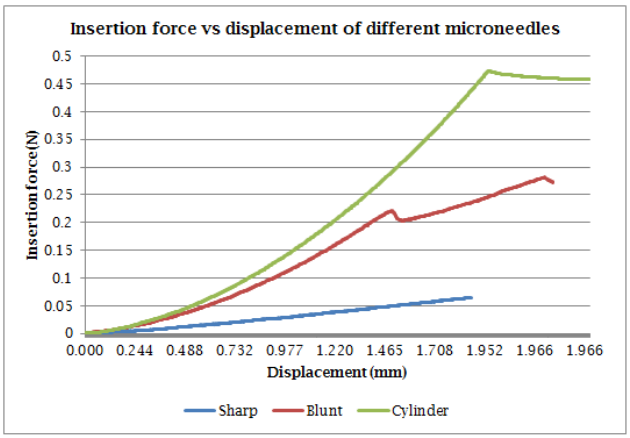

Figure 6.9. Different insertion force relative to insertion depth of sharp, blunt bevel microneedle, and cylinder microneedle.

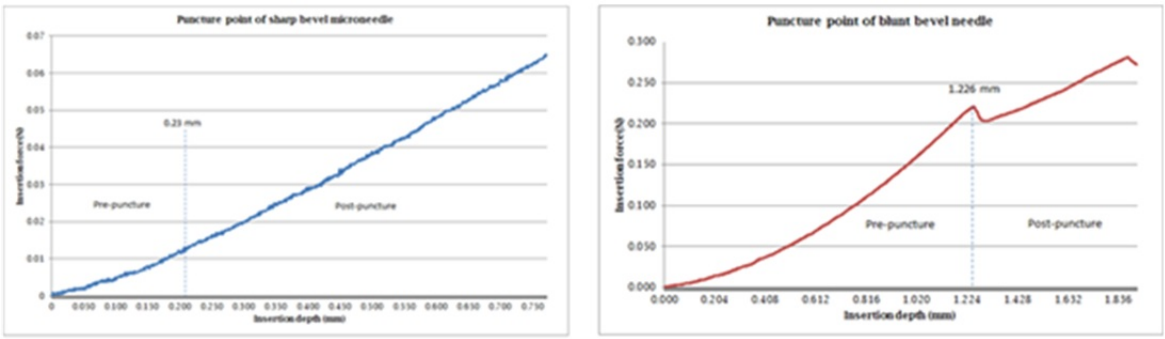

(a) (b)

Figure 6.10. Puncture point of (a) sharp bevel microneedle and (b) blunt bevel microneedle.

To evaluate our developed post-puncture force modeling, we conducted simulations of using the solid needles of sharp bevel, blunt bevel, and cylindrical needle shapes inserting on the silicone rubber material in the experiments. Figure 6.11 shows the result data obtained from the experiments conducted and the simulations results based on the presented analytical models. Figure 6.11 shows the comparison between the computed and experimental data of sharp bevel microneedle. The presented algorithm is able to approximate the post-puncture function of the sharp bevel microneedle quite reasonably well. To model the relationship of the adhesion force and cutting area, more experiment on various tip angles may be needed.

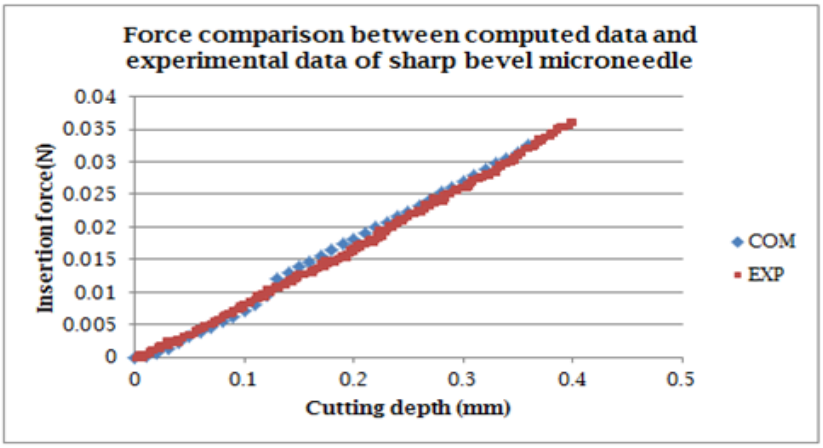

Figure 6.11. Comparison of experimental and simulation results of the insertion force and cutting depth by a sharp bevel microneedle at parameter $S = 0.168$.

The obtained results were also supported by actual microneedle insertion experiments. In this experiment, a microneedle array was pressed against a tissue phantom made from the silicone rubber. Microneedle arrays that hold four conic microneedles were built using a Perfactory® DDP4 Rapid Prototyping System. The machine uses Direct Light

Projection technology to produce parts in wax-based polymer and glass-filled composites. The microneedles and substrates were fabricated from envisionTEC e-Shell 300 material which is a biocompatible photo-reactive acrylate. The conic microneedles are about 700 μm long and 500 μm wide at the base. Each microneedle is located approximately 2 mm away from each other. The substrate has dimension of 5x5x1 mm. Figure 6.12 illustrates an example of microneedle array used in the insertion experiment.

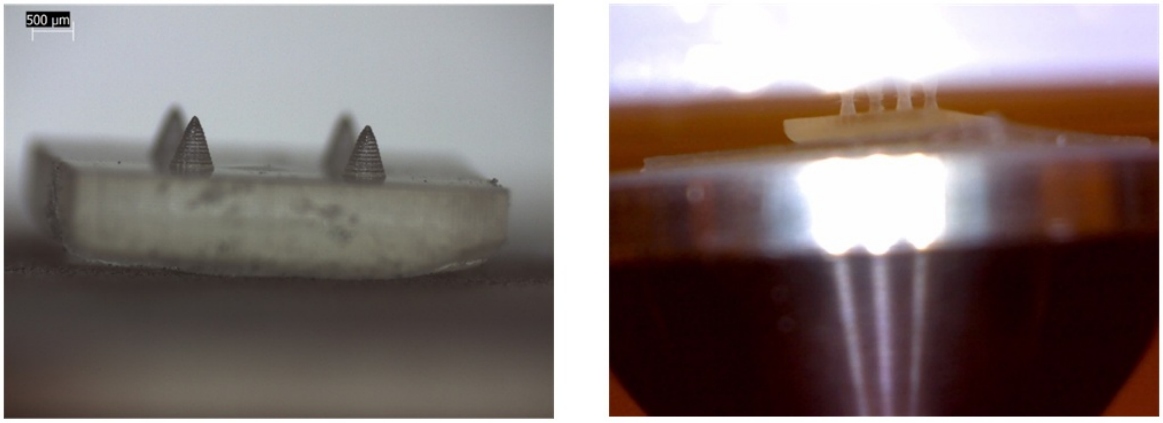

Figure 6.12. Microneedle array used in insertion experiment. (a) Side view of microneedle array. (b) Microneedle array during insertion.

The insertion force obtained from microneedle insertion experiments show nonlinear relationship between the insertion force and displacement (Figure 6.13). The nonlinearity assumes the shape of 2nd polynomial similar to that shown in Figure 6.9. The magnitude of the insertion force is also larger than that shown in Figure 6.9 since the array contains four microneedles rather than one. Moreover, as the microneedles have sharp tip, the point of puncture where the insertion force drops cannot be identified clearly.

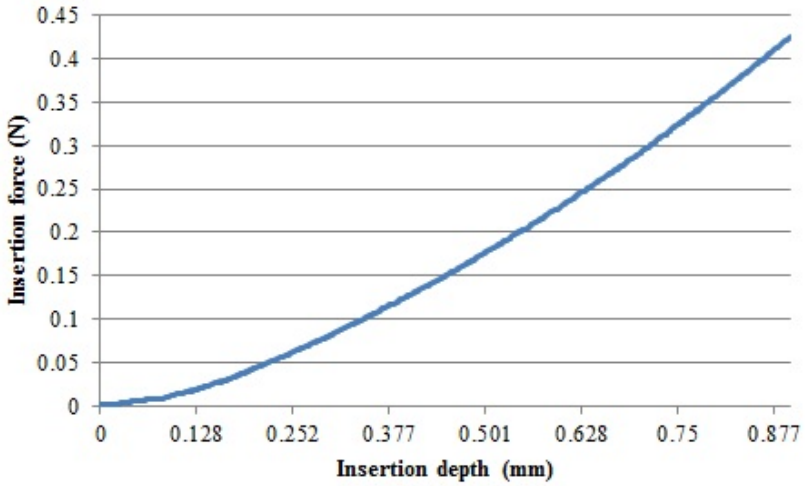

Figure 6.13. Insertion force of microneedle array containing four conic microneedles into silicone rubber.

6.3 Example uses of Microneedle Performance Index in evaluating and optimizing microneedle designs

The presented technique was implemented in Matlab R2009a and run on a Intel® Core™ i3 CPU M380 @ 2.53 GHz personal computer with 4 GB RAM, Intel® HD Graphics, and 64 bit Windows 7. To demonstrate the concept of the Microneedle Performance Index, we present the following cases where solid and hollow microneedles assuming different shapes are compared between each other. All hollow microneedle have similar channel size of about 20 μm. Each microneedle has different geometries such as cylindrical, conic, or bevel. The cylindrical microneedle is about 95 μm in diameter and 500 μm long. The conic microneedle is approximately 30 μm in tip diameter, 150 μm in base diameter, and500 μm long. Lastly, the bevel microneedle is about 30 μm in tip size (D_1), 120 μm in base diameter and 500 μm long. Some of these parameters were modified slightly to accommodate the computation. Dimension of each microneedle is carefully selected such

that volumes of these microneedles are comparable to each other. Design parameters of these microneedle arrays are shown in Table 6.1. All microneedles are fabricated from the same material which in this case is Silicon. Lastly we assume that 100 microneedles of each shape are fabricated on a 1 cm x 1 cm substrate as shown in Figure 6.14.

Table 6.1. Geometric parameters of the cylindrical, conic, and bevel microneedles used in this study.

Parameters	Cylinder	Cone	Bevel
Number of needles per row/column (*n*)	10	10	10
Tip diameter (D_1)	95 μm	30 μm	30 μm
Base diameter (D_2)	95 μm	150 μm	120 μm
Width of the patch (*w*)	1 cm	1 cm	1 cm
Length of needles (*L*)	500 μm	500 μm	500 μm
Epidermis thickness (*H*)	50 μm	50 μm	50 μm
Volume (μm^3)	3,544,109	3,652,104	3,618,763
Young's modulus (*E*)	169 GPa (Silicon)		

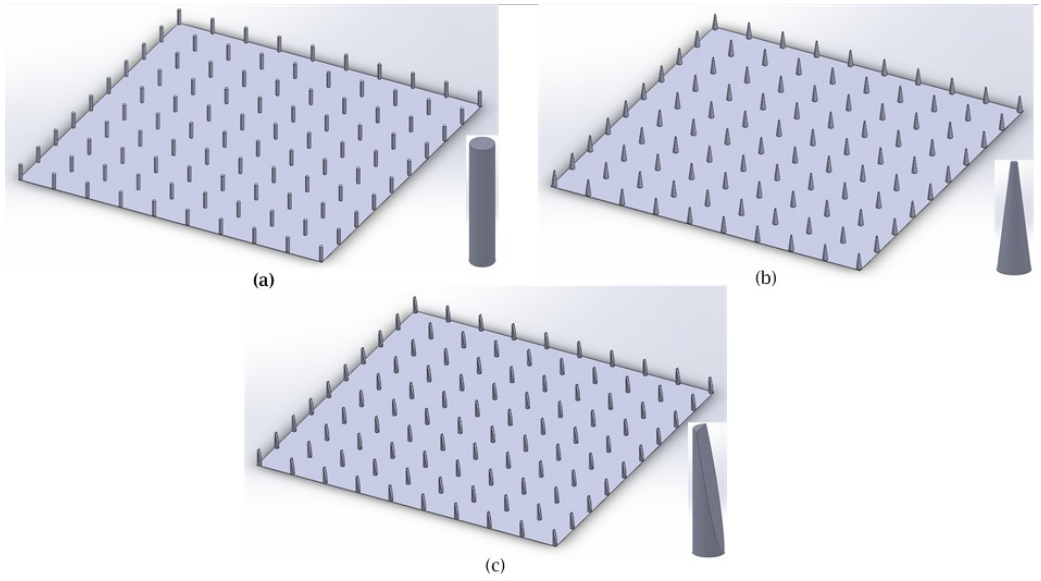

Figure 6.14. Microneedle geometries used in this study, including; (a) Cylindrical microneedle, (b) Conic microneedle and (c) Bevel microneedle.

6.3.1 Microneedle Performance Index of sample cylindrical, conic, and bevel microneedles

We assume that the ideal permeation depth is identical to the depth of interface layer between Epidermis and Dermis, which is about 50 μm beneath the skin surface. Microneedle Performance Index is computed for all microneedles. It was found that the MPI for both solid and hollow cylindrical microneedle becomes zero as the length of cylindrical microneedle is not long enough to overcome tissue deformation before puncture. This finding is supported by the buckling force applied on the cylindrical microneedle array. Figure 6.15 shows large buckling force (0.7405 – 0.8778) distributed over the cylindrical microneedle array.

However, this is partly due to our assumption that all microneedles are pushed against the skin by the distance equals to the length of microneedle only, no "finger-press" is allowed. Therefore, the length of micronedle (500 μm) is not long enough to overcome the skin deformation (580 μm). However, in a case where finger-press is allowed, the microneedle might be able to achieve successful penetration as it was reported earlier by [Teo 2005]. We believe the main reason for their successful puncture is that the skin may be compacted by other skin layers underneath and this reduces the amount of tissue deformation.

In case of solid and hollow conic microneedles, Microneedle Performance Indices of the solid and hollow conic microneedle fall within the range of about 1.4093×10^{-5} - 1.288×10^{-4}. The fact that MPI does not become zero indicates that these microneedles are able to penetrate into the skin as evidenced by lower buckling force (0.5668 - 0.6720 N) applied on the microneedle array (as shown in Figure 6.16). Conic microneedle can puncture into skin

due to its small tip size (67.4 μm) that generates skin deformation of only 42.9 μm from the skin surface. The penetration depth of the microneedle, as a result, is largely about 457 μm.

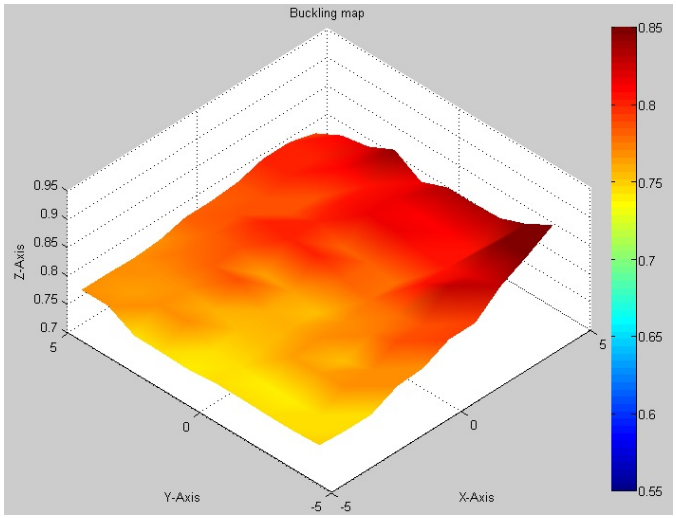

Figure 6.15. Buckling force distribution over cylindrical microneedle array. Minimum and maximum buckling forces are 0.7405 and 0.8778 N.

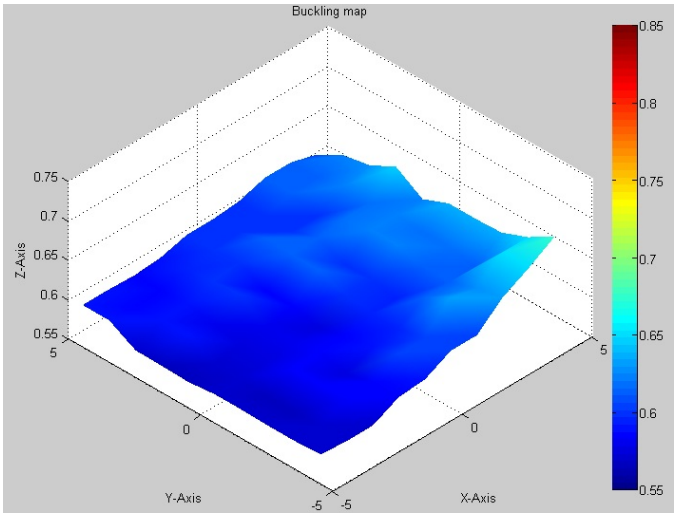

Figure 6.16. Buckling force distribution over conic microneedle array. Minimum and maximum bucklng forces are 0.5668 and 0.6720 N. The values are lower than that in previous cylindrical microneedle.

Microneedle Performance Index of the solid and hollow bevel microneedle can be calculated similar to the case of conic microneedle. The MPI of the solid bevel microneedle is about 1.197 x 10^{-4}, while the MPI of the hollow one is about 1.637x10^{-5}. The bevel tip creates skin deformation of 134.4 μm from the skin surface. The penetration depth of this microneedle is about 365.6 μm. Figure 6.17 shows the resulting MPI of the given microneedles.

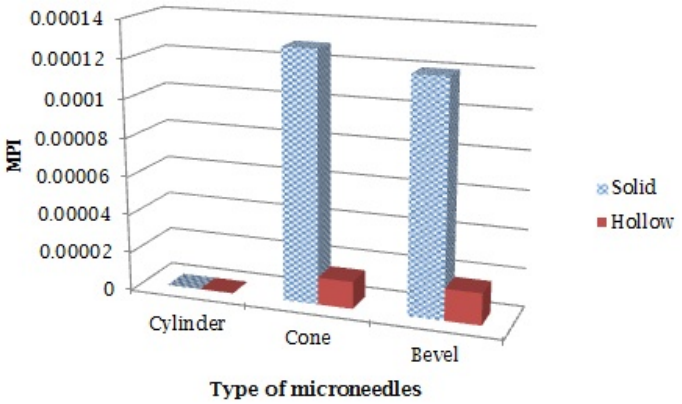

Figure 6.17. MPI of microneedles used in this study. MPI of cylinder microneedle becomes zero since the microneedle does not penetrate into the skin (amount of tissue deformation is larger than the length of microneedle).

The significant decrease in Microneedle Performance Index in hollow microneedles indicates the reduction of skin permeation. It appears that hollow microneedles perform much worse than solid microneedles of similar design. This is probably because drugs have to travel in longer distance before they can dissolve with the body fluid. Moreover, it was found that the conic microneedle performs best in transdermal drug delivery based on the

given microneedle parameters. However, it is not clear at this point which design parameter the MPI is dependent upon.

We therefore investigate the effect of design parameters such as tip diameter, base diameter, or the length of microneedle by varying the magnitude of each parameter one at a time, while the others remain constant. As shown in Figure 6.18 and 6.19, we found that both solid and hollow microneedles demonstrate similar response toward changes in base diameter. As the base diameter of conic microneedle increases by two folds, the Microneedle Performance Index increases accordingly by 3.25 folds on average. Change in the tip and length of microneedle, however, does not cause as much change in MPI compared to the base diameter. As microneedle is lengthen by two folds, the MPI increases by only 1.11 folds. Similarly, increasing tip diameter by two folds raises MPI by only 1.03 folds.

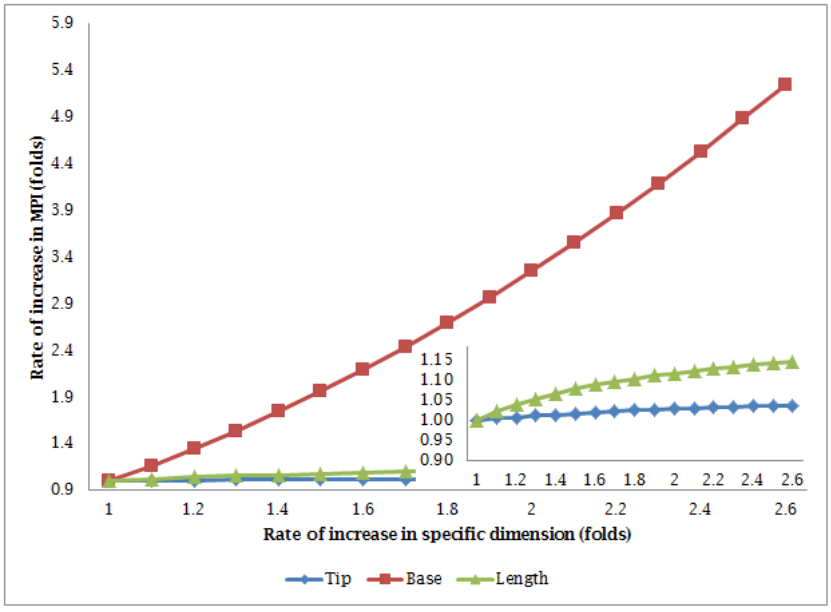

Figure 6.18. Change of Microneedle Performance Index of conic microneedles in relation to geometric parameters including tip size, base diameter, and length.

This finding suggests that the performance of transdermal microneedle can be best improved by increasing the base diameter. Although the length of microneedle may also help improving the performance of solid microneedles (it shows opposite effect in hollow microneedles though), we believe that fabricating microneedle such that it is just long enough to reach the ideal permeation depth should be sufficient. Also, as tip size does not play much important role compared to other parameters, we recommend that the tip size should be made relatively small to reduce the force of puncture and improve the ease of penetration.

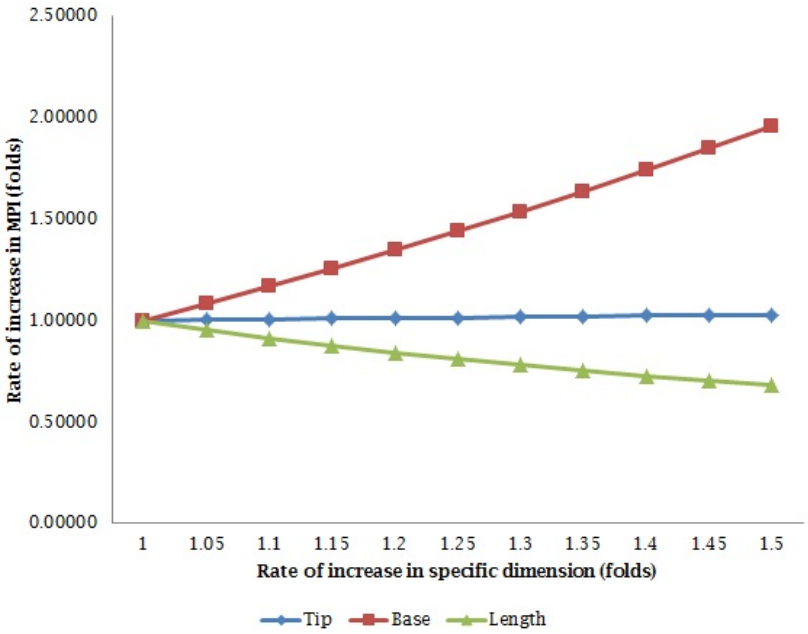

Figure 6.19. Change of Microneedle Performance Index of hollow conic microneedles in relation to geometric parameters including tip size, base diameter, and length.

Moreover, it should be noted that the obtained results are different from the work of [Olatunji 2009], where the tip radius appears to have higher effect on skin permeation compared to the base diameter. We believe this is due to their assumption that the whole

bodies of microneedles are embedded inside the soft tissue. Since the Microneedle Performance Index is developed base on the different assumption where microneedle may not be completely inside the soft tissue (e.g. microneedle will not be pressed further against the skin if the full length of microneedle already passes the original skin surface), the resulting data appears to be different.

To demonstrate that Microneedle Performance Index can be used in microneedle design, we aim to find the geometry that yield the highest value of Microneedle Performance Index. The process of obtaining the best microneedle design will be described next.

6.3.2 Evaluation of microneedle design based on the Microneedle Performance Index

With an attempt to find the microneedle design that yields the highest value of Microneedle Performance Index, we set the boundary of related input parameters as follows. Number of microneedles (n) ranges from 5 to 25 needles per row. Tip and base diameter of the microneedle (D_1, D_2) are from 30 - 150 μm and 30 – 300 μm respectively. Size of internal hole or pathway in the microneedles (D_3) is varied from 20 to 50 μm. The width of substrate (w) is between 5000 and 20000 μm. Finally, the length of microneedles (L) is ranging from 300 – 500 μm. All microneedles are fabricated from strong material such as Silicon. The input user interface is shown in Figure 6.20, while the summary of all input parameters is demonstrated in Table 6.2.

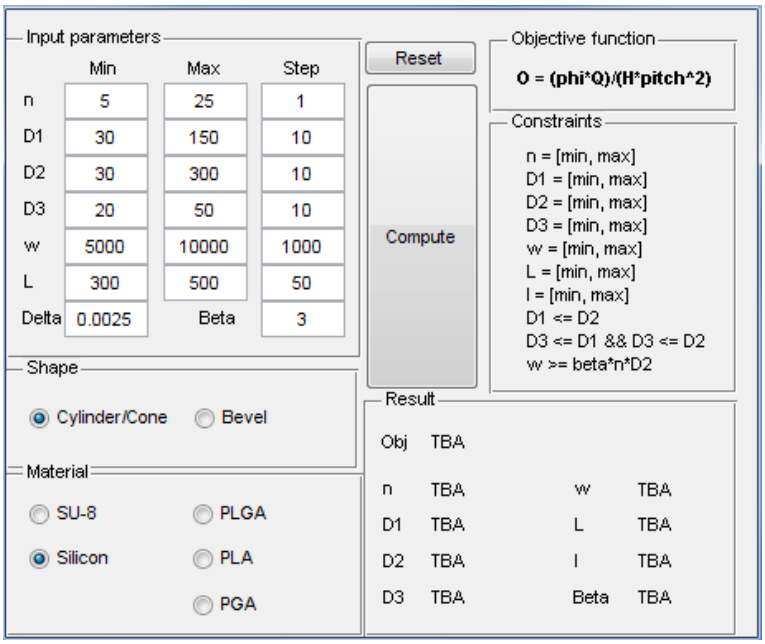

Figure 6.20. The input user interface of the developed computational engine.

Table 6.2 Summary of input parameters for obtaining the best microneedle design based on maximum Microneedle Performance Index.

Parameters	Min	Max
Number of needles per row (n)	5	25
Tip diameter (D_1)	70 μm	150 μm
Base diameter (D_2)	100 μm	300 μm
Hole diameter (D_3)	20 μm	50 μm
Width of the patch (w)	0.5 cm	2.0 cm
Length of needles (L)	300 μm	1000 μm
Constant parameter (δ)	0.0025	N/A
Epidermis thickness (H)	50 μm	N/A
Young's modulus (E) • Silicon	169 GPa	N/A

Among solid microneedles, cylindrical microneedle appears to have highest Microneedle Performance Index at 0.001745, compared to conic microneedle at 0.001447, and bevel microneedle at 0.001637. However, for hollow microneedles, bevel microneedle

yields highest MPI at 0.00111, while conic and cylindrical microneedle yield only 0.00061 and 0.00057 respectively. The design parameters of these microneedles are shown in Table 6.3.

Table 6.3. Design parameters of the best microneedle design.

Geometry	**Number of needle/row**	**Tip Size (μm)**	**Base Dia (μm)**	**Patch Width (μm)**	**Length (μm)**	**MPI**
Solid cylinder	25	80	80	6000	500	0.001745
Solid cone	25	70	80	6000	500	0.001447
Solid bevel	25	70	80	6000	500	0.001637
Hollow cylinder	25	80	80	6000	500	0.000569
Hollow cone	25	80	130	10000	500	0.00061
Hollow bevel	25	60	80	6000	350	0.001106

The reason that solid cylindrical microneedle yield the highest MPI can be explained by the ratio between the surface area of the embedded part and the skin volume under the patch. Among the three best geometries, the cylindrical microneedle has the highest surface area per skin volume while the ratio obtained from the conic microneedle is the lowest. In hollow microneedles, however, the bevel microneedle performs better than the others since it has the shortest traveling distance to the ideal permeation depth. Therefore, determination of the length of hollow microneedle is important especially when skin permeation is most concerned.

6.4 Example of surface fitting technique in design and analysis of flexible microneedle patch.

The presented technique was implemented using Microsoft Visual Studio 2010 and OpenGL. Some demonstrating figures are developed and displayed using Matlab R2009a. The programs are run on a Intel® Core™ i3 CPU M380 @ 2.53 GHz personal computer with 4 GB RAM, Intel® HD Graphics, and 64 bit Windows 7. A human neck model was used to illustrate the fitting of the flexible microneedle patch onto a free form surface. The neck model is a triangulated mesh model which consists of 79,092 triangles. We will show a comparison between rigid and flexible microneedle patch first. Then, more examples of flexible microneedle patch fitting onto different soft tissue will be presented and discussed.

6.4.1 Rigid VS flexible microneedle patch

Fitting a rigid substrate onto a skin surface was selected as a control group. The rigid patch with a square shape had the dimension of 10 x 10 mm and consisted of 100 solid cylindrical microneedles (10 microneedles in each row and column) with tip diameter of 70 μm, and length of 400 μm. The microneedles were considered as being fabricated from SU-8 photoresist that has the Young's modulus of about 4 – 5 GPa. Each spring in mass spring system representing the patch had a spring constant of 1 N/mm.

The results indicated the minimum and maximum values of Microneedle Performance Index were between 0.0 (no penetration) and 0.0289 respectively (0.0153 on average, and 1.5282 in total). The minimum and maximum buckling forces were 0.0768 and 0.0910 N respectively (0.0812 N on average), while the minimum and maximum bending forces were

about 0.0287 and 0.0567 N (0.0387 N on average). Figure 6.21(a) shows fitting of a 10x10 mm rigid microneedle patch onto a skin surface. Color maps of buckling and bending are shown in Figure 6.21(c) and 6.21(d) respectively.

Next, we created another example. This time, flexible microneedle patch with similar dimension as the previous rigid patch was fitted onto the same skin surface as shown in Figure 6.22. The patch was originally held above the skin model. The center of the patch was located at (0, 0, Z) where Z was larger than the highest Z value of any node on the skin surface. Once the fitting process started, the patch moved toward the skin in –Z direction. As the patch reached the surface, it gradually deformed according to the curvature of the skin. The severity of this deformation is dependent on the predetermined allowable energy in each spring. Since, the microneedles are assumed to be always oriented perpendicularly to the patch, the distance between the tips and the associated insertion points on the surface ($x_{i,j}$) can be calculated (e.g. using Equation (5.12)). Actual penetration depth of each microneedle was calculated by subtracting the indentation depth (d) from $x_{i,j}$. Finally, the Microneedle Performance Index (MPI) of the flexible microneedle patch can be computed using Equation (5.9).

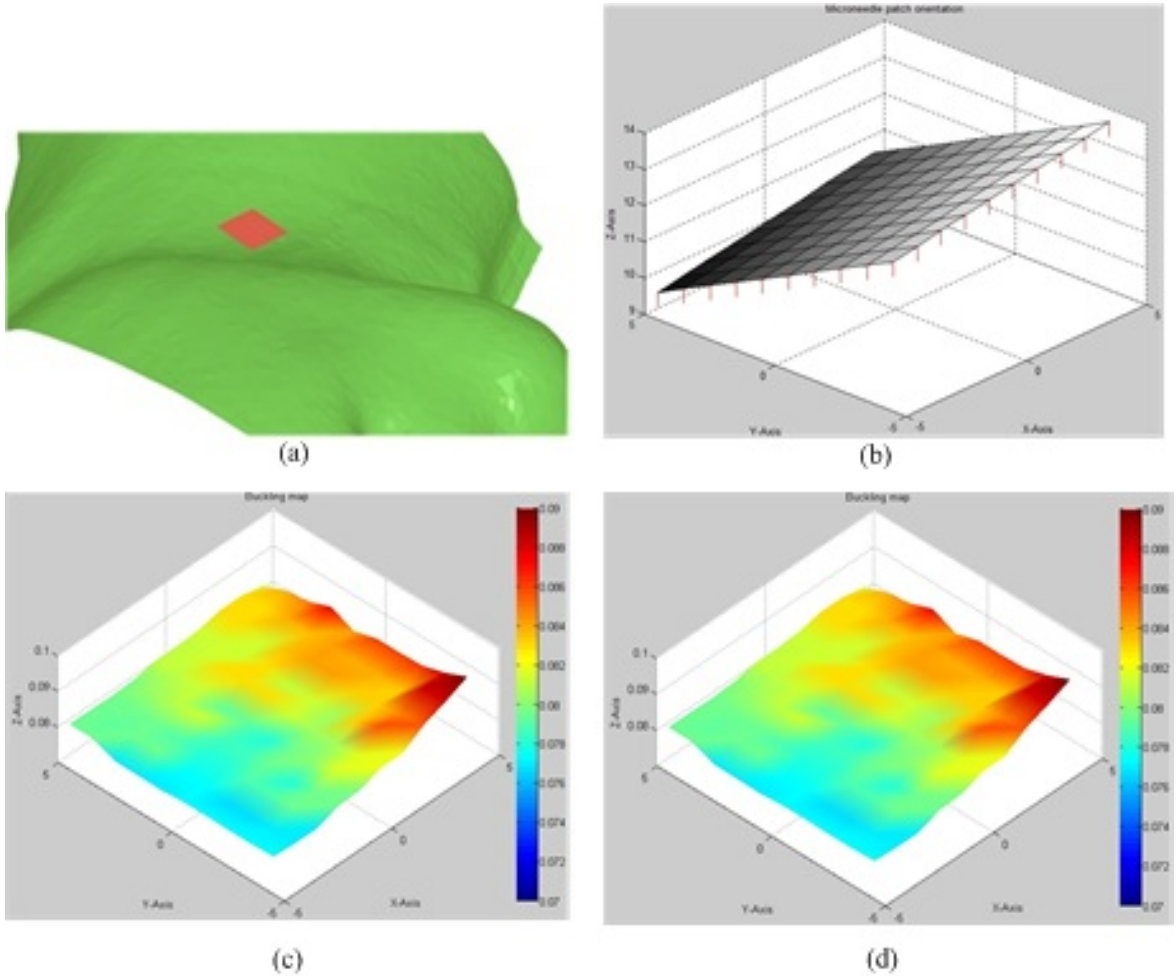

Figure 6.21. Fitting of a 10x10 rigid microneedle patch onto a skin surface. (a) Fitted rigid patch on the skin model. (b) Patch orientation after insertion. (c) Buckling force distribution [0.0768 N, 0.0910 N]. (d) Bending force distribution [0.0287 N, 0.0567 N].

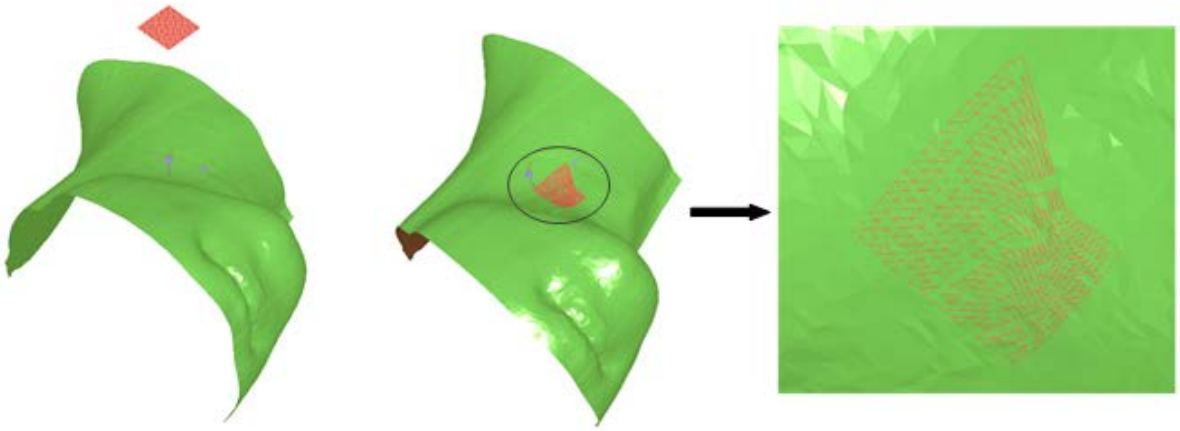

Figure 6.22. Flexible microneedle patch fitted on the free form skin surface.

It was found that Microneedle Performance Index appeared to be 0.0291 (2.91 in total). The minimum and maximum buckling forces were 0.0712 and 0.0715 N respectively (0.0712 N on average), while the minimum and maximum bending forces were 0.000183 and 0.0067 N (0.0021 N on average). Figure 6.23(a) shows fitting of a 10x10 mm flexible microneedle patch onto a skin surface. The orientation of the patch has changed according to the skin curvature as shown in Figure 6.23(b). Color maps of buckling and bending were drawn in similar scale as in the case of the rigid microneedle patch (shown in Figure 6.23(c) and 6.23(d)). Although there are some variations in the buckling and bending forces due to differences in skin curvature and insertion angle, the forces are obviously lower than that observed in the rigid microneedle patch.

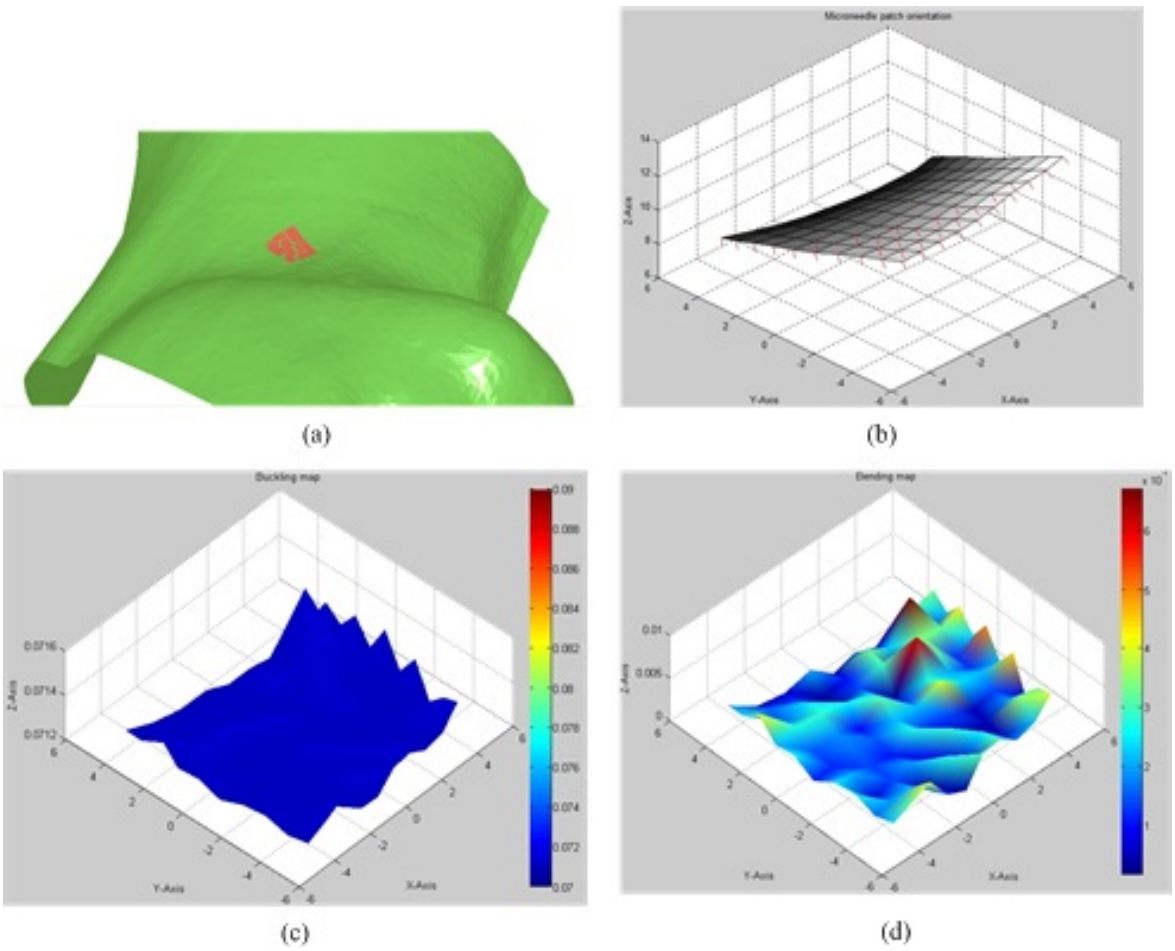

Figure 6.23. Fitting of a 10x10 flexible microneedle patch onto a skin surface. (a) Fitted rigid patch on the skin model. (b) Patch orientation after insertion. (c) Buckling force distribution is lower than rigid patch [0.0712 N, 0.0715 N]. (d) Bending force distribution. Fluctuation of the forces are caused by angled insertion.

The result data as shown in Figure 6.24(a) indicate that the flexible microneedle patch performs better than the rigid patch, as evidenced by higher MPI of almost two folds. Moreover, Figure 6.24(b) supports the previous color maps that the flexible microneedle patch tends to have lower buckling and bending forces. Thus, the microneedles on the patch may be less likely to suffer from damages such as buckling or bending compared to microneedles on a rigid substrate.

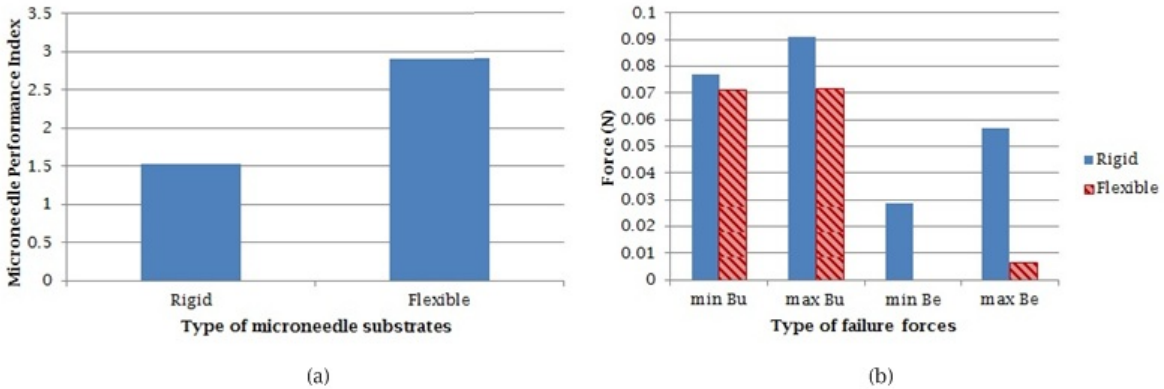

Figure 6.24. Comparison between the rigid and flexible microneedle patch. (a) Microneedle Performance Index. (b) Maximum and minimum values of buckling and bending force.

We will now show more examples on fitting flexible microneedle patch onto different types of soft tissues such as skin and brain. Depending on material properties, the effectiveness of flexible microneedle patch may be different.

6.4.2 Fitting flexible microneedle patch onto human skin

Two case studies based on different design parameters of microneedles were conducted to demonstrate the proposed methodology. In the first case, the flexible microneedle patch was simulated for use in the application of transdermal drug delivery or local chemotherapy where it is applied directly onto the human skin. The parameters related to physical parameters of the human skin were taken from the previous works [Boonma 2012a], and are shown in Table 6.4. The flexible microneedle patch had a square shape, the dimension of 20 x 20 mm, and consists of 400 solid cylindrical microneedles (20 microneedles in each row and column) with tip diameter of 50 and 70 µm, and length of 400

μm. The microneedles were considered as being fabricated from SU-8 photoresist that has the Young's modulus of about 4 – 5 GPa. Each spring in mass spring system representing the patch had a spring constant of 1 N/mm.

Table 6.4. Related parameters used in the first case study.

Parameters	Value
Parameter α	0.0183
Parameter τ	6.25 mm^{-1}
Number of microneedles	400
Type of microneedles	Solid
Geometry	Cylinder
Tip diameter (D_1)	50, 70 μm
Base diameter (D_2)	50, 70 μm
Width of the patch (w)	20 mm
Length of needles (L)	400 μm
Epidermis thickness (H)	50 μm
Young's modulus (E) • SU-8	 4-5 GPa

We will first discuss the flexibility of the patch and then move on to the Microneedle Performance Index and other related forces. As we have mentioned previously that, in this study, a mass spring system is used to demonstrate the behavior of flexible microneedle patch. Stretchability of each spring can be controlled by a parameter called the strain energy. If large energy is allowed, a spring can deform more and the whole microneedle patch can better conform to the target surface.

Figure 6.25 illustrates the average of Microneedle Performance Index in relation to the maximum allowable strain energy in each spring. The maximum allowable strain energy was varied within the range of 0.005 – 0.05 mJ/spring. As its magnitude increases, MPI

increases accordingly. This indicates that the very flexible microneedle patch may perform better on high curvature surface or on a very soft material (e.g. brain) where the curvature may change easily. However, making the substrate too soft may result in other problems. For example, microneedles may not be able to penetrate into skin as the substrate cannot provide enough insertion force. Therefore the balance between flexibility and affordable insertion force must be carefully determined.

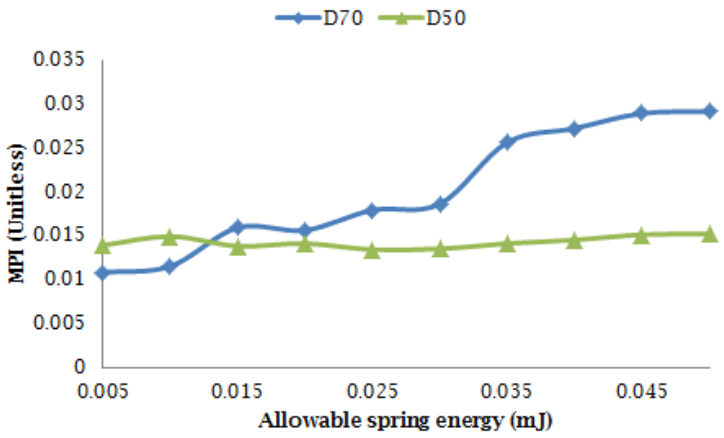

Figure 6.25. The relationship between the average of MPI (unitless) and the allowable spring energy in each spring (mJ).

Moreover, difference in microneedle size affects the performance of microneedles on a flexible patch similar to those on a rigid substrate. As shown in Figure 6.25, the minimum and maximum MPI of microneedles with 70 μm tip diameter were found to be 0.0108 and 0.0291 respectively. These values dropped to 0.0134 – 0.0152 when microneedle with 50 μm tip diameter was used. The slight fluctuation in the MPI may be caused by shallow insertion where some microneedles may not penetrate into skin due to their orientations. While the

patch deforms, some microneedles that encounter with steep skin surface may not be inserted deep enough to initiate the crack. In that case, the microneedles are considered as ineffective and MPI cannot be computed.

We will now discuss on the distribution of the forces over the flexible microneedle patch. Figure 6.26 shows the distribution of buckling and bending force on the flexible microneedle patch where the fabricated microneedles assume the shape of cylinder with tip diameter and length of 70 μm and 400 μm respectively. The maximum allowable strain energy was set to 0.5 mJ/spring (highly flexible). Figure 6.26(a) illustrates the final shape of the microneedle patch when it was fitted onto the skin surface. Figure 6.26(b) and 6.26(c) demonstrates the color maps of buckling and bending forces applied to the patch during the insertion process. The minimum and maximum buckling forces were found to be 0.0712 and 0.0727 N respectively (0.0713 N on average). Also, the minimum and maximum bending forces were 0.000134 and 0.0148 N (0.0031 N on average).

It appears that the magnitudes of buckling and bending forces are higher in the (+X, +Y) end, compared to the (-X,-Y) end. This is probably due to the insertion process and the skin curvature in the area that the microneedles were applied to the skin. In this simulation, when the patch approached the skin, the (-X,-Y) end of the patch reached the skin first. Also, the skin curvature is not so steep at that area. Thus, the difference in skin curvature and inserting direction is relative small and results in less fluctuation of the forces. This result indicates the importance of selecting the insertion spot. It is recommended that a microneedle patch, especially when the size is large, is to be placed on a relative flat area of skin in order

to minimize the damage to the needles due to buckling or bending, and the patch due to the internal stress.

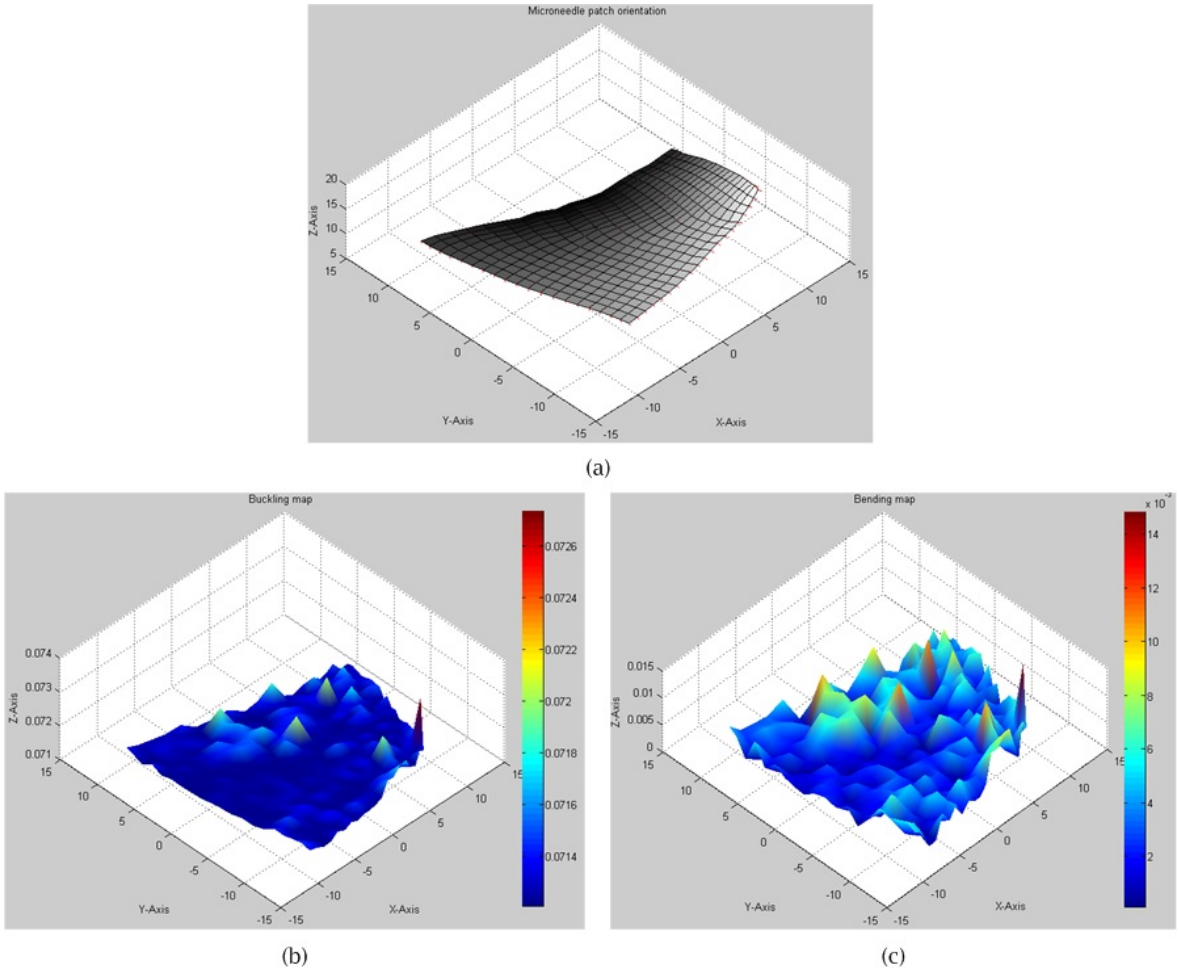

Figure 6.26. Color maps of buckling and bending force in the flexible microneedle patch. (A) Microneedle patch after being fitted onto the skin surface. (B) Buckling force distribution [0.0712 N, 0.0727 N]. (C) Bending force distribution on the patch.

6.4.3 Fitting flexible microneedle patch onto brain membrane

In the second case, a simulation was setup in order to demonstrate the process of fitting the flexible microneedle patch onto the brain membrane. We assume that the membrane, while remains inside the skull, takes the shape similar to the shape of skull. As for the material properties, it was reported that the Young's moduli of the incised and intact pia mater are about 0.089 and 1.4 MPa respectively [Mazuchowski 2003]. Our test material, silicone rubber (~ 0.2 MPa), falls within the range of these values [Boonma 2012a]. Therefore, as shown in Table 6.5, the parameters that determine the properties of the brain in were derived from the insertion of needle into silicone rubber.

In this simulation, the flexible microneedle patch had a square shape with the dimension of 10 x 10 mm, and consisted of 100 solid conic microneedles (10 microneedles in each row and column) with tip diameter of 70 μm, base diameter of 300 μm, and length of 1000 μm. The microneedles were again assumed to be fabricated from SU-8 photoresist similar to the previous cases.

Figure 6.27(a) shows the 20x20 mm microneedle patch as it is applied onto a human skull model. The human skull is a triangulated mesh model composed of 92,284 triangles. It was found that all conic microneedles penetrated the soft tissue successfully. No structural failures were detected during the insertion. The MPI was found to be 0.1184 and remained constant while the maximum allowable strain energy increased from 0.005 to 0.05 mJ. Similar result was found on a smaller patch as well. For 10x10 mm microneedle patch, the average MPI remained at 0.0289 for the entire range of the allowable strain energy. This

indicates that the rigidity of these patches does not have significant effect on the skin permeability for the selected insertion spot.

Table 6.5. Related parameters used in the second case study.

Parameters	Value
Parameter α	0.0013
Parameter τ	8.5076
Number of microneedles	100
Type of microneedles	Solid
Geometry	Cone
Tip diameter (D_1)	70 μm
Base diameter (D_2)	300 μm
Width of the patch (w)	10, 20 mm
Length of needles (L)	1000 μm
Brain tissue thickness (H)	50 μm
Young's modulus (E) • SU-8	 4-5 GPa

Figures 6.27(c) and 6.27(d) illustrate the color maps of buckling and bending forces applied to the patch during the insertion process. The minimum and maximum buckling forces were found to be 0.0712 and 0.0718 N respectively (0.0713 on average), while the minimum and maximum bending forces were 0.000052 and 0.0094 N (0.0022 N on average). Both buckling and bending forces were way below the associated critical loads (2.98 and 0.64 N respectively), and thus did not cause needle damage. From Figures 6.27(c) and 6.27(d), buckling and bending force were uniformly distributed across the entire patch. This indicates that the change in curvature of the soft tissue is quite smooth and thus the deformation of each mass node on the patch is rather small.

Although our result demonstrates that there is no significant different between rigid and flexible substrate, we still believe that the flexible patch should be used in brain probing and stimulation where the device must be implanted inside the skull. The reasons are; 1) flexible microneedle patch yields same penetration performance similar to rigid patch, 2) flexible patch offer better performance when larger patch is required especially when large area of motor cortex is being observed, 3) the patch is more likely to remain in the insertion spot since it is less affected by the curvature of soft tissue, 4) when the patch conforms to skull curvature, the external force applied on the patch may be distributed evenly and thus reduces the possibility of dislocation of the patch and brain damage due to concentrated force.

Moreover, in our experiment, it appears the buckling is the primary mode of failure even in high skin curvature area. Therefore, the microneedle geometry that is suitable for the flexible patch should be able to withstand buckling. Base on the theory of elasticity in beam and column, cone is more robust and has higher resistance to buckling than cylindrical shape. It therefore should be used in the fabrication of flexible microneedle patch.

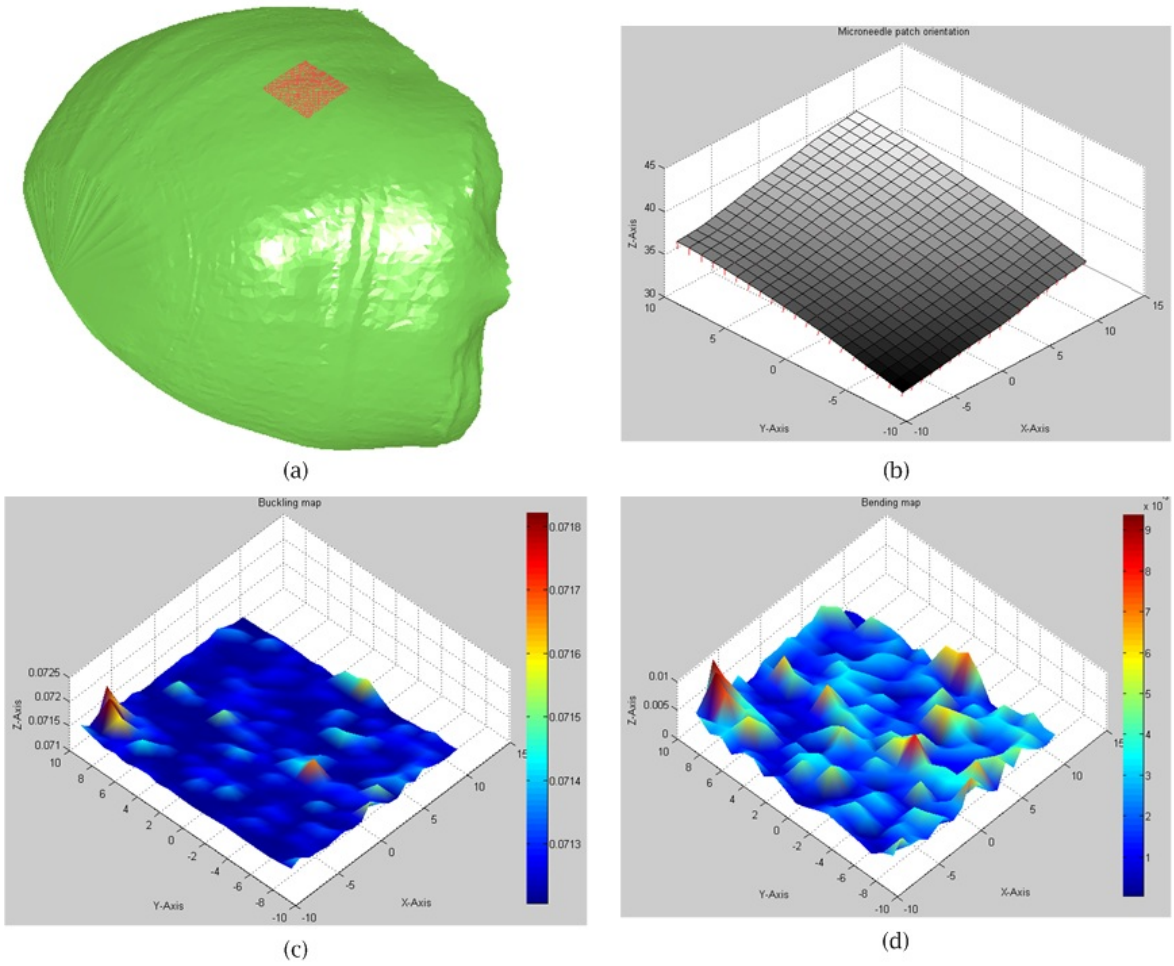

Figure 6.27. Fitting of 20x20 mm flexible microneedle patch on a human skull model. (a) Fitted microneedle patch on the human skull. (b) Microneedle patch orientation after being fitted onto the skin surface. (c) Buckling force distribution [0.0712 N, 0.0718 N]. (d) Bending force distribution.

6.5 Summary

This chapter presents some preliminary examples of the proposed techniques. These results demonstrate that the proposed two stage force modeling method, Microneedle Performance Index, and the energy based surface fitting technique can be used in analytical design and evaluation of microneedles and may be extended to other biomedical devices.

Combination of the developed techniques and virtual reality can enhance the capability of the design analysis and evaluation. Future research in this area may lead to further understanding in micro-interaction between soft tissue and medical devices and even the development of new inventions for diagnosis and treatment of diseases.

CHAPTER 7

CONCLUSIONS AND FUTURE WORKS

The primary objective of this research is to investigate the interaction between soft tissue and biomedical devices (especially microneedle) and develop analytical tools that may be used in design, evaluation, and analysis of both current and future designs of such devices. The presented techniques can be used in product design and evaluation in various simulated environments. Detail analytical and computation have been discussed in this paper. This chapter provides some conclusion remarks and the future research.

7.1 Conclusions

The contributions of this paper can be summarized as follows:

- Modeling techniques of heterogeneous soft tissue model have been proposed for the medical design and development of micro-interaction models between biomedical devices and soft tissue. The developed heterogeneous soft tissue can be used as tissue phantom for prediction of the insertion force and tissue deformation when it is interacted with biomedical devices.
- The two stage insertion force models have been presented for predicting the possible response of soft tissue and medical devices under various circumstances and material properties. The techniques combine several conceptual theories including finite element method, fracture mechanics, computational geometry,

and distribution load, and provide the results that may be used in design and analysis of biomedical devices especially in micro-scale.

- Microneedle Performance Index is proposed for analytical evaluation and analysis of current microneedle designs, and may be used in finding suitable design parameters based on skin anatomy, given 3D geometric parameters of microneedle and the desired cutting depth. The technique may be extended to other biomedical devices of similar nature.
- Energy based surface fitting technique is proposed for design, analysis, and evaluation of futuristic microneedle array. The methods combine the concepts of mass spring, node sweeping, geodesic distance, and energy minimization to predict the orientation and characteristics of flexible microneedle patch when it is applied on various soft tissues. The method may be extended to other applications such as brain probing and stimulation, collagen induction, skin rejuvenation, tattooing, and etc.

Analytical models, algorithms development, computer implementation and practical examples have been presented for design and analysis of biomedical devices under different circumstances and conditions. The techniques presented in this dissertation can lead to more effective design and development of biomedical devices especially microneedles. This research may enhance understanding and knowledge of micro-scale soft tissue properties, interactions between soft tissue and medical tools, and also design and analysis of new medical devices.

7.2 Future research

The proposed techniques can be further improved for higher accuracy and simulation of various types of soft tissues and microneedle designs. Based on the developed techniques in this paper, future research may be extended as follows.

- The heterogeneous soft tissue model can be enhanced by increasing the resolution of the model and integrating larger variety of soft tissue properties. As the soft tissue model consists of a set of tetrahedrons. Increasing number of tetrahedrons will make the finite element computation more accurate. Also, adding many types of soft tissue makes the model becoming more soft tissue-liked. These improvements can be achieved with larger computational resource.
- The interaction model between soft tissue and microneedle can be further improved by conducting more needle insertion experiments with various microneedle sizes and designs, and various soft tissue conditions. Angled insertion should be considered as it is more practical and identical to the real situation where microneedles are used.
- Microneedle Performance Index can be extended to more variety of microneedle designs, although some designs may be complex and difficult to formulate into mathematical representation. Finite element-liked or piecewise MPI may be more suitable for analysis and evaluation of complex microneedle designs.
- The energy based surface fitting algorithm, soft tissue modeling, and Microneedle Performance Index can all be integrated with virtual environment and haptic devices. This will allow a simulation where microneedle patch can be

manipulated and applied onto virtual soft tissue e.g. skin or brain. With the development of this technique, doctors can plan ahead where to apply the microneedle probe on the brain, skin, or other organs such that it will be most effective and less invasive. Custom design of microneedle probe can be designed and fabricated such that it is attached perfectly to the skull. This will improve long term implantation of the device in patients.

- Development of flexible microneedle patch may be limited by material property. Fabricating materials that remain sufficiently strong while being formulated onto a flexible patch are required. Fabrication methods that are able to produce this type of microneedle array are also needed.

This list only provides some examples of what could be conducted in near future. It is by no means a complete list. We believe that there is a huge opportunity for the related research to expand and be used in practical engineering and medical applications.

7.3 List of publications

From the contents of this research and previous studies, we have published some conference and journal papers. The following is the list of papers that have already been published, accepted, or are being prepared for publication.

Wongwiwat, P.; Boonma, A.; Lee, Y.-S.; Narayan, R. J.: Bioceramics in Ossicular Replacement Prostheses: A Review. Journal of Long-Term Effects of Medical Implants (2011), 21(2), 100.

Boonma, A.; Narayan, R. J.; Lee, Y.-S.: Analytical modeling and evaluation of microneedle apparatus with deformable soft tissues for biomedical applications. Overall Best Paper Award Winner. The International CAD Conference and Exhibition (2012), paper 44, Niagara Falls, Canada.

Boonma, A.; Narayan, R. J.; Lee, Y.-S.: Analytical modeling and evaluation of microneedle apparatus with deformable soft tissues for biomedical applications. Accepted for publication in Computer-Aided Design & Applications (2012), Vol 9.

Boonma, A.; Narayan, R. J.; Lee, Y.-S.: Analytical modeling and evaluation of microneedle designs for biomedical applications. Working paper (2012).

Boonma, A.; Narayan, R. J.; Lee, Y.-S.: Energy based surface fitting for microneedle design with flexible base evaluation. Working paper (2012)

REFERENCES

[Abolhassani 2007] Abolhassani, N.; Patel, R.; Moallem, M.: Needle insertion into soft tissue: a survey. Medical Engineering & Physics 29 (2007), 413 – 431.

[ADA 2005] American Diabetes Association. Total prevalence of diabetes & prediabetes (2005).

[Aggarwal 2004] Aggarwal, P.; Johnston, C. R.: Geometrical effects in mechanical characterizing of microneedle for biomedical applications. Sensors and Actuators B (2004), 102, 226-234.

[Al-Qallaf 2008] Al-Qallaf, B.; Das, D. B.: Optimization of square microneedle arrays for increasing drug permeability in skin. Chemical Engineering Science 63 (2008), 2523 – 2535.

[Aoyagi 2008] Aoyagi, S.; Izumi, H.; Fukuda, M.: Biodegradable polymer needle with various tip angles and consideration on insertion mechanism of mosquito's proboscis. Sensors and actuators A (2008), 143, 20 – 28.

[Asanuma 1975] Asanuma, H.: Recent developments in the study of the columnar arrangement of neurons within the motor cortex. Physiol. Rev. (1975), 55(2), 143 – 155.

[Bader 1983] Bader, D. L.; Bowker, P.: Mechanical characteristics of skin and underlying tissues in vivo. Biomaterials (1983), 4, 305 – 308.

[Bielser 2000] Bielser, D.; Gross, M.: Interactive simulation of surgical cuts. Proceedings of Pacific Graphics (2000), Hong Kong, China, October 2000, 116–125.

[Birchall 2011] Birchall, J.C.; Clemo, R.; Anstey, A.; John, D.N.: Microneedles in clinical practice-an exploratory study into the opinions of healthcare professionals and the public. Pharm Res 28 (2011), 95 – 106.

[Boonma 2012a] Boonma, A.; Narayan, R. J.; Lee, Y.-S.: Analytical modeling and evaluation of microneedle apparatus with deformable soft tissues for biomedical applications. Accepted for publication in Computer-Aided Design & Applications (2012), Vol 9.

[Boonma 2012b] Boonma, A.; Narayan, R. J.; Lee, Y.-S.: Analytical modeling and evaluation of microneedle designs for biomedical applications. Working paper (2012)

[Boonma 2012c] Boonma, A.; Narayan, R. J.; Lee, Y.-S.: Energy based surface fitting for microneedle design with flexible base evaluation. Working paper (2012)

[Bergstrom 2001] Bergstrom, J.S.; Boyce, M. C.: Constitutive modeling of the time dependent and cyclic loading of elastomers and application to soft biological tissues. Mech Mater (2001), 33, 523 – 530.

[Bostwick 1997] Bostwick, D. G.; Iczkowski, K. A.: Minimal criteria for the diagnosis of prostate cancere on needle biopsy. Annals of Diagnostic Pathology (1997), 1(2), 104 – 129.

[Campbell 1991] Campbell, P. K.; Jones, K. E.; Huber, R. J.; Horch, K. W.; Norman, R. A.: A silicon-based, three-dimensional neural interface: manufacturing processes for an intracortical electrode array IEEE Trans. Biomed. Eng. (1991), 38, 758–768.

[Carter 2001] Carter, F. J.; Frank, T. G.; Davies, P. J.: Measurements and modeling of the compliance of human and porcine organs. Medical Image Analysis (2001), 5, 231 – 236.

[Cheung 2000] Cheung, K.; Gun, L.; Djupsund, K.; Yang, D.; Lee, L. P.: A new neural probe using SOI wafers with topological interlocking mechanisms. 1st annual international IEEE-EMBS special topic conference on microtechnologies in medicine and biology (2000)

[Davis 2004] Davis, S. P.; Landis, B. J.; Adams, Z. H.; Allen, M. G.; Prausnitz, M. R.: Insertion of microneedles into skin: measurement and prediction of insertion force and needle fracture force. Journal of Biomech. 37 (2004): 1155-1163.

[Dimaio 2003] Dimaio, P.: Modeling, simulation and planning of needle motion in soft tissues. PhD thesis. 2003.

[Ensell 1996] Ensell, G.; Banks, D. J.; Ewins, D. J.; Balachandran, W.; Richards, P. R.: Silicon-based microelectrodes for neurophysiology fabricated using a gold metallization/nitride passivation system J. Microelectromech. Syst. (1996), 5, 117–121.

[Fan 1998] Fan, J.; Wang, Q.; Chen, S.-F.; Yuen, M. M. F.: A spring mass model based approach for warping cloth patterns on 3D objects. The journal of visualization and computer animation (1998), 9, 215 – 227.

[Gibson 1997] Gibson, S. F. F.: 3D ChainMail: a fast algorithm for deforming volumetric objects, in Proc. Of Symp. Interactive 3D Graphics (1997), 149-154.

[Gibson 1999] Gibson, S. F. F.: Using linked volumes to model object collisions, deformation, cutting, carving and jointing, IEEE Trans. On Visual. & Comps Graph, 5, 333-348, 1999.

[Gill 2007] Gill, H. S.; Prausnitz M. R.: Does needle size matter? Journal of Diabetes Science and Technology (2007), 1(5), 725 – 729.

[Gittard 2009] Gittard, S. D.; Ovsianikov, A.; Monteiro-Riviere, N. A.; Lusk, J.; Morel, P.; Minghetti, P.; Lenardi, C.; Chichkov, B. N.; Narayan, R. J.: Fabrication of polymer microneedles using a two-photon polymerization and micromolding process. Journal of diabetes science and technology (2009), 3(2), 304 – 311.

[Greenish 2002] Greenish, S.; Hayward, V.; Steffen, T.: Measurement, analysis and display of haptic Signals During Surgical Cutting. Presence (2002).

[Greenleaf 2003] Greenleaf, J. F.; Fatemi, M.; Insana, M.: Selected Methods for Imaging Elastic Properties of Biological Tissues. Annual Review of Biomedical Engineering (2003), 5, 57 – 78.

[Guyton 1985] Guyton, A.: Anatomy and Physiology. Saunders Colledge Publishing (1985), New York.

[Hanley 1999] Hanley, D. F.; William, M. A.; Naff, N.: Intracranial heomorrhage: Time for an intervention. Critical Care Medicine (1999), 27(3), 477 – 478.

[Henry 1998] Henry, S., D. V. McAllister, M. G. Allen, and M. R. Prausnitz. Microfabricated microneedles: a novel approach to transdermal drug delivery. J. Pharm Sci (1998), 87, 922-925.

[Hayes 1972] Hayes, W. C.; Keer, L. M.; Herrmann, G.; Mockros, L. F.: A mathematical analysis for indentation tests of articular cartilage. J. Biomech. (1972), 5, 541 – 551.

[Hu 2004] Hu, T.; Desai, J. P.: Characterization of soft-tissue material properties: large deformation analysis. In Medical Simulation: International Symposium, ISMS (2004), 28-37, Cambridge, MA, USA.

[Huang 2007] Huang, H; Fu, C.: Different fabrication methods of out-of-plane polymer hollow needle arrays and their variations. Journal of micromech. Microeng (2007), 17, 393 – 402.

[Jones 1977] Jones, E. G.; Wise, S. P.: Size, laminar and columnar distribution of efferent cells in the sensory-motor cortex of monkeys. J. Comp. Neurol. (1977), 175, 391 – 438.

[Khumpuang 2003] Khumpuang, S.; Horade, M.; Fujioka, K.; Sugiyama, S.: Geometrical strengthening and tip-sharpening of a microneedle array fabricated by X-ray lithography. Microsystem technologies (2007), 13, 209 – 214.

[Kim 2007] Kim, K.; Lee, J.B.: High aspect ratio tapered hollow metallic microneedle arrays with microfluidic interconnector. Microsyst Technol (2007), 13, 231 – 235.

[Kim 2009] Kim, B. J.; Hong, C. K.; Rhu, K. H.; Kim, M. N.; Lim, Y. Y.: Microneedle roller for the treatment of acne scar. J Am Acad Dermatol (2009).

[Ko 2010] Ko, K. W.; Kim, H.; Bae, S.; Kim, E.; Lee, Y.-S.: Determination of Spring Constant for Simulating Deformable Object under Compression, Journal of Key Engineering Materials, Vol. 417-418, No. 2, 2010, 369-372. DOI: 10.4028/www.scientific.net/KEM.417-418.369

[Kobayashi 2005] Kobayashi, Y.; Okamoto, J.; Fujie, M. G.: Physical properties of the liver and the development of an intelligent manipulator for needle insertion. Proceeding of the IEEE international conference on robotics and automation (2005), Barcelona, Spain.

[Kovacs 1994] Kovacs, G. T. A.; Storment, C. W.; Halks-Miller, M.; Belczynski, C. R. Jr.; Santina, C. C. D.; Lewis, E. R.; Maluf, N. I.: Silicon-substrate microelectrode arrays for parallel recording of neural activity in peripheral and cranial nerves IEEE Trans. Biomed. Eng. (1994), 41, 567–577

[Kwan 1978] Kwan, H. C.; Mackay, W. A.; Murphy, J. T.: Spatial organization of precentral cortex in awake primates. II. Motor outputs. Journal of Neurophysiology (1978), 41 (5), 1120 – 1131.

[Lee 2002] Lee, Y.; Hwang K.: Skin thickness of Korean adults. Surg Radiol Anat 2002, 24, 183 – 189.

[L' Etang 2006] L' Etang, A.; Huang, Z.: FE simulation of laser generated surface acoustic wave propagation in skin. Ultrasonics (2006), 44, 1243 – 1247. DOI:10.1016/j.ultras.2006.05.077

[Liu 2000] Liu, Z.; Bilston, L.: On the viscoelastic character of liver tissue: experiments and modeling of the linear behavior. Biorheology (2000), 37, 191–201.

[Lin 2008] Lin, S. Y.; Narayan, R.; Lee, Y.-S.: Heterogeneous Deformable Modeling and Topology Modification for Surgical Cutting Simulation with Haptic Interfaces, Computer-Aided Design and Application (2008), 5(6), 877-888. doi:10.3722/cadaps.2008.877-888

[Maynard 1997] Maynard, E. M.; Nordhausen, C. T.; Normann, R. A.: The Utah intracortical electrode array: a recording structure for potential brain-computer interfaces. Electroencephalogr. Clin. Neurophysiol (1997), 102, 228 – 239.

[Mak 1994] Mak, A. F. T.; Liu, G. H. W.; Lee, S. Y.: Biomechanical assessment of below-knee residual limb tissue. J. Rehabil. Res. Dev. (1994), 31(3), 188 – 198.

[McAllister 2003] McAllister, D. V.; Wang, P. M.; Davis, S. P.; Park, J.-H.; Canatella, P. J.; Allen, M. G., Prausnitz, M. R.: Microfabricated needles for transdermal delivery of macromolecules and nanoparticles: Fabrication methods and transport studies. PNAS (2003), 100(24), 13755 – 13760.

[McCartney 1999] McCartney, J.; Hinds, B. K.; Seow, B. L.: The flattening of triangulated surfaces incorporating darts and gussets. Computer-Aided Design (1999), 31, 249 – 260.

[Miller 1999] Miller, M. A.; Pisani, E.: The cost of unsafe injections (1999), 77, 808-811.

[Miller 2000] Miller, K.: Constitutive modelling of abdominal organs. J Biomech (2000), 33, 367 – 373.

[Miller 2002] Miller, K.; Chinzei, K.: Mechanical properties of brain tissue in tension. J Biomech (2002), 35, 483 – 490.

[Mikszta 2002] Mikszta, J. A.; Alarcon, J. B.; Brittingham, J. M.; Sutter, D. E.; Pettis, R. J.; Harvey, N. G.: Improved genetic immunization via micromechanical disruption of skin-barrier function and targeted epidermal delivery. Nature medicine 8, no. 4 (2002), 415 – 419.

[Mohr 2003] Mohr, M.B.; Blumcke, L.G.; Seemann, G.; Sachse, F.G.; Dossel, O.: Volume modeling of myocard deformation with a spring mass system. Proceedings of Surgery Simulation and Soft Tissue Modeling: International Symposium, IS4TM 2003, 332-339.

[Mollemans 2003] Mollemans, W.; Schutyser, F.; Cleynenbreugel, J.V.; Suetens, P.: Tetrahedral mass spring model for fast soft tissue deformation. Proceedings of Surgery Simulation and Soft Tissue Modeling: International Symposium, IS4TM 2003, 145-154.

[Mollemans 2007] Mollemans, W.; Schutyser, F.; Nadjmi, N.; Maes, F.; Suetens, P.: Predicting soft tissue deformations for a maxillofacial surgery planning system: From computational strategies to a complete clinical validation. Medical Image Analysis 11 (2007) 282-301.

[Mott 2008] Mott, R. L.: Applied Strength of Materials. 5th edition. Pearson Prentice Hall (2008).

[Motta 2005] Motta, P. S.; Judy, J. W.: Multielectrode microprobes for deep-brain stimulation fabricated using a novel 3-D shaping electroplating process. IEEE Transactions on biomedical engineering (2005), 52(5), 923 – 933.

[Mow 1989] Mow, V. C.; Gibbs, M. C.; Lai, W. M.; Zhu, W. B.; Athanasiou, K. A.: Biphasic indentation of articular cartiage. Part II: a numerical algorithm and an experimental study. J. Biomech. (1989), 222, 853 – 861.

[Murray 1981] Murray, E. A.; Coulter, J. D.: Organization of corticospinal neurons in the monkey. J. Comp. Neurol. (1981), 195, 339 – 365.

[Najafi 1994] Najafi, K.: Solid-state microsensors for cortical nerve recordings. IEEE engineering in medicine and biology magazine (1994), 13(3).

[Nava 2004] Nava, A.; Mazza, E.; Kleinermann, F.: Evaluation of the mechanical properties of human liver and kidney through aspiration experiments. Technol Health Care (2004), 12(3), 269-280.

[O'Brien 2002] O'Brien, D. P.; Nichols, T. R.; Allen, M. G.: Flexible microelectrode arrays with integrated insertion devices MEMS'01 (2002), 216–219.

[Odland 1991] Odland, G.: Structure of the skin. In Physiology, biochemistry and molecular biology of the skin. Oxford: Oxford University Press, 1991.

[Park 2005] Park, J.-H.; Allen, M. G.; Prausnitz, M. R.: Biodegradable polymer microneedles: Fabrication, mechanics and transdermal drug delivery. Journal of Controlled Release (2005), 104, 51-66.

[Park 2007] Park, J.-H.; Yoon, Y.-L.; Choi, S.-O.; Prausnitz, M. R.; Allen, M. G.: Taper conical polymer microneedles fabricated using an integrated lens technique for transdermal drug delivery. IEEE Transactions on Biomedical Engineering (2007), 54(5), 903 – 913.

[Parker 2007] Parker, E.R.; Rao, M.P.; Turner, K.L.; Meinhart, C.D.; MacDonald, N.C.: Bulk micromachined titanium microneedle. Journal of Microelectromechanical systems (2007), 16(2).

[Prausnitz 2008] Prausnitz, M. R.; Langer, R.: Transdermal drug delivery. Nature Biotechnology (2008), 26, 1261 – 1268.

[Rapaport 2011] Rapaport, J.; Boss, W. K.: Cosmetic Skin and Surgery Center. Electronic resource. www.cosmeticskin.com

[Reynolds 1992] Reynolds, D.; Lord, M.: Interface load analysis for computer-aided design of below-knee prosthetic sockets. Med. Biol. Eng. Comput. (1992), 1, 89 – 96.

[Roxhed 2007] Roxhed, N.; Gasser, T. C.; Griss, P.; Holzapfel, G. A.; Stemme, G.: Penetration enhanced ultrasharp microneedles and prediction on skin interaction for efficient transdermal drug delivery. Journal of Microelectromechanical Systems (2007), 16(6), 1429-1440.

[Rousche 1998] Rousche, P. J.; Normann, R. A.: Chronic recording capability of the Utah Intracortical electrode array in cat sensory cortex. Journal of neuroscience methods (1998), 82, 1 – 15.

[Sakamoto 1996] Sakamoto, M.; Li, G.; Hara, T.; Chao, E. Y. S.: A new method for theoretical analysis of static indentaion test. J. Biomech. (1996), 29(5), 679 – 685.

[Sakuma 2003] Sakuma, I.; Nishimura, Y.; Chui, C. K; Kobayashi, E; Inada, H.; Chen, X.: In vitro measurement of mechanical properties of liver tissue under compression and elongation using a new test piece holding method with surgical glue, Proceedings of the International Symposium on Surgery simulation and Soft Tissue Modelling (2003), vol. 2673 of Lecture Notes in Computer Science, 284–292.

[Smart 2000] Smart, W. H.; Subramanian, K.: The use of silicon microfabrication technology in painless blood glucose monitoring. Diabetes technology & therapeutics (2000), 2(4), 549 – 559.

[Sokoloff 1966] Sokoloff, L.: Elasticity of articular cartilage. Fed. Proc. Am. Soc. Exp. Biol. (1966), 25, 1089 – 1095.

[Stieglitz 1997] Stieglitz, T.; Beutel, H.; Meyer, J.-U.: A flexible, light-weight multichannel sieve electrode with integrated cables for interfacing regenerating peripheral nerves Sensors Actuators A (1997), 60, 240–243

[Stoeber 2005] Stoeber, B.; Liepmann, D.: Arrays of hollow out of plane microneedles for drug delivery. JMEMS (2005), 14(3), 472-479.

[Sugai 1999] Sugai, Y.; Asa, F.; Okada, Y.; Yokoshima, T.; Momma, T.; Osaka, T.; Ito, T.: Formation of microprobe using nickel electrodeposition. Electrochemistry (1999), 67 (12).

[Takeuchi 2000] Takeuchi, S.; Shimoyama, I.: A three-dimensional shape memory alloy microelectrode with clipping structure for insect neural recording J. Microelectromech. Syst. (2000), 9, 24–31.

[Takeuchi 2004] Takeuchi, S.; Suzuki, T; Mabuchi, K.; Fujita, H.: 3D flexible multichannel neural probe array. Journal of micromech. Microeng (2004), 14, 104 – 107

[Tang 2003] Tang, Y.M.; Zhou, A.F.; Hui, K.C.: Comparison of FEM and BEM for interactive object simulation. Computer-Aided Design 38 (2006) p. 874-886.

[Tay 2002] Tay, B. K.; Stylopoulos, N.; De, S.: Measurement of in-vivo force response of intra-abdominal soft tissues for surgical simulation. Stud Health Technol Inform (2002), 85, 514 – 519.

[Teo 2006] Teo, A. L.; Shearwood, C.; Ng, K. C.; Lu, J.; Moochhala, S.: Transdermal microneedles for drug delivery applications. Material science and engineering B (2006), 132, 151 – 154.

[Thiboutot 2009] Thiboutot, D.; Gollnick, H.: New insights into the management of acne: an update from the global alliance to improve outcomes in acne group. J Am Acad Dermatol (2009), 60, S1-50.

[Timoshenko 1961] Timoshenko, S. P.; Gere, J. M.: Theory of Elastic Stability. McGRAW-Hill Book Company, INC. (1961)

[Vannah 1996] Vannah, W. M.; Childress, D. S.: Indentor test and finite element modeling of bulk muscular tissue in vivo. J. Rehabil. Res. Dev. (1996), 33(3), 239 – 252.

[Verbaan 2008] Verbaan, F. J.; Bal, S. M.; van den Berg, D. J.; Dijksman, J. A.; van Hecke, M.; Verpoorten, H.; ven den Berg, A.; Luttge, R.; Bouwstra, J. A.: Improved piercing of microneedle arrays in dermatomed human skin by an impact insertion method. Journal of Controlled Release (2008), 128, 80 – 88.

[Wang 1992] Wang, B. C.; Wang, G. R.; Yan, D. H.; Liu, Y. P.: An experimental study on biomechanical properties of hepatic tissue using a new measuring method. Biomed Mater Eng (1992), 2, 133 – 138.

[Wang 2002] Wang, C. C. L.; Smith, S. S.-F.; Yuen, M. M. F.: Surface flattening based on energy model. Computer-Aided Design (2002), 34, 823 – 833.

[Wang 2004] Wang, S.; Fenster, A.: A virtual reality based 3D real-time interactive brachytherapy simulation of needle insertion and seed implantation. IEEE International symposium on biomedical imaging: nano to micro (2004), vol. 1, 280 – 283.

[Wang 2005] Wang, C. C. L.; Tang, W.; Yeung, B. M. L.: Freeform surface flattening based on fitting a woven mesh model. Computer-Aided Design (2005), 37, 799 – 814.

[Wild 2004] Wild, S.; Roglic, G.; Green, A.; Sicree, R.; King, H.: Global prevalence of diabetes: estimates for the year 2000 and projections for 2030. Diabetes Care (2004), 27(5), 1047-1053.

[Wilke 2007] Wilke, N.; Morrissey, A.: Silicon microneedle formation using modified mask designs based on convex corner undercut. Journal of Micromechanics and Microengineering (2007), 17, 238 – 244.

[Wu 2006] Wu, K. S.; Van Osdol, W. W.; Dauskardt, R. H.: Mechanical properties of human stratum corneum: Effects of temperature, hydration, and chemical treatment. Biomaterials (2006), 27, 785 – 795.

[Yuzhakov 2003] Yuzhakov, V. V.; Gartsein, V.; Owens, G. D.: Microneedle apparatus used for marking skin and for dispensing semi-permanent subcutaneous makeup. US patent no. 6,565,532 B1, 2003.

[Zahn 1995] Zahn, J. D.: Microfabricated Microneedles for Minimally Invasive Drug Delivery, Sampling and Analysis. University of California, Berkeley and San Francisco (1995)

[Zhang 1997] Zhang, M.; Zheng, Y. P.; Mak, A. F. T.: Estimating the effective Young's modulus of tissues from indentation test – nonlinear finite element analysis of effects of friction and large deformation. Med. Eng. Phys. (1997), 19(6), 512 – 517.